PACKAGING AND CHARACTERIZATION OF MEMS OPTICAL MICROPHONES

A Thesis
Presented to
The Academic Faculty

by

Caesar Garcia

In Partial Fulfillment
of the Requirements for the Degree
Master of Science in the
George W. Woodruff School of Mechanical Engineering

Georgia Institute of Technology
December, 2007

PACKAGING AND CHARACTERIZATION OF MEMS OPTICAL MICROPHONES

Approved by:

Dr. F. Levent Degertekin, Advisor
School of Mechanical Engineering
Georgia Institute of Technology

Dr. Peter J. Hesketh
School of Mechanical Engineering
Georgia Institute of Technology

Dr. Kenneth A. Cunefare
School of Mechanical Engineering
Georgia Institute of Technology

Date Approved: November 9th, 2007

To my grandfather, Calixto Garcia

ACKNOWLEDGEMENTS

I would first like to express my sincere gratitude toward the people who contributed tremendously to the work represented by this thesis. Foremost, I would like to thank my thesis advisor, Professor F. Levent Degertekin, for allowing me the privilege of participating as a member of his research group during my graduate studies. I have truly appreciated his patience, guidance, and jovial charisma which have all contributed to the technical background in optical and acoustic sensors that I have acquired over the past two years. I would also like to thank Professors Peter J. Hesketh and Kenneth A. Cunefare for agreeing to serve on my reading committee.

Of essential importance to the culmination of this work was the invaluable contributions made by Dr. Neal Hall. Dr. Hall's presence, both as a mentor and as a friend, was a vital factor in making this educational pursuit a worthwhile endeavor. I am equally appreciative of the enjoyable experience of working alongside Baris Bicen throughout this research. I owe a great deal of thanks to several other members of the MiST Laboratory as well. First, I would like to thank both Hamdi Torun and Guclu Onaran who graciously offered their time and expertise on countless occasions making significant contributions to my education and research progress. I would also like to thank Shakeel Qureshi and Kamran Jeelani for their contributions.

Other entities to which I owe special thanks include the National Institute of Health for supporting this research, the Integrated Acoustics Laboratory (IAL) at Georgia Tech for use of the anechoic chamber facility as well as other equipment essential to this work, Sandia National labs for the supply of omnidirectional microphone devices, and the Vibrations Research Laboratory at Binghamton University, New York. Specifically,

many thanks are owed to Professor Ron Miles, Quang Su, and Dr. Weili Cui for supplying resources in the form of biomimetic directional microphone devices and modeling tools.

Finally, I would like to thank my father, mother, two brothers, and four sisters for motivation and support during my time as a graduate student and throughout my life, and for being just plain wonderful.

TABLE OF CONTENTS

LIST OF TABLES

Page

LIST OF FIGURES

Page

SUMMARY

This thesis describes the integrated packaging of silicon micromachined microphones with diffraction-based optical displacement detection. Both omni-directional and directional microphone designs are described and tested. Omni-directional microphones were fabricated by Sandia National Labs and share similarities with existing capacitive micromachined microphones. The novel, biomimetically inspired, directional microphones were supplied by the State University of New York at Binghamton and accomplish directionality by imitating the intertympanal mechanical coupling of the fly, Ormia ochracea. Designed to incorporate the presented optical detection method, these microphones avoid the contradictions associated with the miniaturization of capacitive detection. Commercially available micro-optoelectronic devices, used primarily in fiber optic data transmission, are capable of meeting both the size and performance requirements for miniaturized high-quality optical microphones. A computer simulation model is used to optimize the micro-optical system which is contained within a $1mm^3$ volume. These micro-optical simulations predict displacement resolution levels on the order of 12fm/√Hz for ideal operation. A modular packaging architecture, suitable for testing both types of microphones and comparable to measurement microphone packages, is designed to incorporate micro-optical detection and imposes minimal disturbance to measured acoustic fields. Results from the omnidirectional optical microphone structure demonstrate the capability of resolving 150fm/√Hz (5/√Hz) across much of the audible bandwidth. This resolution is primarily limited by relative intensity laser noise and allows the 2mm diameter omnidirectional microphone to achieve a 26dBA noise floor. The biomimetic directional optical

microphone, which has an equivalent port spacing of 1mm, is able to resolve 2.5pm/√Hz (15μPa/√Hz) at 1kHz. The noise floor of this microphone is measured to be 34dBA and is limited by the thermal mechanical noise level of the soft differential diaphragm. Additionally, these results demonstrate an array of two biomimetic directional optical microphones located on the same silicon chip and separated by less than 5mm with measured directivity indices of 4.6 and 3.5. These results confirm the micro-optical detection method as an alternative to capacitive detection especially for miniaturized microphone applications and suggest that this method in its modular packaging architecture is competitive with industry leading measurement microphones.

CHAPTER 1

INTRODUCTION

Microphones occupy a pervasive space among acoustic sensors if not sensor technology in general. Various applications have lead to specific requirements for microphones; however, metal-film, capacitive measurement microphones are generally accepted as the ultimate standard in terms of size and detection capability. Presently, the demand for higher quality miniaturized microphones is growing. In many instances, however, current technologies are unable to meet these demands, and as a result, numerous microphone applications are forced to settle for lower performance standards. One example of such an application is hearing aid microphones where quality is extremely important and desire for miniaturization goes without saying. Some of the challenges facing miniaturization have been solved with the advent of microelectromechanical systems (MEMS) which offers marginal improvements for small scale capacitive microphones. Performance degradation associated with the microphone miniaturization, however, is attributed to the limitations of capacitive sensing itself and capacitive MEMS microphones are therefore subject to these same limitations. Given its long history of development, the performance of capacitive detection in microphones is not easily surpassed. Nevertheless, several alternative sensing mechanisms have been explored as solutions to capacitive sensing limitations. In this chapter, capacitive detection is introduced in the context of miniaturized microphones and several alternative

detection techniques are described. Additionally, this introduction includes a brief summary of microphone response patterns and their importance.

Microphone Miniaturization

In addition to the convenience associated with miniaturization, there is a more fundamental motivation to keep microphones as small as possible. Figure 1 provides an illustration of a microphone in the presence of a measured sound field for the following explanation.

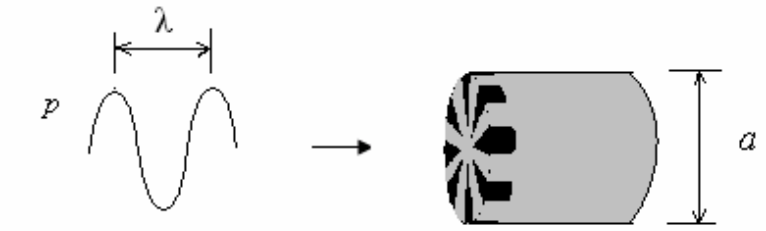

Figure 1. Cylindrical microphone obstacle in a measured sound field

When obstacles are located in a sound field, their size relative to the wavelength, λ, of the pressure wave, p, becomes an important factor which can alter the measurement of the field through diffraction and scattering effects. For cylindrical obstacles with diameter a, such as measurement microphones, these effects tend to limit the high frequency operation of the microphone when $a/\lambda>1$. In addition to diffraction and scattering effects, the feasibility of microphone arrays for sound source localization and sound intensity measurements is dependent upon the separation between individual microphone elements. In these types of applications, high quality miniaturized microphones are often essential given certain sound fields of interest. Unfortunately, it has proven difficult to manufacture high quality microphones "smaller than about 12mm" [1-3].

Sensing Mechanisms for Miniaturized Microphones

There are several reasons why microphone performance scales unfavorably with decreasing size. One of the underlying challenges is that most sensing mechanisms are not readily adapted to miniaturization and are incapable of attaining the same sensitivity levels as their macroscale embodiments. Generally speaking, there are two aspects of microphone sensitivity which together are responsible for determining the overall or "open circuit" sensitivity, *S*. First, the measure of a microphone's ability to convert incident pressure into diaphragm displacement is called mechanical sensitivity, *Sm*, and is sometimes referred to as compliance. Electrical sensitivity, *Se*, on the other hand, is a measure of microphone's ability to convert diaphragm displacement into an electrical signal. The overall sensitivity, *S*, of a microphone is given by *Sm* X *Se* and is expressed in units of *mV/Pa*. Capacitive detection is by far the most common means by which today's microphones make the conversion from diaphragm deflection to output voltage, although it is certainly not the only way. The schematic shown in Figure 2 illustrates the basic principles of a condenser microphone. Here, *Sm* is modeled by a spring-mass-damper system while *Se* is modeled by a variable gap capacitor.

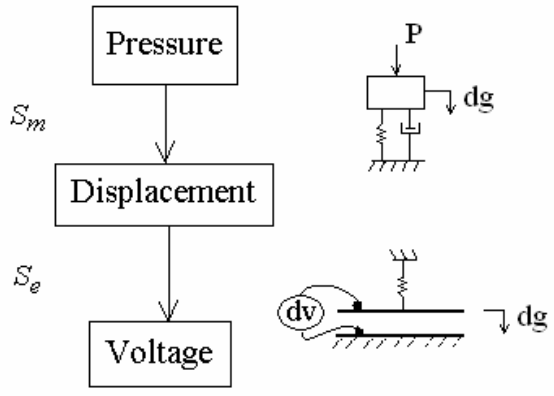

Figure 2. Principle schematic of a condenser microphone

Capacitive Sensing

Despite the prevalence of capacitive microphones, the miniaturization of capacitive detection is associated with a number of drawbacks which complicate and constrict the design of small condenser microphones. These drawbacks are based primarily on the interrelation between three aspects of capacitive design: 1) diaphragm (electrode) area, 2) gap height, and 3) backplate resistance. Before exploring these interactions further, it is important to establish a general understanding of the expressions for *Sm* and *Se* in capacitive devices which use a bias voltage to optimize sensitivity. Mechanical sensitivity, *Sm*, of a condenser microphone is dictated by the net forces acting on the diaphragm. Considering only internal forces, the two pressures acting on the diaphragm of a condenser microphone are due to spring forces and the presence of an electric field induced by the bias voltage, and will be referred to as P_e and P_r respectively. P_r depends on the spring constant of the diaphragm while P_e is defined as

$$P_e = \frac{\varepsilon_o}{2}\left(\frac{V_{bias}}{s-g}\right)^2 \qquad 1$$

where ε_o is the permittivity of free space, V_{bias} is the DC bias voltage, and s is an effective thickness of the dielectric regions which takes into account the properties of composite layers. The mechanical sensitivity for capacitive devices operating in the presence of significant electric fields is then defined as

$$S_m = \frac{1}{\frac{dP_r}{dg} - \frac{dP_e}{dg}} \qquad 2$$

Electrical sensitivity, on the other hand, is simply the change in output voltage due to a change in diaphragm displacement.

$$S_e = \frac{dV}{dg} \qquad 3$$

In large capacitive microphones, the contribution of dP_e/dg is usually small compared to the diaphragm compliance and can be ignored in Equation 2, but this is not always the case.

Because miniaturization requires a reduction in the diaphragm area available for capacitive detection, sensitivity is sacrificed. Small capacitive devices are therefore inclined to compensate in other ways. The lumped element model in Figure 3 helps to explain these possible compensatory techniques and is referred to as the parallel plate approximation. One possible way of increasing the overall sensitivity is to increase *Sm* by softening the diaphragm spring constant, k_s. This is usually not an easy task to accomplish in small scale devices due to fabrication challenges.

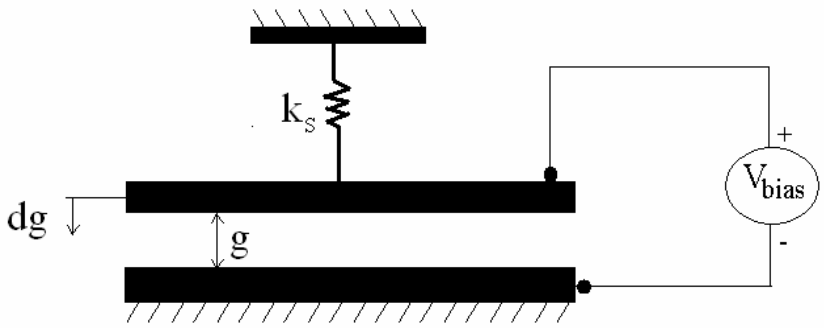

Figure 3. Parallel plate model of a condenser microphone

Another possible way of compensating for sensitivity loss in small capacitive devices is to bias the diaphragm to operate at gap heights which allow increased *Se*. The disadvantage here, however, is that the diaphragm exhibits undesirable behavior as the gap height becomes smaller. The first issue of contention is understood by the

relationship between V_{bias}, and electrostatic force, F_e. This relationship is derived from the principle of virtual work such that

$$F_e = \frac{C^2 V_{bias}^{\ 2}}{2\varepsilon_0 A k_s} \qquad 4$$

where k_s is the effective spring constant of the diaphragm shown in Figure 3. When the diaphragm deflects in response to F_e, a spring force, $F_s=k_s(dg)$, also begins acting on the diaphragm. As V_{bias} is increased, the forces F_e and F_s begin to converge. A force balance then requires that

$$k_s(dg) = \frac{C^2 V_{bias}^{\ 2}}{2\varepsilon_0 A k_s} \qquad 5$$

This equality leads to a phenomenon known as electrostatic "collapse" or "pull-in" and occurs when dg=g/3. Although large condenser microphones are less affected by the condition of collapse since their diaphragm areas allow greater sensitivity without approaching this precarious gap height, this condition can be detrimental to miniaturized capacitive microphones. This occurrence coincides with nonlinearity as well and for these reasons, microphones should not operate in this region. Furthermore, it is often the case that such attempts to optimize sensitivity result in an undesirable dependence between sensitivity and frequency which can limit the bandwidth of condenser microphones [4, 5].

The third conflicting design parameter involves the backplate resistance of capacitive devices. Since large backplate resistance values lead to excessive microphone internal noise levels, backplates are usually perforated to facilitate the flow of air behind the diaphragm. In addition to alleviating the impedance to flow, however, backplate

perforations result in a diminished sensing area and therefore a decrease in sensitivity. In miniaturized microphones whose diaphragm area is already small, there is little room for compromise. For this reasons, small condenser microphones generally have higher noise floors and lower sensitivity levels compared to larger condenser microphones [6].

In summary, capacitive sensing is the most widely employed method of detecting microphone diaphragm displacements and is a well developed technology for standard size measurement microphones. However, capacitive detection does not scale well with decreasing size. The dependence of capacitive detection upon electrode area, gap height, and backplate resistance tends to significantly degrade the performance of miniaturized condenser microphones to the point that several other sensing methods have been and are currently being explored.

Other Sensing Methods

A variety of other sensing methods can be used in order to detect sound pressure. Another common type of pressure transducer uses the principle of magnetic induction and is often referred to as the dynamic pressure transducer. Magnetic induction occurs when a conductive material is located in a changing magnetic field. It can occur, as is the case in a moving coil microphone, when a conductive coil passes through a magnetic field. In moving coil microphones, the conductive coil is attached to a flexible diaphragm which moves in response to pressure. This coil is then situated around a permanent magnet which remains fixed so that there is relative motion between the coil and the magnetic field. Other configurations are of course possible; however, these microphones almost always occupy more space than capacitive microphones and usually contain at least one pound of metal. Additionally, dynamic microphones tend to involve

more complicated designs than capacitor microphones. Although dynamic pressure transduction is much more common among other pressure transducers such as loudspeakers, which operate in a reciprocal manner, dynamic microphones are unsuitable for small scale applications such as hearing aid microphones [2].

Compared to dynamic microphones, piezoelectric microphones are much more suitable for miniaturized applications. These microphones employ the electromechanical properties of piezoelectric materials and in some ways are considered more rugged than condenser microphones. Because of their high mechanical impedance, traditional piezoelectroacoustic transducer designs are better suited for hydrophone applications. However, piezoelectric microphones have been fabricated by depositing materials such as zinc oxide (ZnO) using low pressure chemical vapor deposition (LPCVD) or sputtering to create piezoelectric thin film diaphragms with minimal mechanical impedance. The sensitivity of different piezoelectric materials can vary significantly, and unfortunately, the performance of some of the most sensitive piezoelectric materials is dependant upon environmental conditions such as temperature and humidity. Although reported characteristics, such as noise performance, of piezoelectric microphones fall short of the standards for high fidelity microphone performance, small scale piezoelectric microphones are likely to improve in the future [2, 7, 8].

Perhaps the most promising alternative to traditional capacitive sensing in miniature microphones is optical detection. The idea of an optical microphone has been around since a patent for a “photophone” was received in 1880. Optical detection is usually based on the modulation of light rather than the conversion from an existing energy form into light energy. Several methods of accomplishing this modulation have

been demonstrated over the years although overlapping methods have hindered the development of convenient taxonomy [9]. One general class of optical detection is characterized by the interference of superposing light waves and is known as interferometry. Optical detection, by interferometric means offers several advantages over other sensing mechanisms in microscale devices such as high displacement resolution, low shot-noise limitations, and decoupled electrostatic actuation. Achieving all of these performance attributes within a package size on par with other miniaturized microphones, however, is an accomplishment yet to be reported.

MEMS Microphones

The challenges associated with microphone miniaturization have faced the microphone industry for many years. For example, the Danish company Brüel & Kjær is well known for producing precision microphones which are optimized using state-of-the art manufacturing procedures to control thin-film stresses. The fabrication process requires manual assembly of each microphone typically resulting in elevated price scales. Yet, even these premium microphones are less than ideal for the miniaturized applications which have been mentioned. In an attempt to achieve and standardize acceptable levels of performance at smaller size scales, silicon based micromachining is currently being explored as an alternative to traditional fabrication methods. In 2003, the first microelectromechanical (MEMS) microphones emerged onto the consumer market for use in cellular phones. The quality of some MEMS microphones has even become competitive with high quality measurement microphones such as the Brüel & Kjær model 4939 which are up to three times larger [10, 11].

Silicon based micromachining offers several advantages over other means of microphone fabrication. One undeniable advantage is the level of control for a given sequence of processes. In silicon micromachining, these processes usually involve either etching or deposition of material and typically occur at rates on the order of several to several hundred angstroms per minute. At these rates it is possible to precisely control the vertical dimensions of silicon micromachined microphones. Tight control over lateral and horizontal dimensions is also indicative of lithography techniques which are used to define surface topologies in silicon micromachining. Finally, the advantageous material properties of silicon devices can be maintained uniformly by batch fabrication of silicon microphones on a single wafer under these processing conditions. In addition to reducing costs, this streamlined process facilitates consistent dynamic properties among silicon micromachined microphones and opens the possibility of miniature silicon microphone arrays for sound source discrimination and localization applications.

A typical MEMS microphone is shown in Figure 4 for conceptual demonstration. In this design, a metallization layer is deposited onto a silicon substrate to form a conductive backplate. Using wet etching or deep reactive ion etching (RIE), the metallized backplate is perforated to reduce damping in the form of backplate resistance. A dielectric cavity is usually formed by depositing a conductive diaphragm layer on top of a sacrificial layer which is subsequently removed. The metallized membrane and back electrode function as the conductive parallel plates of a movable capacitor. The acoustic response is tailored by adjusting the back volume as well as the vent hole resistance using these and other precise micromachining techniques [3].

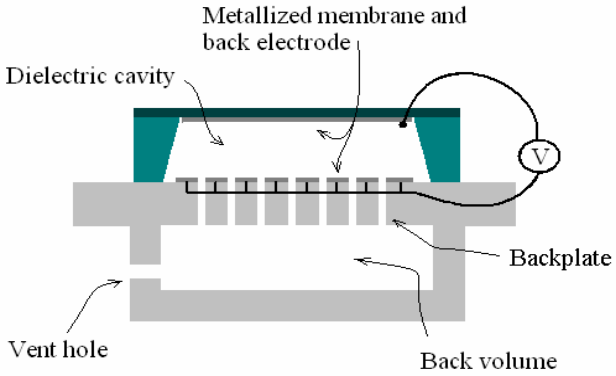

Figure 4. Silicon micromachined microphone

As mentioned previously, one way to compensate for the reduction in sensitivity of miniaturized microphone diaphragm areas is to increase the compliance of the diaphragm. A MEMS microphone diaphragm composite such as the one shown in Figure 4 might consist of a 1-3µm silicon based layer and a metallized electrode with a thickness of several hundred angstroms. In comparison, high quality thin-film metal diaphragms of a ¼ inch microphone, for example, are considerably less compliant, not to mention costly to fabricate [10]. Under the assumption that other factors are held constant, this advantage allows MEMS microphones to exhibit higher sensitivity than other microphones of comparable size. Although this softening of the diaphragm also reduces the bandwidth of the microphone, it is another useful advantage of MEMS microphones. Despite these advantages, capacitive detection is still the limiting factor in MEMS designs because of inherent contradictions between capacitive detection and miniaturization [12].

A Highly Sensitive MEMS Optical Microphone

In response to these limitations, a MEMS microphone design based on a phase sensitive optical diffraction grating has been reported. In addition to capitalizing on the

advantages of MEMS, this design accomplishes some of the advantages promised by optical detection methods such as high displacement resolution on the order of 2.4pm/√Hz and decoupled electrostatic actuation, but fails to reduce thermal mechanical noise levels below reasonable levels. The 5μm grating period relies on the fabrication capabilities of silicon micromachining although the remainder of the structure is fairly simple. The optical detection setup for this device makes use of a low-noise, high-power laser source along with various focusing optics, and the overall package of this setup is rather cumbersome with a form factor unsuitable for reliable acoustic testing. Although this MEMS optical microphone successfully demonstrates high displacement resolution, it is not a convincing demonstration of the optical detection method as an alternative to capacitive detection in small scale microphone applications [13].

A Biomimetically Inspired Directional MEMS Microphone with 1mm Port Spacing

Another unique microphone structure taking full advantage of the capabilities of silicon micromachining was inspired by the directional acoustic sensing capabilities of a small fly, Ormia ochracea, which shares a parasitic relation with crickets. This fly is able to locate crickets by listening to their mating calls and detecting the direction from which these calls originate to within 2° accuracy. What makes the fly's ability unique, is the size in which directional sensing is accomplished. Most creatures utilize a temporally induced phase delay incurred while the pressure wave travels the separation distance between two separated ears. This distance is usually comparable to the wavelength of the sources being located. In the case of the Ormia fly, however, the inlet ports are located less than 1mm apart while the acoustic wavelengths of interest are as much as 7cm. This

means that the fly is able to detect minute pressure differences across its tympanal membrane in order to obtain directional information. Most animals use neurological processing to determine the arrival time difference between two inputs, but because of its small size, this time delay would only be about 2μs. Instead, the Ormia fly makes use of a single intertympanal membrane supported by a rigid pivoting hinge which couples the two sides of the membrane and actually slows the effective signal delay. The dynamic coupling between the two sides of membrane is sensed inside the inner ear cavity and allows the fly to distinguish between right and left [14].

The MEMS microphone design replicates this dynamic coupling about a central hinge as shown in Figure 5. The coupling hinge is rigidly attached to a silicon substrate allowing a "teeter-totter" type motion.

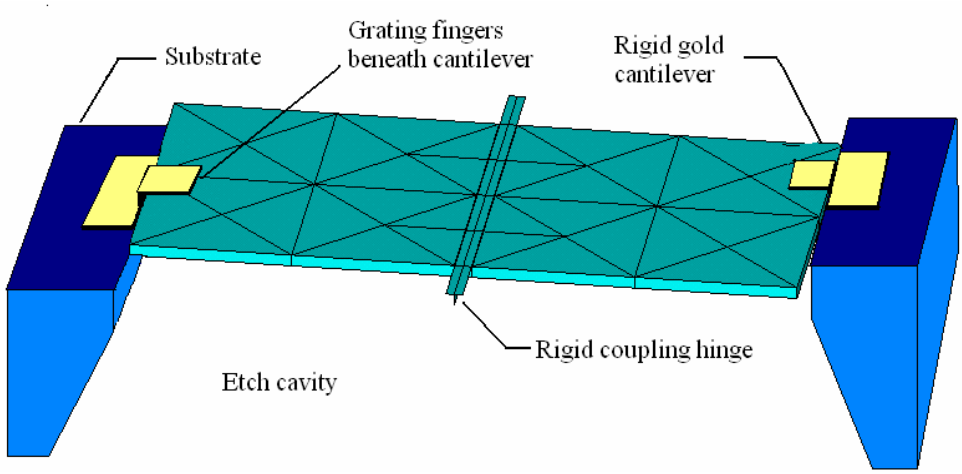

Figure 5. Biomimetic gradient microphone design

The dynamics of the diaphragm motion are tailored to maximize sensitivity over a frequency range of interest. For example, the diaphragm is roughly 1μm thick and is equipped with stiffeners which provide added stability and minimal mass. This

complexity which allows the structure to mimic nature's model, would be virtually impossible without the aid of silicon micromachining technology.

As might be expected, the unique structure of the biomimetic directional microphone presents a challenge for capacitive detection. There is first the issue of the rocking motion and a corresponding tilt which is unfavorable for capacitive detection. Another issue is that parasitic capacitance effects can become dominant in small capacitive devices. Efforts to increase the transduced signal by increasing the backplate electrode area can minimize the effects of parasitic capacitance; however, they are ill-advised since large backplate areas produce more damping and therefore more noise in the system. Therefore, an alternative to capacitive sensing is especially valuable for this device which offers a unique design for directional sensing on an extraordinarily small size scale [15, 16].

The introduction of this unique directional microphone warrants a brief review of how different microphone response patterns are formed and the advantages which these microphones offer. As opposed to omnidirectional microphones, which respond uniformly to signals coming from all directions, the mechanical sensitivity of the biomimetic directional microphone structure is a function of the impinging wave's incidence angle and is referred to as a differential microphone. In other cases, directional sensitivity is accomplished by combining the output of two or more microphones. In either case, directional microphones are able focus their sensitivity in certain directions while blocking sounds arriving from other directions as seen in Figure 6 where both an omnidirectional and a directional response pattern are plotted. The "figure 8" response of a directional microphone provides obvious advantages over omnidirectional microphones

in noise suppression applications such as hearing aids. Despite this advantage, directional microphones are not yet pervasive in hearing aid technology given their current performance limitations at small size scales [17, 18].

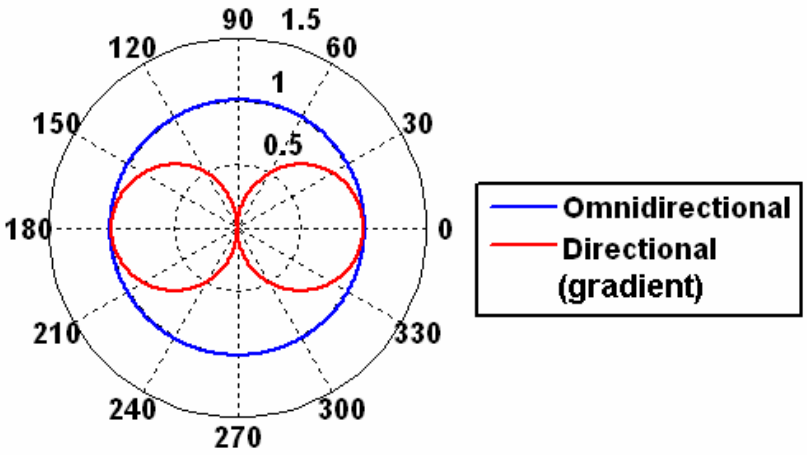

Figure 6. Omnidirectional and gradient microphone response patterns

Motivation

In summary, reducing the size of a condenser microphone decreases capacitive sensitivity while amplifying the effects of noise and parasitic capacitance. Contradictory design constraints exist and overlap between the mechanical and electrical domain and make it especially difficult to optimize capacitive detection in small scale microphones. Although measurement-quality capacitive MEMS microphones have been reported, there is sufficient motivation to explore alternative detection techniques in MEMS structures especially in the case of the unique biomimetic directional microphone design which does not lend itself well to capacitive detection. Specifically, there is motivation to develop a miniaturized, fully integrated detection scheme which eases the restraints on diaphragm area, gap height, and backplate resistance in a small scale environment.

CHAPTER 2

OPTICAL MODELING FOR MICROSCALE IMPLEMENTATION

An increasingly common trend for resolving the inherently small displacements of MEMS structures is to use optical sensing. Various optical sensing techniques have been demonstrated in high-resolution applications such as atomic force microscopy (AFM), ultrasonic imaging, seismology, and inertial navigation systems. Of these various techniques, interferometry is among the most common and involves the interference of superposing waves. In order to accomplish interphase modulation of a single coherent light source, the optical detection architecture presented in this thesis uses phase sensitive diffractive gratings to accomplish the sensitivity of type Michelson interferometers. In these architectures, electrostatic actuation capabilities are decoupled from the optical sensing scheme. In the proposed optical detection method, electrostatic actuation is used to tune the sensitivity of the microphone and to provide self-dynamic characterization capabilities and force-feedback modalities. The proposed microscale architecture requires no optical beam splitters or focusing lenses in order to accomplish sensitivity levels surpassing high quality measurement microphones. In order to maximize these sensitivity levels, computer simulation is used to model the micro-optical system. Other considerations such as power and shot noise are also taken into account in the simulation.

Phase Sensitive Interferometric Gratings

An example of a phase sensitive interferometric grating structure with the sensitivity of Michelson interferometers is illustrated in Figure 7. In this illustration, a collimated light source illuminates a periodic grating which splits the incident light beam into two paths, one reflecting back towards the source and a second transmitting through the grating. The transmitted light beam travels a distance, g, before encountering a second surface and reflecting back towards the grating. After passing back through the grating and traveling a total distance $2g$, the second path interferes with the first in either a constructive or destructive manner. The result is an optical field with intensity

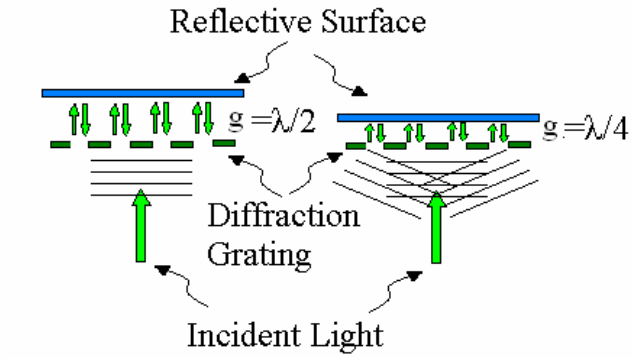

Figure 7. Reflection and diffraction in a phase-sensitive optical grating

concentrations occurring at fundamental and higher order mode locations. The intensity variation of a particular mode as well as the mode locations themselves, are dependent upon several factors which will be discussed in more detail later in this chapter. In the context of the proposed design for optical microphones the intensity profile is most importantly a function of the gap, g, between the grating and the reflective surface. For example, the first case of Figure 7 illustrates the scenario when $g=\lambda/2$. For this gap height, the total distance traversed by the second path is equal to λ and the phase sensitive

interferometric grating behaves as a perfect reflector. This same result is obtained at any gap height where the total phase shift accrued by the transmitted wave is equal to $n2\pi$ where n is any integer. In the case where $g=\lambda/4$, the accumulated phase is equal to π and therefore all of the light energy is diffracted into higher order modes. Gap heights producing phase shifts other than $n2\pi$ or $n\pi$ result in an optical field consisting of both reflection and diffraction.

The relationship between gap height and a given order intensity is the fundamental link which allows phase sensitive diffraction grating architectures to function as high resolution displacement sensors. Assuming a single mode incident light source which can be expressed as $cos(\omega t+kz)$ where k is the wave number and z is the distance traversed by the light wave relative to some origin $z=0$, the variation in the optical field can be obtained using superposition. For example, if the incident laser light comes into contact with the grating at $z=0$, the reflected light is expressed as $cos(\omega t)$. The transmitted portion of the light travels the extra distance $2g$ and is therefore expressed as $cos(\omega t+2kg)$ once it returns through the grating. When these cosine terms are in phase, they added together to yield the zeroth order component of the intensity which is proportional to

$$I_0 \alpha \cos^2(\frac{2\pi}{\lambda} g) \qquad 6$$

Similarly, it can be shown that the first order components (I_{+1} and I_{-1}) follow the proportionality

$$I_{\pm 1} \alpha \sin^2(\frac{2\pi}{\lambda} g) \qquad 7$$

and remain 180° out of phase with the zeroth order component of the intensity profile. In order to verify previous discussion, it is useful to consider I_0 in the cases $g=0$ and $g=\lambda/4$. When $g=0$, Equation 6 is maximized which corresponds to pure reflection so that all of the optical energy is contained in I_0. When $g=\lambda/4$ on the other hand, the accrued phase, $2kg$, reduces to π and I_0 vanishes so that the optical energy is distributed among even order intensity components [13, 19-21].

Principles of Diffraction Grating Optical Microphones

A principle schematic of an optical microphone using the presented optical detection method is shown in Figure 8. First, acoustic pressure, P, is converted into membrane displacement, dg, according to the system dynamics. Membrane displacement is then used to modulate light energy. In this case, phase sensitive diffraction gratings accomplish this task. The modulated intensity, I, is then converted into the electrical domain using light sensitive optoelectronic devices such as photodiodes whose responsivity, measured in Amps per Watt (A/W), determines the efficiency with which light power is converted into photocurrent, i. Finally, photocurrent is converted into a proportional voltage signal, v, using a transimpedance amplifier (TIA). In this simple schematic, each stage contributes to the overall electroacoustic sensitivity. The suggested models therefore play a vital role in the optimization of the optical microphone.

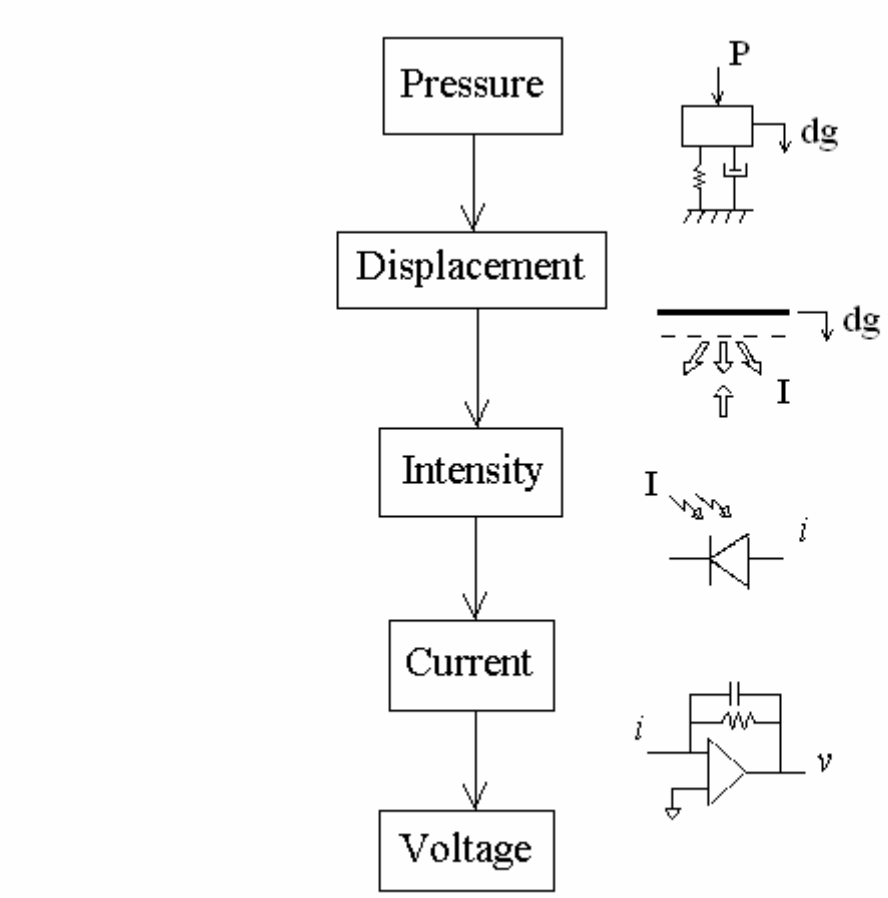

Figure 8. Principle schematic of diffraction grating optical microphones

In the presented optical detection method, the modulation of a given order intensity is a result of gap height fluctuations and for now will be considered to be periodic as Equations 6 suggests. When plotted as in Figure 9, this relationship is referred to as the optical curve and it is this relationship which defines the electrical sensitivity, S_e, of the diffraction grating optical microphone. Figure 9, for example, can also be plotted in the more familiar form of output voltage, v, verses gap height, g, since the induced photocurrent from the diffracted order intensity is scaled proportionally to output voltage during the TIA stage. As Equation 3 requires, the electrical sensitivity is then the derivative of this sinusoidal function. Electrical sensitivity is therefore periodic

as well and it is therefore necessary to calibrate the sensitivity using an electrostatic DC bias voltage, V_{bias}, as shown in Figure 11. In addition to describing the sensitivity of the optical detection method, the optical curve also impacts the dynamic range of the microphone and dictates the fundamental shot noise limitation of the optical detection method for a given bias point.

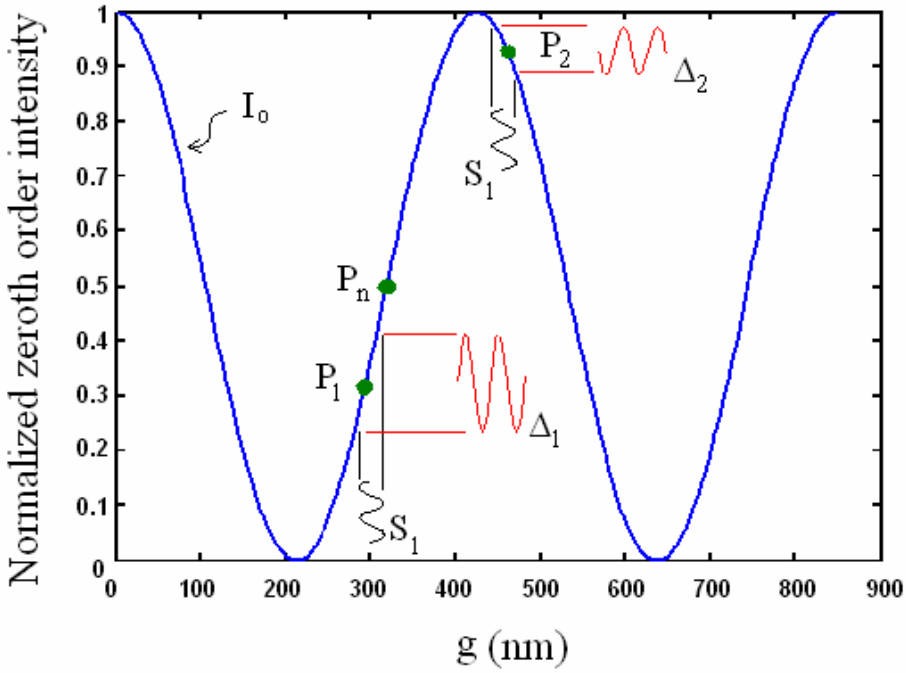

Figure 9. Theoretical optical curve for I_0 order output

Assuming the diaphragm operates about a static equilibrium point, labeled P_1 in Figure 9, small acoustic pressure fluctuations cause the flexible diaphragm to traverse the hypothetical path, S_1. This deviation about P_1 in turn modulates the intensity, I_0, as the optical curve is traced. The result is a variation in zeroth order intensity output shown here as Δ_1. Assuming a less sensitive static equilibrium point P_2, for example, the same hypothetical path S_1 results in an output signal Δ_2. It is in fact the slope of the optical curve which indicates the sensitivity of the optical detection method. Maximum slop and

therefore maximum displacement sensitivity, is found by maximizing the second derivative of the optical curve. Solving for g at these locations leads to a general expression for optimal gap height,

$$g_n = \frac{\lambda}{8} + n\frac{\lambda}{4} \qquad 8$$

In Figure 9, P_n represents a gap height corresponding to maximum displacement sensitivity assuming λ=850nm. Within a finite region of deflection where membrane curvature can be ignored, several optimal gap heights, g_n, may occur. A good approximation for the maximum displacement sensitivity is found by taking the first two terms of the Taylor series expansion about any point, g_n. The magnitude of the slope of this linearized approximation is

$$S_d = \frac{2\pi A_0}{\lambda} \qquad 9$$

where A_0 is the peak to peak amplitude of the modulated signal. When A_0 is taken to be the voltage output from Figure 8 after the TIA, S_d is expressed in units of V/m and is equivalent to electrical sensitivity, *Se*. It is important to realize however, that when the gap height does not correspond to a value g_n, the displacement sensitivity will be less than S_d and can even go to zero when either a maxima or minima is reached on the optical curve. In addition to describing the sensitivity of the optical detection method, the optical curve also plays a role in setting an upper bound on the dynamic range of the microphone. The dynamic range actually depends on the total sensitivity S and it is therefore necessary to take into account the compliance of the diaphragm as well. Again, assuming that the magnitude of the output signal, A_0, is measured in volts, the upper limit

of the microphone's dynamic range is equal to A_0/S in units of Pa. The lower limit of dynamic range is set by the noise floor of the microphone therefore a more complete evaluation of dynamic range will be determined after appropriate noise discussion.

Electrostatic Actuation in Optical Architectures

In order to ensure operation about an optimal point for maximum displacement sensitivity, electrostatic bias is applied between the diaphragm and the grating fingers. The implications of Equation 5, derived from parallel plate theory in Chapter 1 for condenser microphones, are again applicable for the phase sensitive grating structures of optical microphone but are in this case less intrusive to optical detection. In capacitive detection, the bias voltage can often be quite large in order to maximize sensitivity. However, in the optical detection method, large bias potentials are usually not necessary because the initial gap heights can be engineered quite small and the optimal gap heights are separated by only a few hundred nanometers depending on the wavelength of the incident light.

Another distinctive feature of the optical detection method is that the applied electrostatic signals are decoupled from the optical detection readout. One significant consequence of this decoupling is that precisely controlled electrostatic forces can be applied to the diaphragm while the resulting displacement is measured independently. A variety of inputs can be applied via electrostatic excitation in order to obtain the impulse response of the microphone. From this information, frequency response information such as quality factor, Q, resonant frequency, f_0, and usable bandwidth can be obtained. With this data, the thermal mechanical noise limitations of the microphone can be estimated.

In addition to this form of self-dynamic calibration, a second consequence of the decoupled nature of optical detection is that it allows in-situ alteration of the device dynamics. Using a force feedback approach, the dynamic properties of the microphone are tailored by electrostatically inputting an uncoupled proportional feedback signal for application specific operation [22].

Two Michelson Type Optical MEMS Microphones with Integrated Electrostatic Actuation

The optical modeling carried out in this chapter pertains to two particular MEMS microphones which operate under the principles described above. The first is a descendant of the optical microphone design described in Chapter 1. A computer model of this microphone structure, which is fabricated using the SwIFT-Lite™ process at Sandia National Labs, is shown in Figure 10 both with and without the microphone diaphragm. The design consists of a rigid diffraction grating suspended 6μm below a flexible diaphragm by three support arms although one of the arms has been omitted in this depiction. The rigid grating and three support arms are conductive and function as a bottom electrode. The diaphragm itself consists of a flexible 2.25μm thick polysilicon layer and acts as a top electrode. A sacrificial oxide layer is used to precisely control the thickness of the dielectric air gap. A Bosch etch is then used to open a backside volume and define the three rigid support arms. In the final processing step, the sacrificial oxide is removed and the diaphragm is released. After the backside of the microphone structure is sealed, this microphone is able to respond uniformly to pressure from any given direction. The resulting structure is therefore similar in many ways to an omnidirectional condenser microphone [13].

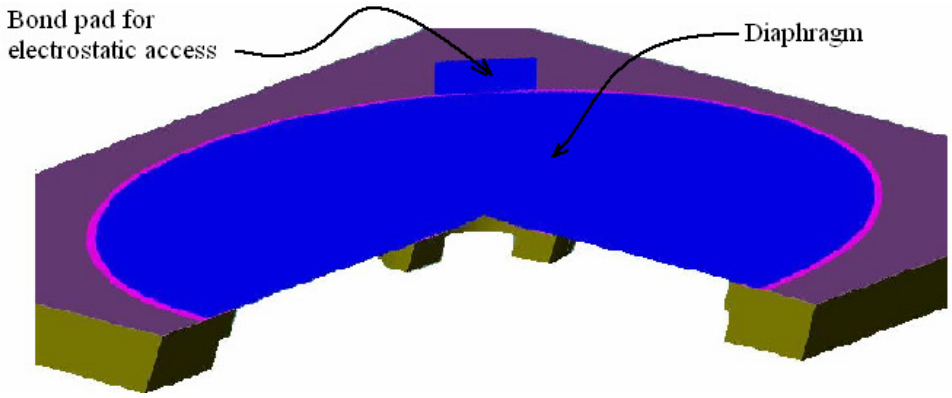

a)

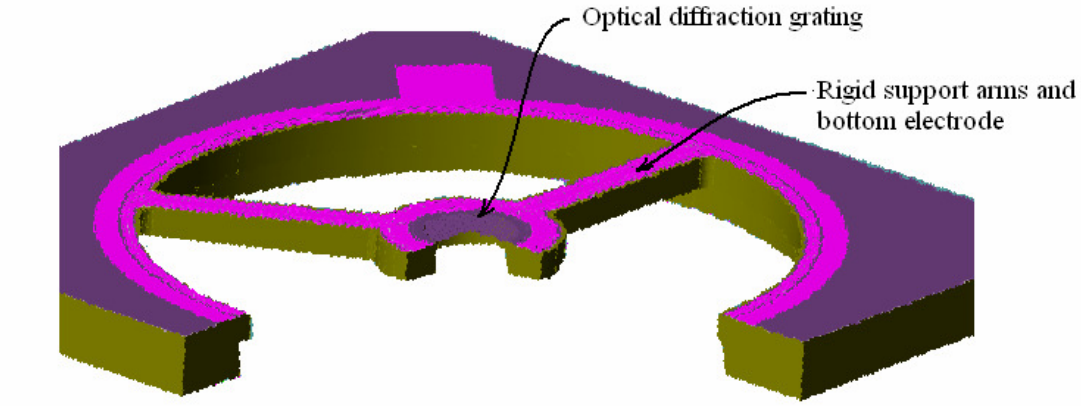

b)

Figure 10. Omnidirectional microphone structure

A profile illustration of the 2mm omnidirectional microphone with integrated optical detection is shown in Figure 11 and is clearly fashioned as a phase sensitive diffraction grating structure. The incident light source, I_{in}, is positioned to illuminate the grating region from the backside of the microphone. The actual grating region is approximately 200µm and can be viewed from the backside of the microphone using high power magnification as seen in Figure 12a. The fingers themselves form a 4µm period grating and can be viewed under higher magnification in Figure 12b. Photodiodes are

then placed to capture the refracted zeroth and first orders intensity components although only the first order photodiode pair is shown in Figure 11.

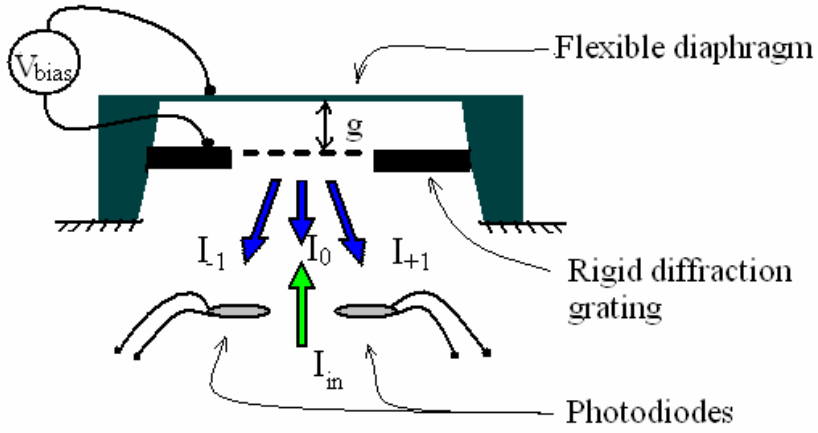

Figure 11. Optical detection method for the omnidirectional microphone

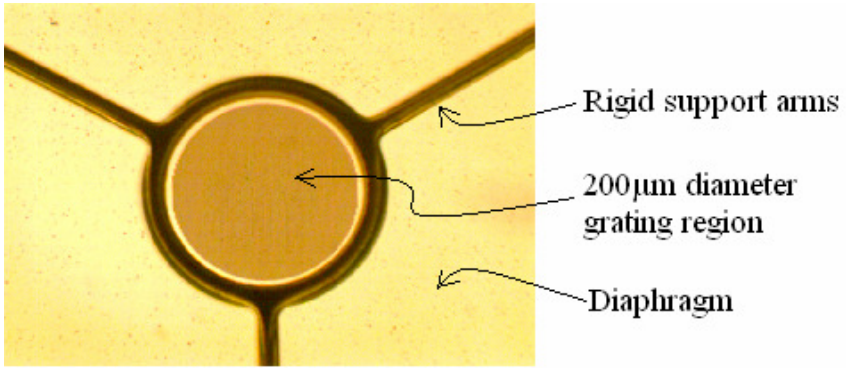

a)

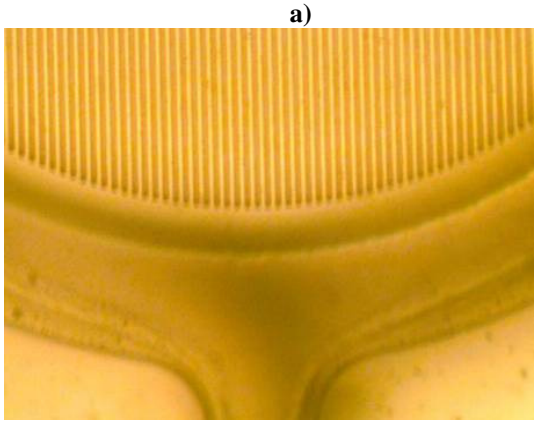

b)

Figure 12. Backside view of the omnidirectional microphone showing a) rigid 200µm diameter diffraction grating suspended by three support arms b) enlarged view of 4µm grating period

The same phase sensitive diffraction grating principle is incorporated into the unique biomimetic directional microphone design. Here, a 4µm period grating is located on the diaphragm itself while a gold cantilever, shown in Figure 5, remains stationary and serves as the second reflective surface. Figure 13 is a magnified image of the grating region viewed from the backside of the microphone. This grating region is approximately 100µm x 100µm and is considerably smaller than the omnidirectional optical microphone grating. Although it is beneficial in terms of reducing damping effects, this smaller optical region is less ideal for optical detection as will be seen.

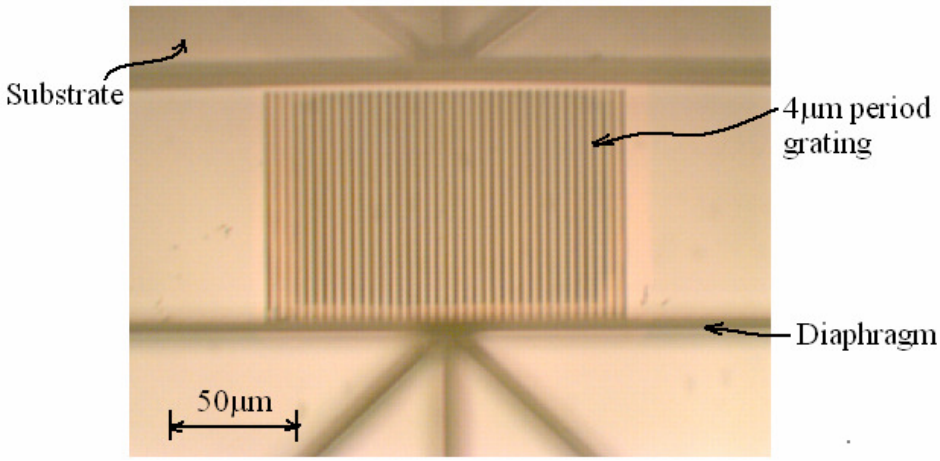

Figure 13. Movable 4µm period diffraction grating located on the diaphragm of the biomimetic directional microphone

Geometric and Mathematical Modeling of Phase Sensitive Diffraction Gratings

Mathematical derivations of an intensity profile in the optical field begin with well known scalar diffraction theory. The two-dimensional optical distribution in a plane of observation, $u(x_i,y_i)$, resulting from an aperture function, $G(x_o)$, is given by the Fresnel-Kirchhoff diffraction formula

$$u(x_i, y_i) = \frac{1}{i\lambda} \int_{-\infty}^{\infty} \int_{-\infty}^{\infty} G(x_o) \frac{e^{-ikr}}{r} dy_o dx_o \qquad 10$$

Here, r is the distance from a point on the aperture, (x_o,y_o), to a point, (x_i,y_i), located on the plane of observation as described by Figure 14.

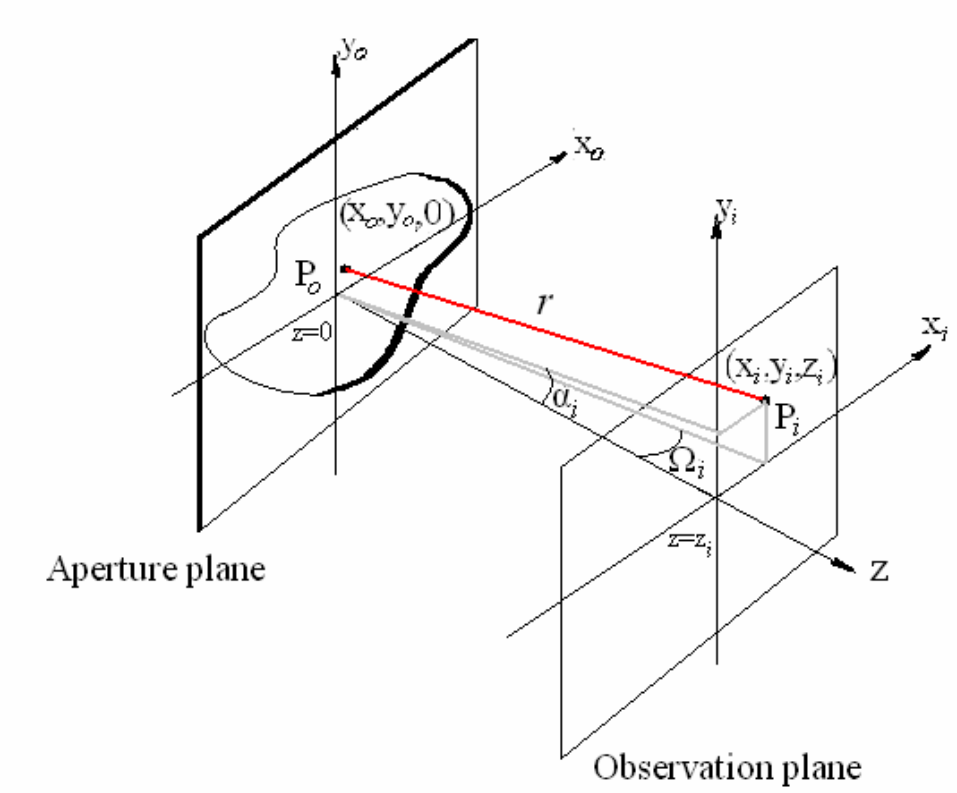

Figure 14. Geometric model used for Fresnel-Kirchhoff diffraction formula

The value of r is expressed geometrically as

$$r = \sqrt{z_i^{\,2} + (x_0 - x_i)^2 + (y_0 - y_i)^2} \; . \qquad 11$$

Integration of Equation 10 becomes difficult due to the squared terms introduced in the expression for r. Approximations are therefore made which make use of binomial expansion and are based on the ratio between the distance z_i and the size of the aperture.

The simplest of these approximations is known as the Fraunhofer approximation and occurs when the characteristic length of the aperture, L, is small enough to satisfy the expression $z_i > L^2/\lambda$. For a simple grating which varies only in one dimension, L is equal to the grating pitch, d. When $z_i < L^2/\lambda$, an extra term from the binomial expansion is incorporated in the approximation for r and the region satisfying this condition is known as the Fresnel region. Note that when z_i becomes much less than L^2/λ, the binomial expansion is no longer valid. The Fresnel and Fraunhofer approximations however, apply for a large number of problems and simplify Equation 10 considerably. Assuming the wavelength of incident light to be 850nm, the Fraunhofer approximation becomes valid at z_i=19μm for a 4μm grating period. Despite these small length requirements, the more accurate Fresnel approximation is used to simulate the optical field and to account for light source divergence which is not possible using the Fraunhofer approximation. The Fresnel approximation for Equation 10 is

$$u(x_i, y_i, z_i) = \frac{1}{i\lambda z_i} \exp\left[ik\left(z_i + \frac{x_i^{\,2} + y_i^{\,2}}{2z_i} \right) \right] \times \Phi \qquad 12$$

where Φ represents the two-dimensional Fourier transform of the complex grating function.

$$\Phi = \Im\left\{ G(x_0, y_0) \exp\left[\frac{jk(x_0^{\,2} + y_0^{\,2})}{2z_i} \right] \right\} \qquad 13$$

Assuming variation along the dimension x_0 only, an appropriate grating function for the imposed phase shift of a 4μm period grating region is shown in Figure 15 where d is the grating pitch and $d/2$ is the finger width.

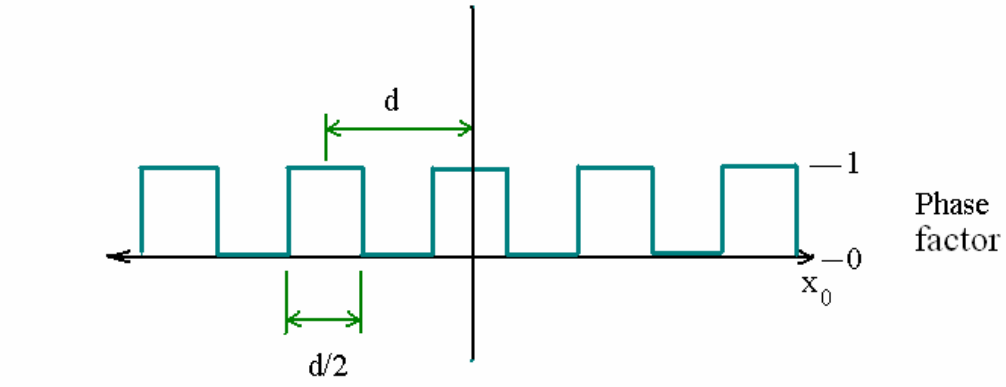

Figure 15. Grating function for simple grating case

In Equation 13, however, $G(x_0,y_0)$ represents both the magnitude and phase of the grating function. The magnitude of the grating function remains unity for all values (x_0,y_0) assuming (for now at least) that both the grating and the diaphragm are reflective and do not absorb or transmit any incident optical power. It will be shown later in this chapter that this is not the case. In Figure 15, phase values of zero correspond to locations where the incident light encounters the optical grating and reflects straight back towards the observation plane without accruing any additional phase. Regions where the phase is unity, on the other hand, correspond to locations where the incident light passes through the grating and accrues a phase value which is dependent on gap height [23, 24].

Microscale Implementation and Optical Modeling

Commercially available optoelectronic devices such as photodiodes and single mode vertical cavity surface emitting lasers (VCSELs) are used primarily in fiber optic data transmission and are capable of meeting both the size and performance requirements of the micro-optical detection method. Discrete micro-optoelectronic components are shown in Figure 16. According to manufacturer's specifications, polysilicon photodiodes

measure 250µm x 250µm x 150µm with an active area diameter of 100µm and a responsivity of .5A/W [25]. A VCSEL, emitting single mode 850nm wavelength light is also available in a similar discrete package and the quoted performance characteristics are supplied in Table 1. A simple design for implementing the proposed optical detection

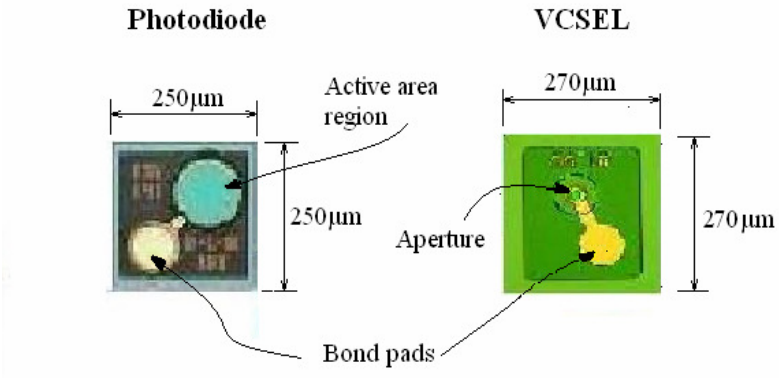

Figure 16. Micro-optoelectronic components

Table 1: VCSEL properties

Wavelength	850nm
Divergence angle	8°
Optical power	2mW
Operating current	6mA
Series resistance	150Ω

method is shown in Figure 17. The design is configured to capture I_0, I_{+1}, and I_{-1} via three discrete photodiodes. These orders contain an overwhelming majority of the optical power and therefore higher orders intensity signals are sacrificed in this design. Because the zeroth order component of the diffraction pattern returns directly back towards the VCSEL aperture, a significant portion of optical power is lost in this design. Other configurations combining tilt and/or focusing optics are potentially capable of recapturing a greater percentage of the signal power contained within the diffracted orders, although these designs are substantially more complex in terms of assembly and optical alignment, and they are likely to occupy larger volumes.

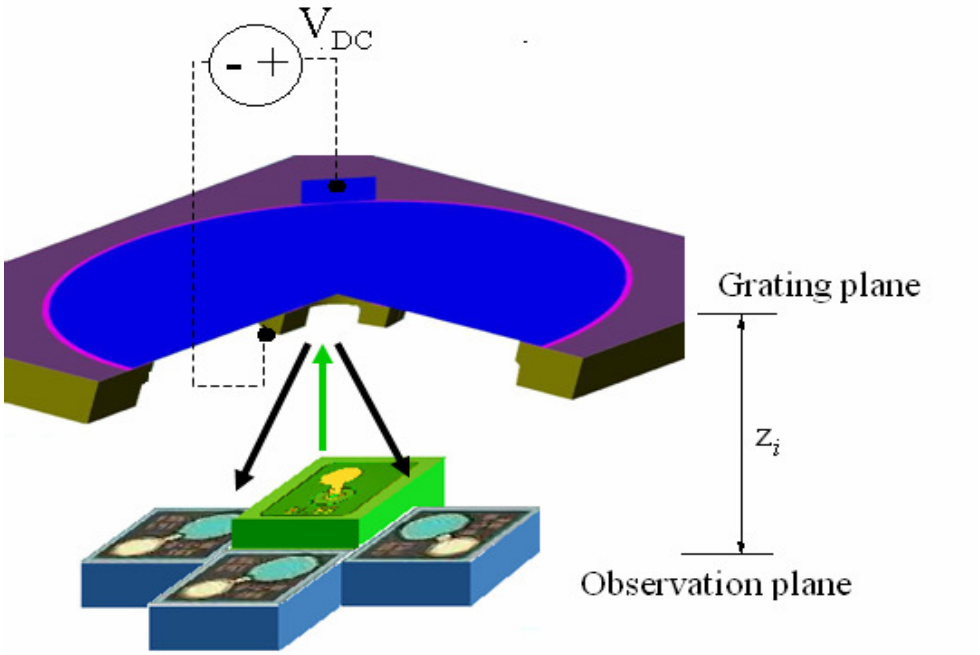

Figure 17. Concept of optoelectronic integration

One drawback of excluding focusing optics in the micro-optical design is that the divergence angle of the VCSEL source has a negative impact on the modulation performance of the diffracted orders. Current technology has improved upon VCSEL divergence angles and the value of 8° listed in Table 1 is considered exceptional [26]. Another disadvantage of VCSELs is that they exhibit relatively high levels of laser relative intensity noise (RIN). Certain techniques, however, can be used which eliminate RIN down to shot noise limitations of the optoelectronics. Details regarding this process are provided in the next chapter [12, 13].

Because of its effect on the displacement sensitivity of the optical detection method, it is important to include the effects of VCSEL divergence in the optical simulation. In an ideal situation, a collimated beam of light illuminates an infinite grating. Theoretical derivations in this situation lead to a simple diffraction grating

equation which governs the angles of the diffracted orders. These angles depend only on the grating period and the wavelength of collimated light source, and are given by

$$\Omega_m = \sin^{-1}\left(\frac{m\lambda}{d}\right) \tag{14}$$

where Ω_m designates the diffraction angle of the m^{th} diffraction order corresponding to the Fourier coefficient F_m from the Fourier representation of the diffraction grating. In the ideal situation, Ω_m designates the locations at which maximum intensity modulation occurs [24]. However, a computer simulation which is provided in Appendix A takes into account the divergence of the VCSEL light source using Gaussian beam propagation and shows that the ideal locations for optoelectronic placement do not coincide with theoretical diffraction angle calculations. In order to simulate the VCSEL radiation, an aperture beam waist, w_0, is chosen which produces the appropriate divergence angle. An approximation for the relationship between a Gaussian beam waist, w_0, and the far-field divergence angle, γ, is given by

$$w_0 \cong \frac{\lambda}{\pi\gamma}. \tag{15}$$

A VCSEL divergence angle of 8° (half angle beam divergence) therefore requires a beam waist of approximately 2μm [27].

Once an appropriate approximation for the VCSEL source is constructed, the computer simulation examines the two extreme cases of total reflection and total diffraction in order to determine the optimal separation distance, z_i, between the grating plane and the observation plane. Recall that total reflection occurs when I_0 is maximized and total diffraction occurs when $I_{\pm 1}$ is maximized. In other words, the corresponding

gap-dependent phase addition, φ, is equivalent to 0 and π respectively. Cross sections of the intensity profiles taken at $y_i=0$ for these phase values are shown together in Figure 18. Figure 18 clearly illustrates the overlapping of diffracted order intensities caused by divergence of the VCSEL source. The two dimensional intensity profiles from which Figure 18 were obtained, are shown in Figure 19 for cases $\varphi=0$, $\varphi=\pi$, and $\varphi=\pi/2$.

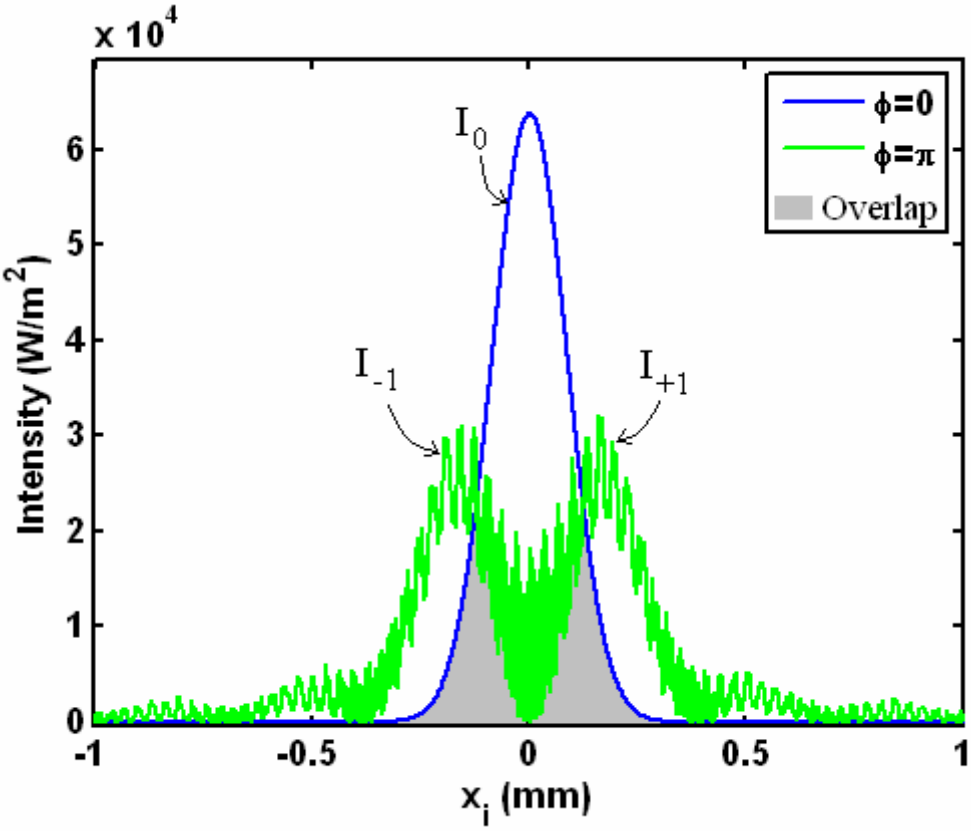

Figure 18. Relevant intensity profiles along $y_i=0$ for $z_i=900\mu m$

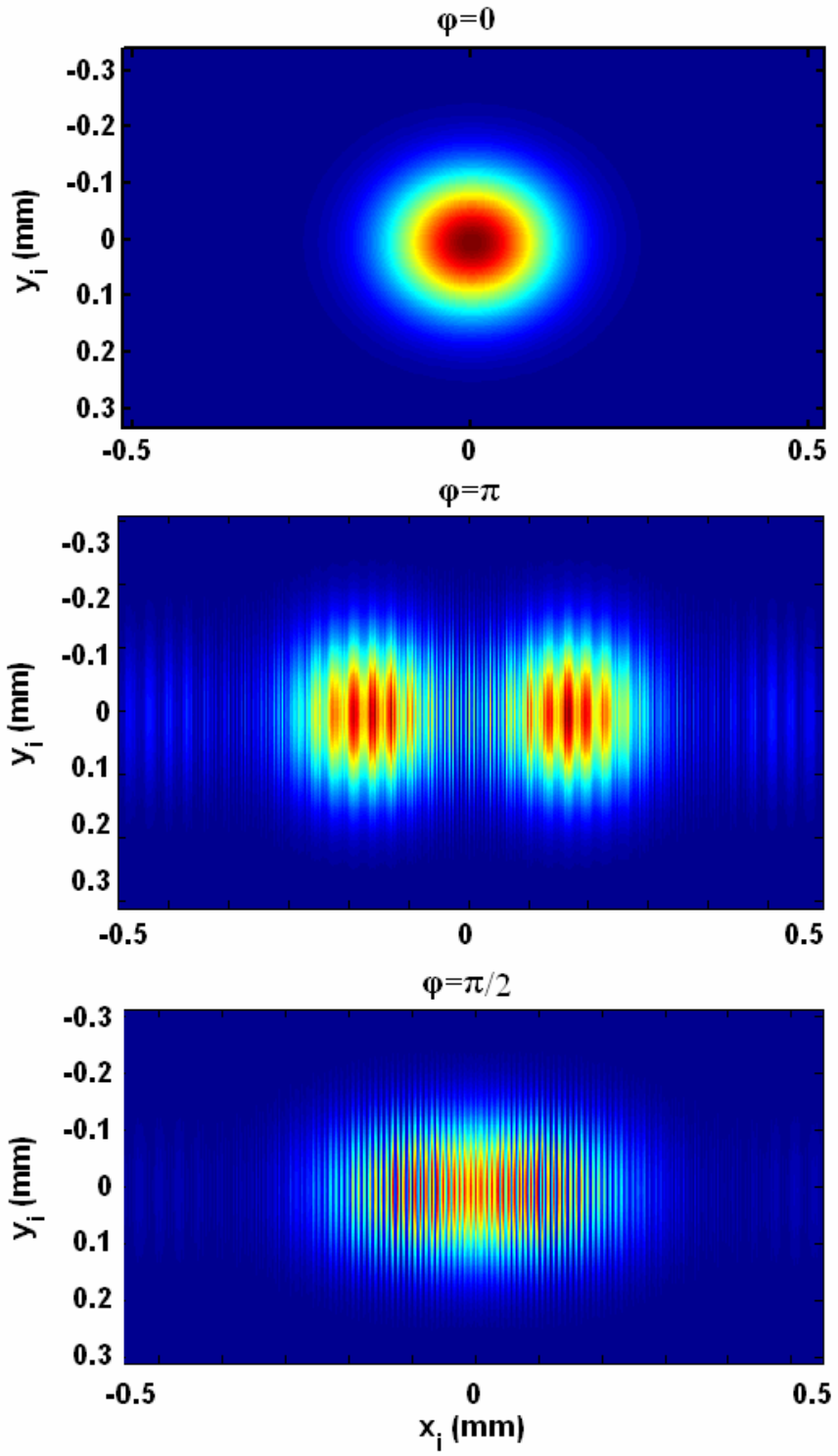

Figure 19. Two dimensional intensity profiles for a 4μm grating period simulated for φ=0, φ=π, and φ=π/2 at z_i=900μm

Overlapping of intensity orders is especially evident when $\varphi=\pi/2$ which corresponds maximum displacement sensitivity. It will be shown that this overlap is responsible for a DC offset in the optical modulation resulting in sensitivity degradation and increased shot noise levels. According to Equation 14, it is possible to achieve more pronounced order separation by increasing the wavelength of the light, or by decreasing the period, d, of the grating structure. However, standard VCSEL wavelengths are on the order of 850nm and are limited by material properties of the quantum well. At these wavelengths, reducing the grating pitch can increase polarization effects [28]. Therefore, there is little room for improvement in the microscale system without the use of focusing optics. Nevertheless, additional simulations predict that it is possible to achieve reasonable modulation given the proposed simple architecture.

A scale drawing of the two dimensional intensity profiles with superimposed optoelectronic components shows the approximate locations of the photodiode active areas for different diffraction patterns (see Figure 20). Placing the VCSEL and photodiodes as close together as possible minimizes the size of design and leads to z_i becoming the independent variable in the optimization process. Note from Figure 20 that the largest dimension in this design is less then 1mm. In order to assess the performance of the optoelectronic design at a location in the field, it is appropriate to estimate the theoretical optical curve. This is done by evaluating u from Equation 12 at a separation distance z_i for a range of gap heights which satisfy $0<\varphi<2\pi$ and then integrating each result over the photodiode active area regions to estimate the amount of light power that is captured as a function of gap height. The result, shown in Figure 21, does indeed confirm that due to the overlap caused by VCSEL divergence, a significant DC offset is

present in the captured optical power and is especially pronounced when the photodiodes are placed too close to the VCSEL or when z_i is too large. However, minimizing this DC offset leads to a reduction in captured signal and therefore a compromise must be reached. This compromise is reached by quantitatively comparing the inverse relationship between the predicted displacement sensitivities and the predicted shot noise levels for a range of gap heights and leads to an optimal value of approximately 900µm for z_i.

The maximum displacement sensitivity, S_d, is obtained from Figure 21 and Equation 9 as 35mV/nm assuming a 200kΩ feedback resistance in the TIA stage. This assumption also leads to a predicted level of -127dBV/√Hz. Therefore, assuming the system is shot noise limited, predicted displacement resolution can be calculated as 12fm/√Hz for a single 1st order output. This estimated displacement resolution provides a sense of the absolute best performance of the proposed optical detection packaging scheme.

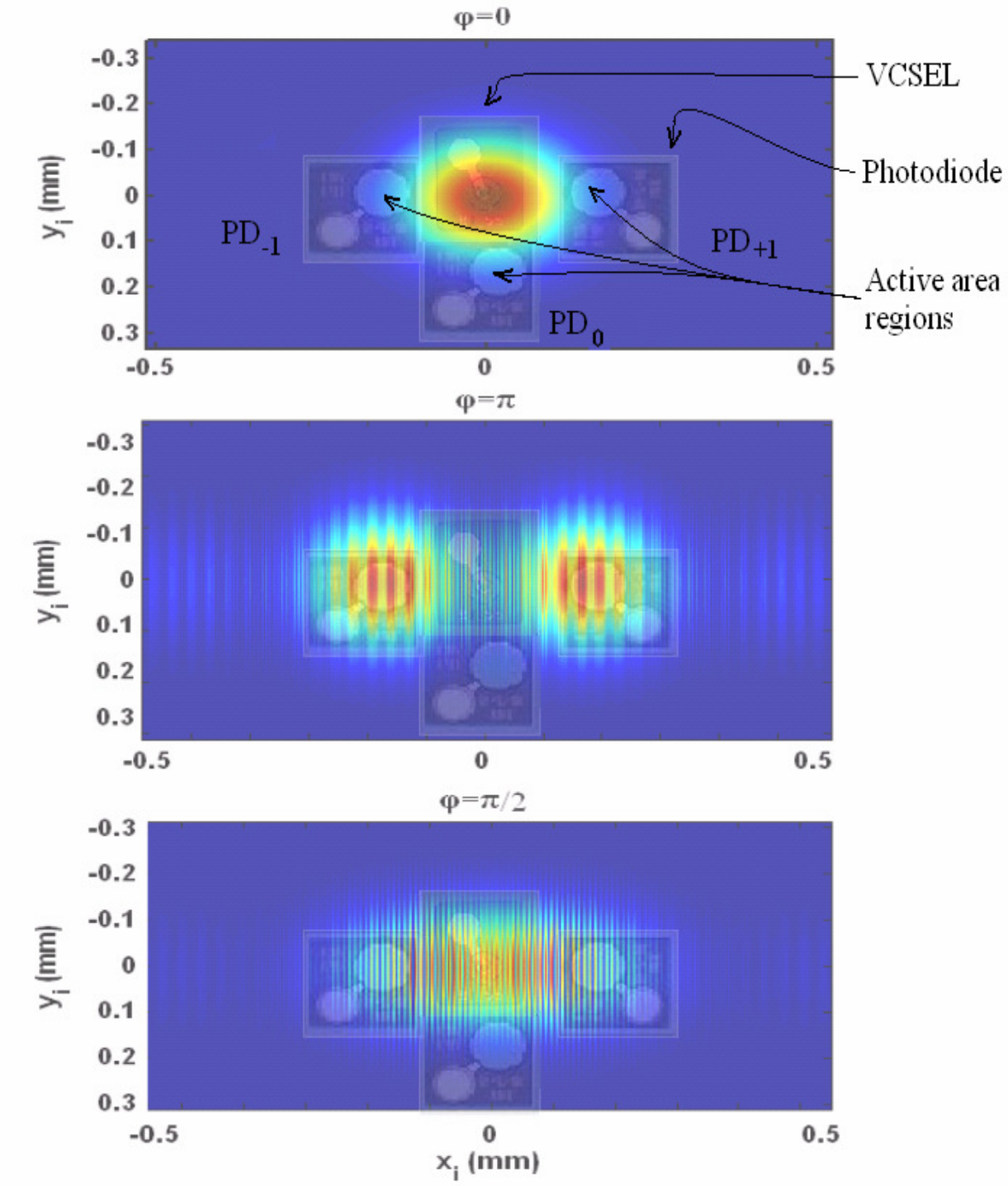

Figure 20. Diffraction patterns for a 4μm grating period with superimposed optoelectronics showing the locations of photodiode active area regions

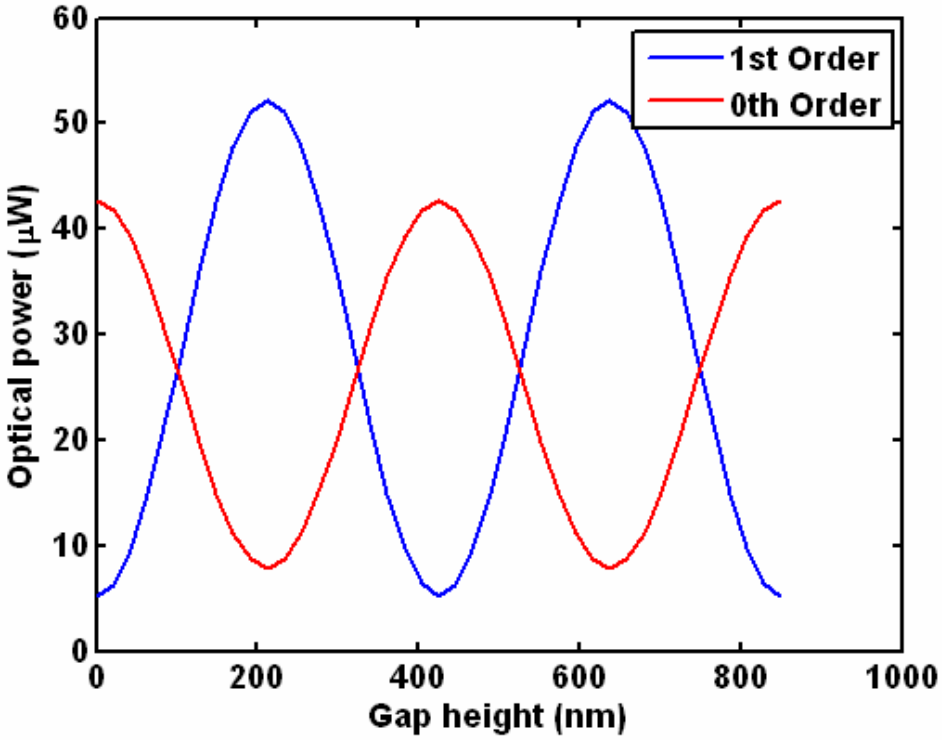

Figure 21. Ideal simulation of the optical curves for omnidirectional microphone structure at z_i=900μm showing DC offset due to VCSEL divergence

One assumption made by the optical simulation is that both the grating and the diaphragm behave as perfect mirrors. However, without adequate reflectivity of the grating and the diaphragm surfaces, a significant portion of optical power can be lost to either absorption or transmission. In order to explain these effects and to roughly estimate loss of optical power, consider the thin film refraction model shown in Figure 22 which describes the actual behavior of the 2.25μm thick polysilicon diaphragm. First, the value of the incident beam I_{in} is set to unity in order to generalize the problem. As it traverses the path 123, the incident beam is divided into reflected and transmitted

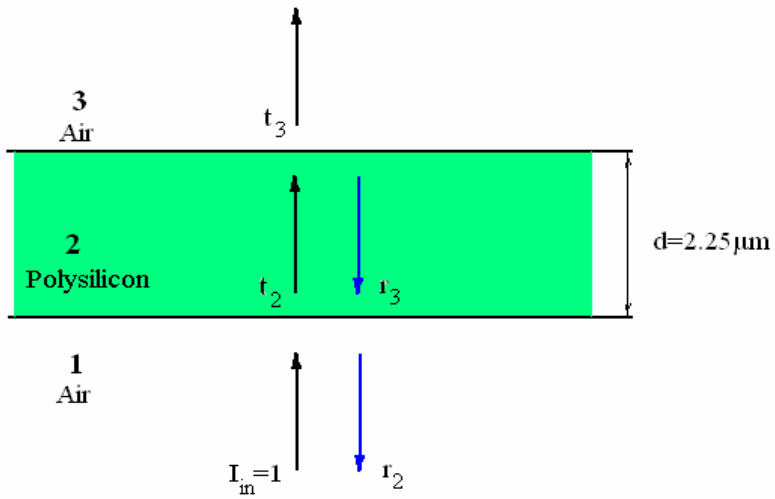

Figure 22. Active boundary layers of the omnidirectional polysilicon diaphragm with unity amplitude incident light beam

portions at each interface according to the Fresnel coefficients

$$r_i = \frac{n_{i-1} - n_i}{n_{i-1} + n_i}, \quad t_i = \frac{2n_{i-1}}{n_{i-1} + n_i} \tag{16}$$

where n has both real and imaginary parts, $n = \bar{n} - \bar{k}\mathrm{i}$. The imaginary portion of n is known as the extinction coefficient and is responsible for absorption effects according to the amplitude attenuation factor, $\exp(-\frac{2\pi\bar{k}d}{\lambda})$. At 850nm wavelength, the extinction coefficient for polysilicon is quite small and the diaphragm exhibits negligible absorption. Although the optical properties of polysilicon thin films depend heavily on deposition and post-processing recipes, a value of n_2=4 is assumed for the polysilicon diaphragm while the standard value n_1=n_3=1 is prescribed for air [29].

Figure 22 is actually a simplification of the infinite reflection and transmission occurrences within the active layer. In order to calculate the total reflection and

transmission, an infinite sum must be carried out. The resulting equation for the total transmission loss, in the case of the polysilicon diaphragm of the omnidirectional microphone can be derived as

$$T = n_3 \frac{t_2^{\,2} t_3^{\,2}}{1 + r_2^{\,2} r_3^{\,2} + 2 r_2 r_3 \cos(2\Delta)} \qquad 17$$

where $\Delta = n_2 \frac{2\pi d}{\lambda}$ and d is the thickness of the diaphragm. From conservation of energy and the fact that absorption can be neglected, it follows that the reflection coefficient satisfies R=1-T [30, 31]. Following this derivation, the transmission coefficient for the polysilicon active interface is found to be T=.506 meaning that ~51% of the light which actually reaches the omnidirectional microphone diaphragm will be lost from the optical detection system to the surroundings. In order to reduce transmission through the diaphragm, a thin metallization layer can be deposited on the backside of the device to increase reflectivity so long as the grating remains electrically isolated from the diaphragm. Transmission effects, as well as other effects such as polarization and membrane curvature, are not taken into account in the sensitivity calculations obtained from Figure 21. Nevertheless, the previous optical modeling provides valuable insight into the behavior of the micro-optical system for the optimal selection of z_i.

Comments on Noise, Dynamic Range, and Power Consumption

Before closing, this chapter addresses two final aspects regarding the feasibility of microscale integration of the optical detection scheme. Namely, these aspects include optical noise, dynamic range, and power consumption. It is well known that

optoelectronic devices are the dominate source of noise in optical microphones and this is especially the case in phase modulating optical microphones which are susceptible to phase noise and intensity noise. These noise levels have the potential to set the lower limit of the microphone's dynamic range will the upper limit of this range is set by the optical modulation curve as mentioned previously. Power consumption is also a matter of concern for optical microphones which potentially limits their application domain. However, there are clever and relatively simple ways of addressing these issues.

Noise in optical system comes in many forms. In this discussion, the first two relevant sources of noise include RIN and phase noise and are both intermodulated with the VCSEL output and consequently the diffracted order outputs. An additional uncorrelated shot noise component is also added to the signal during the conversion of the optical signal into photocurrent and imposes the ultimate limitation for noise performance of optical microphones [9]. First, consider the additive RIN component which is proportional to the amplitude of the DC source intensity. After this source undergoes diffraction, the separated orders I_0 and $I_{\pm 1}$ exhibit an antiphase nature as evidenced by Equations 6 and 7 while the RIN component remains in phase. It can be shown that by scaling and then differencing the electronic representation of these orders, it is possible to eliminate the correlated RIN component while retaining and summing the complementary signals. Unfortunately, this technique, known as differential order detection, is unable to eliminate phase noise of the laser source which can be particularly prevalent in interferometric detection schemes which rely on phase information. In micro-optical systems, however, phase error tends to remain quite small since the propagation distance between the grating and the reflective surface is relatively small

compared to the optical wavelength and for this reason phase noise contributions are negligible [32]. The final noise component to consider is obviously the shot noise component and in the voltage domain it is defined as

$$v_{shot} = \sqrt{2qR_{fb}V_{DC}} \tag{18}$$

where q is the elementary electron charge, R_{fb} is the feedback resistance of the TIA, and V_{DC} is the DC voltage offset after the TIA stage. Since the shot noise components of each photocurrent are uncorrelated with one another, it is impossible to eliminate them using differential order detection and thus this technique is theoretically shot noise limited. The total shot noise level of the output using this technique is actually determined by the Euclidean norm of the contributing order intensities. Differential order detection for two complementary orders with equal amplitudes therefore leads to a total shot noise level which is 3dB greater than that of a single order. Meanwhile, the reduction in common mode intensity noise can be as much as 60dB in noisy sources. The electronic implementation of this process is not void of stipulations, however, and conventional circuits employing multiplication or division operations usually fall short of shot noise limitations due to the inherently higher noise levels of these integrated circuits. Furthermore, these circuits also tend to exhibit fastidious requirements on the amplitudes and ratios of the antiphased orders [9, 12].

As shown already, the optimal performance of the presented micro-optical detection scheme predicts a displacement resolution of 12fm/√Hz for shot noise limited detection. If this value is taken to be the lower limit of the dynamic range, the upper limit is equal to λ/4, or 212nm for an 850nm light source, which is the maximum detectible

displacement allowed by the optical curve as seen in Figure 21. It has been shown that displacement of this magnitude produces a total harmonic distortion (THD) level below the 3% standard for calculating dynamic range. Converting the ratio between maximum and minimum detection levels into dB units gives a predicted dynamic range on the order of 145dB.

For a number of applications, power consumption of the optical detection method weighs heavily on the potential of optical microphones. Power consumption for continuous VCSEL operation above threshold for instance, is approximately 5.4mW which is calculated from the properties given in Table 1. In comparison, several miniaturized microphones for cell phone and hearing aid applications consume power on the microwatt scale. However, by pulsing the VCSEL at a rate suitable for audio bandwidth, a reduction in optical power by a factor of 10^{-6} is theoretically possible depending on the duty cycle. VCSEL's are well equipped to handle pulsed operation well beyond frequencies which satisfy the Nyquist criterion for the audible bandwidth. Photodiodes are equally capable in this mode of operation provided their junction capacitance is small. Although pulsed VCSEL operation is not demonstrated in the results of this thesis, this mode of operation demonstrates the versatility of the optical detection method at the microscale and further supports this optical method as a viable alternative to capacitive detection in small scale microphones [12, 19].

.

CHAPTER 3

IMPLEMENTATION OF MICROSCALE OPTICAL DETECTION

Microscale packaging of the presented optical detection method for MEMS optical microphones is carried out with three main goals in mind: 1) decrease sound field disturbance by minimizing package size; 2) demonstrate high sensitivity optical microphones within mm^3 volumes; and 3) obtain antiphased intensity readout for noise reduction algorithms. Previous packages employing the present optical detection method have demonstrated sufficient displacement resolution to achieve microphone structures with 17dBA internal noise floors. However, these package designs incorporate both focusing optics as well as tilted configurations which require substantial working distances and volumes. Furthermore, these microphone test beds are equipped with a single laser source and are unable to accommodate efficient device testing much less the simultaneous testing of an array of microphones. A final disadvantage of these experimental setups is the repetitive and laborious nature of the optical alignment process which requires accuracy down to several tens of microns. Therefore, using the micro optoelectronic components which were modeled in the previous chapter, an apparatus was designed to accomplish the stated goals as well as to overcome a number of these limitations. Packaging and fabrication details as well as a detailed description of the suggested noise cancellation circuitry are provided in this chapter.

Integrated Optical Microphone Array Platform (IO-MAP)

The construction of an integrated optical microphone array platform (IO-MAP) was motivated by the desire to collect meaningful acoustic data in an efficient manner using sub-1mm^3 optical detection architecture. The modular design was based on commercialized measurement microphones structures such as the Larson Davis Model 2541 ½ inch microphone which is ideal for free-field acoustic measurements. However, in addition to sharing essentially the same form factor as these instrumentation microphones, the IO-MAP is designed to support simultaneous testing of multiple optical microphones.

The IO-MAP design can be divided into three main assemblies. The first and most distinguishing assembly is the microphone header which contains the micro-optoelectronic components in the configuration established in the previous chapter. The microphone header along with its accompanying electrical routing elements, are modeled using SolidEdge computer aided design (CAD) software and an exploded view of the microphone header showing these elements is provided in Figure 23. A twelve-pin transistor outline header (TO-header) functions as the first routing element as well as the structural platform for the optical detection scheme. A custom PCB is the second routing element and in addition to providing convenient accesses for wirebonding, it also assists with the correct positioning of the optoelectronic components. A spacing element, fashioned using rapid prototyping stereolithography (SLA) material, is designed to supply the optimal microphone height, z_i. The SLA spacer also fulfills other functional aspects which are designed to optimize the microphone performance. A fabricated microphone header is shown in Figure 24. The second assembly of the IO-MAP consists

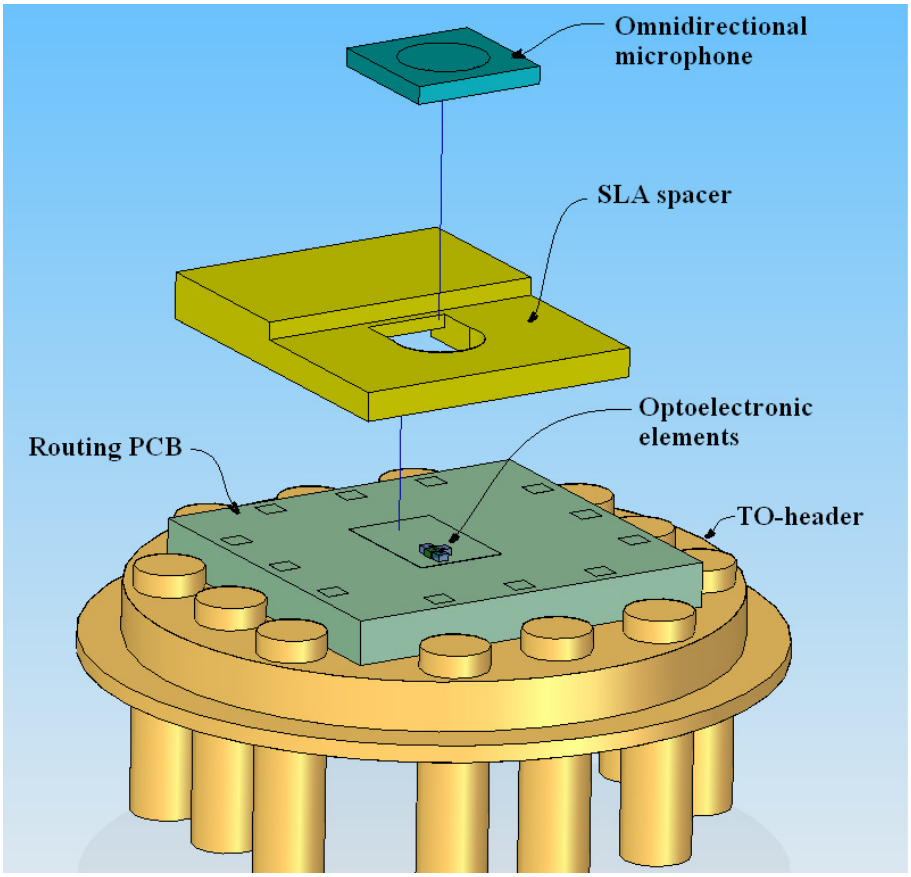

Figure 23. Exploded view of the microphone-header assembly

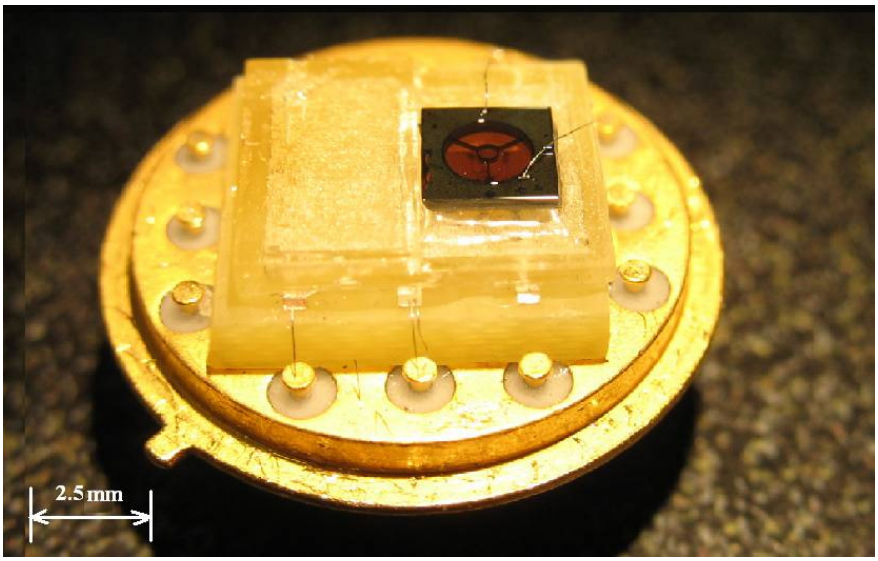

Figure 24. Fabricated omnidirectional microphone-header assembly

of a preamplifier tube and a multi-channel LEMO® extension cable. More details regarding the functional electronics within the preamplifier tube are provided in the following section as well as more advanced circuitry designed to achieve RIN cancellation down to shot noise limitations. The ten-meter long 12-channel LEMO® extension cable is useful for anechoic chamber testing and is shown along with the preamplifier tube in Figure 25. The necessary electronics are easily housed within the shielded tubing as seen in Figure 26 and the layout for the PCB used to package these electronics is provided in Figure 70 of Appendix D.

Figure 25. IO-MAP preamplifier tube and LEMO extension cable assembly

Figure 26. Preamplifier tube with packaged electronics

The third assembly is the IO-MAP routing box which provides a shielded environment for battery power supply as well as convenient I/O BNC ports to and from the LEMO® connector. The box assembly is shown in Figure 27.

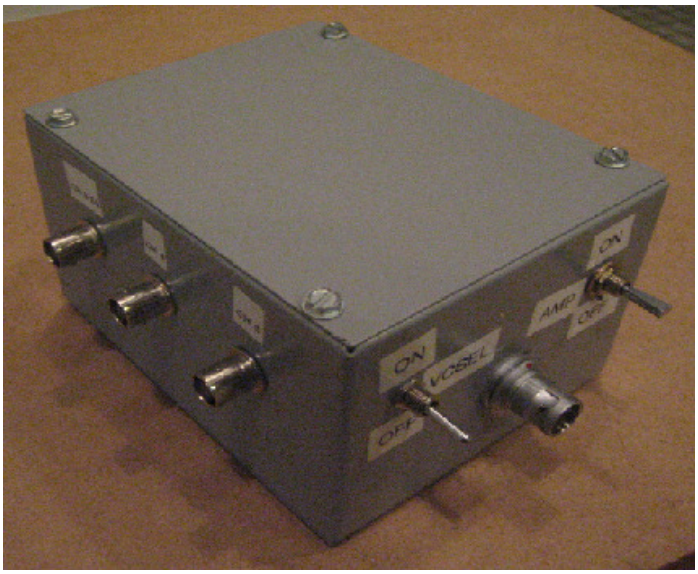

Figure 27. IO-MAP routing box for power supply and BNC I/O access

Microphone Header Fabrication Procedure

Of the various IO-MAP assemblies, the header assembly performs the most defining role of the optical microphone and involves the greatest amount of packaging effort. Some critical steps of the fabrication process include; 1) optoelectronic placement 2) microphone alignment and sealing, and 3) electrostatic connection.

Step 1: Optoelectronic Placement

Before placing the optoelectronic components onto the appropriate 8mm x 8mm routing PCB, the PCB should be rigidly attached to the TO-header using superglue. Figure 28 and Table 2 establish an important numbering scheme which is followed throughout the IO-MAP and the placement of the PCB on the TO-header depends on this

numbering scheme. For example, the ground trace on the PCB, which is also the cathode for both the VCSEL and the photodiodes, should be located next to pin 9. After the PCB is attached in the proper orientation, a minute amount of conductive thermal epoxy is used to attach the cathode of each discrete optoelectronic component to the appropriate PCB trace. Great care should be taken to ensure that these components lie perfectly flat against the PCB to avoid tilting of the beams. A clean glass slide may be used to apply pressure on top of these devices once they are mounted and before curing on a hotplate. As the optical modeling suggests, the placement of these devices is critical. The 1st order photodiode should be placed such that the active region is centered between 250-300µm from the VCSEL aperture while the 0th order photodiode should sit as close as possible to the VCSEL aperture. Once these components are cured, wire bonds are made to the appropriate traces keeping in mind that channel numbering throughout the IO-MAP should correspond to the TO-header pin numbering (see Figure 28 and Table 2).

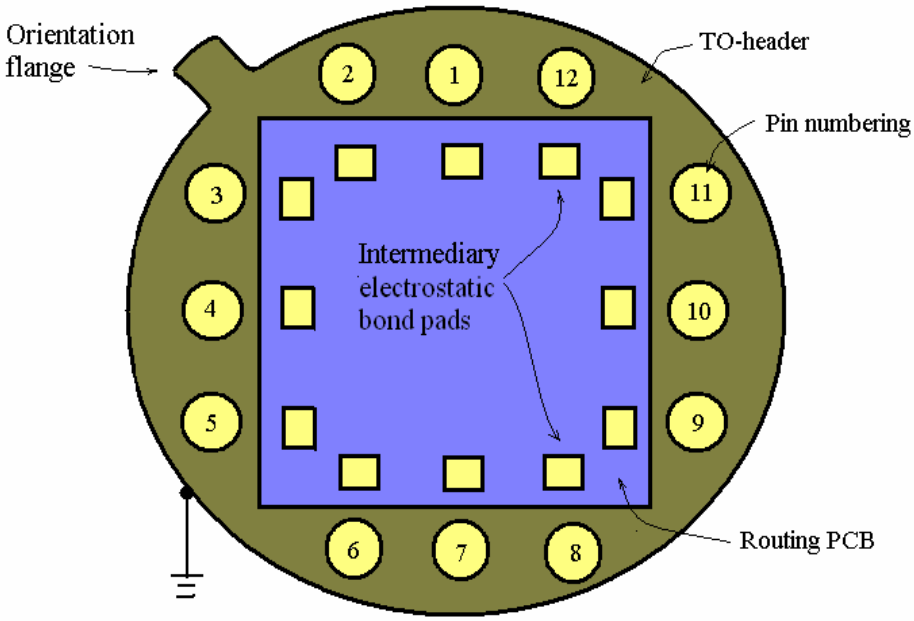

Figure 28. Header orientation and numbering scheme

Table 2: Channel and pin numbering scheme

Channel (Pin) Number	Description
1	N/A
2	PD output
3	PD output
4	PD output
5	PD output
6	N/A
7	V+
8	Electrostatic Supply
9	VCSEL and PD cathode (Also common ground)
10	VCSEL Power
11	V-
12	Electrostatic Supply

Note that V^+ and V^- cannot be accessed at the header level. When using this numbering scheme, the TO-header flange should always be orientated in the upper left quadrant. This orientation flange is also critical when mounting the header onto the preamplifier tube of the IO-MAP. The tube assembly itself is equipped with a custom SLA socket which designates the proper orientation of the header via a crescent shaped notch.

Step 2: Microphone Alignment and Sealing

The next task is to align the microphone so that the VCSEL illuminates the grating region. A few instruments which are necessary for accurate alignment should be prepared prior to this point. First, because the VCSEL wavelength is outside the visible spectrum and can be harmful to human eyesight, magnification with infrared sensitivity (in the form a CCD camera for example) is needed in order to view the VCSEL light during alignment. Secondly, a stable, variable current source is needed to drive the VCSEL during alignment. This source should not exceed 6mA and should be capable of

supplying currents as low as 1-2mA. With these instruments in place, the microphone can be position accurately.

Microphone alignment begins by positioning the SLA spacer as shown in Figure 23 so that the void in the SLA material is situated with the VCSEL in the center. The SLA spacer provides not only the appropriate z_i spacing, but also a 14-fold increase in the back cavity volume. For this reason, the SLA spacer is fixed in place using UV-cured epoxy to ensure that there are no air gaps between the SLA and the PCB. Next, the TO-header should be mounted securely under the microscope with the variable current source applied to the VCSEL via pin 9 (cathode) and pin 10 (anode) of the TO-header. VCSEL operation can then be verified by inspecting the TO-header under the microscope configured with a camera which is sensitive in the infrared specturm. During this process, it is important to establish and maintain a horizontal alignment axis which contains both the VCSEL aperture and the 1st order photodiode active area region as shown in Figure 29.

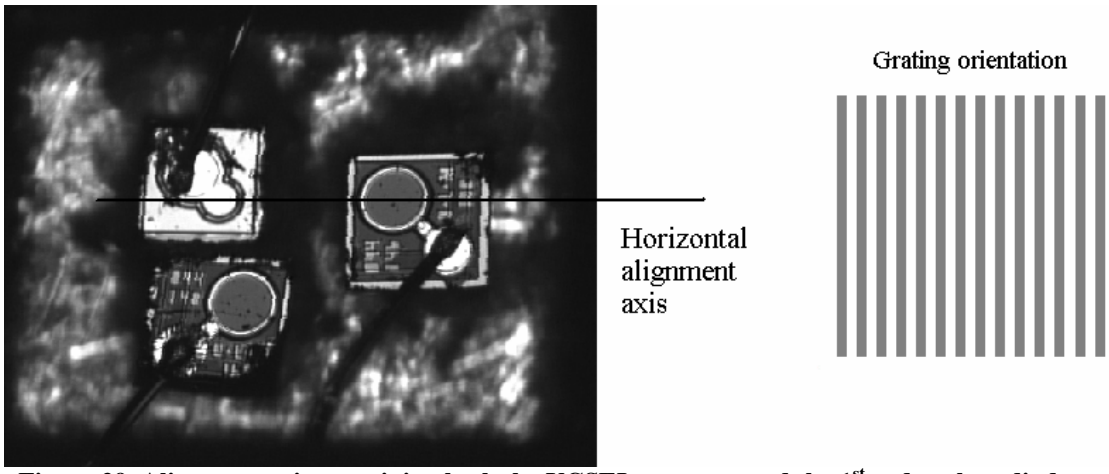

Figure 29. Alignment axis containing both the VCSEL aperture and the 1st order photodiode active area region established perpendicular to the grating fingers.

The microphone chip is then mounted directly on top of the SLA spacer by first applying a very thin, uniform layer of UV-cured epoxy on the surface of the SLA spacer around the circular void. After making certain that the optical grating fingers are aligned perpendicular to the horizontal alignment axis, the microphone chip is placed over the SLA void. Pressure is then carefully applied to the microphone chip so that the epoxy forms an effective seal between the microphone and the SLA surface. Once the microphone is in place, fine adjustments to the alignment are made so that the VCSEL light strikes the center of the grating regions as shown in Figure 30. Low current supplies to the VCSEL (below threshold current) are recommended during this phase of the alignment process. Once the VCSEL is aligned in the center of the grating, it is sometimes useful to vary the applied current, and thereby the VCSEL intensity, to see if the beam spot illuminates the grating in a uniform manner. Nonuniformity of the beam spot in this procedure is usually a result of tilting and the alignment process should be repeated in this event. After fine adjustments are made to the alignment, the epoxy layer between the microphone and the SLA spacer is cured. This same alignment process is used for the biomimetic directional microphone and a high-power microscope image showing the proper orientation of the microphone is provided in Figure 31.

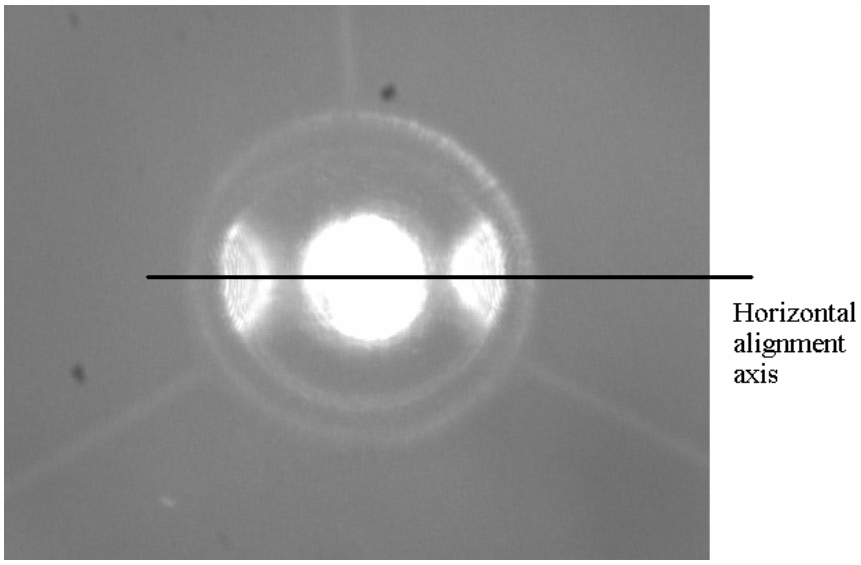

Figure 30. Fine adjustments made to omnidirectional optical microphone using magnified infrared sensitive viewing tool before curing

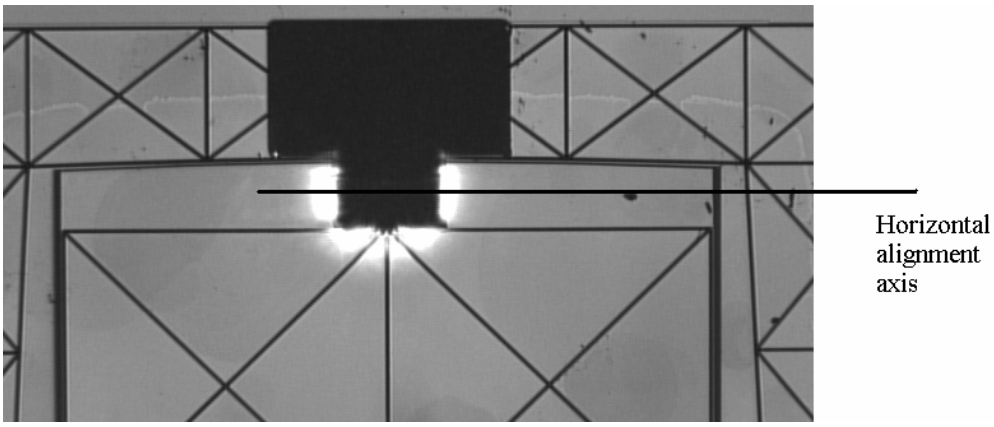

Figure 31. Fine adjustments made to biomimetic optical microphone using magnified infrared sensitive viewing tool before curing

Step 3: Electrostatic Connections and Microphone Header Orientation.

Electrostatic connections are made from the microphone chip to the TO-header pins. This is the final step in fabricating the microphone header assembly and usually requires an element of finesse. Wirebonding directly from the microphone chip to the TO-header is possible, although it is sometimes more convenient to use the intermediary pads provided on the PCB (see Figure 28). Another note regarding wirebonding is that

ground connections may be made anywhere on the gold surface of the microphone-header since this surface is shorted to common ground at pin 9. According to the numbering scheme established by Figure 28 and Table 2, electrostatic connections should always be made to either pin 8 or pin 12.

Preamplifier Tube and Integrated Electronics

The IO-MAP preamplifier tube performs amplification, buffering, and in some instances, noise cancellation of the photocurrent signals. It is critical that the presence of the preamplifier tube does not excessively interfere with the measured sound field and therefore aluminum tubing is used which gives the IO-MAP a form factor comperable to, and slightly larger than, that of a ½ inch measurement microphone. The simple TIA circuit, shown in Figure 32, is contained in the preamplifier tube and is responsible for the amplification of the photocurrent, i_{pc}. In this process, i_{pc} is converted into the output voltage signal, v_{out}, and scaled by the feedback resistance, R_{fb}. Based on the optical simulations for predicted photocurrent levels which fall in the μA range, a value of 200kΩ was selected for R_{fb} to obtain output voltages reasonable for audio applications. Noting that the parallel combination of R_{fb} and the feedback capacitance, C_{fb}, form an RC low-pass filter, the upper cutoff frequency for this circuit is calculated as $f_c=1/2\pi R_{fb}C_{fb}$. For the IO-MAP circuitry, C_{fb} was chosen to be 5pF so that f_c is calculated as 64kHz, which is high enough for pulsed VCSEL operation across the audio bandwidth.

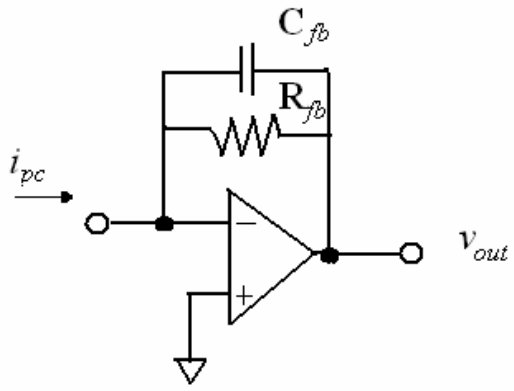

Figure 32. Simple TIA circuit

Within the general IO-MAP preamplifier tube, four of these simple circuits are packaged using a 4-channel low-noise operational amplifier so that multiple i_{pc} signals can be accessed independently. Although it is not shown in Figure 32, a substantial capacitive load at the output of the TIA, which can cause amplifier oscillation, is added by the presence of the long cable. Capacitive loading of the cable was handled by adding a buffer amplifier after the simple TIA circuit.

In order to reach shot noise limitations of the optical detection method, noise cancellation circuitry is required to subtract out the correlated noise components, most notably the RIN component. In some cases where thermal noise levels rise above RIN levels of the VCSEL source, this additional circuitry is unnecessary. However, this cancellation circuitry enables some optical microphone designs to improve their noise performance considerably. A preferable method of implementing differential order detection involves the subtraction of intermodulated photocurrents prior to the TIA stage. The basic circuit consists of a bipolar junction transistor (BJT) differential pair which splits a reference photocurrent by subtraction and provides negative feedback to balance

the sampled signal. This circuit, illustrated in Figure 33, has been shown to provide ultrasensitive performance for laser absorption spectroscopy, coherent LIDAR, and other optical measurements. The following discussion pertains to the implementation of this circuit for use in optical microphones.

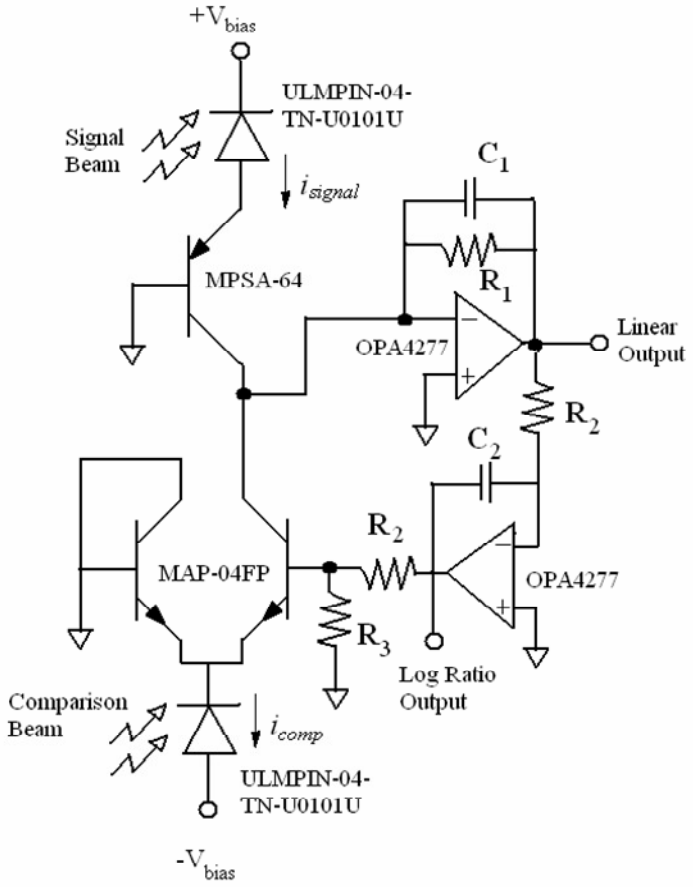

Figure 33. Differential order detection circuitry for shot noise limited optical measurements

One requirement of the circuit shown in Figure 33 is that the captured DC value of the comparison light beam be higher than that of the signal beam, $i_{comp} > i_{signal}$, according to the Ebers-Moll model. As can be seen in the optical modeling results in Figure 21, however, the suggested micro-optical designs yields essentially the same DC offset for the captured portions of I_{+1} and I_0. Modifications to the optical design are

therefore necessary to designate i_{comp} and i_{signal} so that the conditions of this circuitry are met. Apart from this requirement, the differential detection circuitry is dependable for shot noise limited detection well beyond the audio frequency range. A lower cutoff frequency for the circuit is defined by the equation

$$f_{c\_low} = \frac{R_1 R_3 i_{signal}(i_{comp} - i_{signal})}{2\pi R_2 C_2 V_T i_{comp}(R_2 - R_3)} \tag{19}$$

where V_T is the thermal voltage from semiconductor physics

$$V_T = \frac{k_t T}{q}. \tag{20}$$

The presence of the feedback capacitance C_1 serves two purposes. First, as in the case of a simple TIA, C_1 sets the upper cutoff frequency according to the response of the *RC* circuit. Secondly, C_1 is responsible for capacitive stabilization which prevents oscillation of the circuit. The minimum value for C_1 which will prevent oscillation without sacrificing bandwidth is dependent upon the properties of both the photodiodes and the amplifier and is given by

$$C_{1\_\min} = \frac{1}{4\pi R_1 G_{bw}(1 + \sqrt{1 + 8\pi R_1 C_{pd} G_{bw}})} \tag{21}$$

where C_{pd} is the shunt capacitance of the photodiode and G_{bw} is the gain bandwidth product of the amplifier. The value of C_{1_min} is usually quite small and, for the employed optoelectronic components, is much less than the selected value for C_1 of 5pF. Part numbers for the relevant integrated circuit and optoelectronic components are given in Figure 33 while other pertinent values are listed in Table 3. From these values, the upper and lower cutoff frequencies of the differential detection circuitry designed for IO-MAP

implementation are calculated as f_{c_high}=64kHz and f_{c_low}=49Hz respectively assuming reasonable signal and comparison photocurrent levels [33].

Table 3: Differential order detection circuitry parameter values

R_1	500kΩ
C_1	5pF
R_2	1kΩ
C_2	2μF
R_3	26Ω

CHAPTER 4

ACOUSTICAL MODELING OF THE OPTICAL MICROPHONE PACKAGE

Various models for estimating the acoustical performance of the presented optical microphones are presented in this chapter. One goal of these models is to estimate the noise performance of microphone structures which rely on the miniaturized optical detection scheme implemented on the IO-MAP architecture. Dynamic behavior of both the omnidirectional and the biomimetic directional microphone structures is assumed using lumped element approximations. Packaging considerations are also incorporated into a simple yet accurate equivalent circuit model. These models predict noise performance on par and in some cases superior to high-end commercial measurement microphones. A second goal of the modeling carried out in this chapter is to more thoroughly illustrate the directionality of the biomimetic directional microphone and to provide a rough model for comparison. This goal is accomplished using ANSYS finite element modeling software to simulate the harmonic response of the directional microphone as a function of the incidence angle of the measured pressure field. The degree to which these models predict the actual performance of the optical microphones is expected to depend heavily on the form factor of the IO-MAP packaging upon which acoustic characterization tests are carried out.

Lumped Element Modeling of the Omnidirectional Microphone

The following summary describes the process of simulating the noise performance of the 2mm omnidirectional optical microphone header. First consider the omnidirectional microphone structure along with the proposed packaging architecture as shown in Figure 34. A simplified equivalent circuit model for the omnidirectional

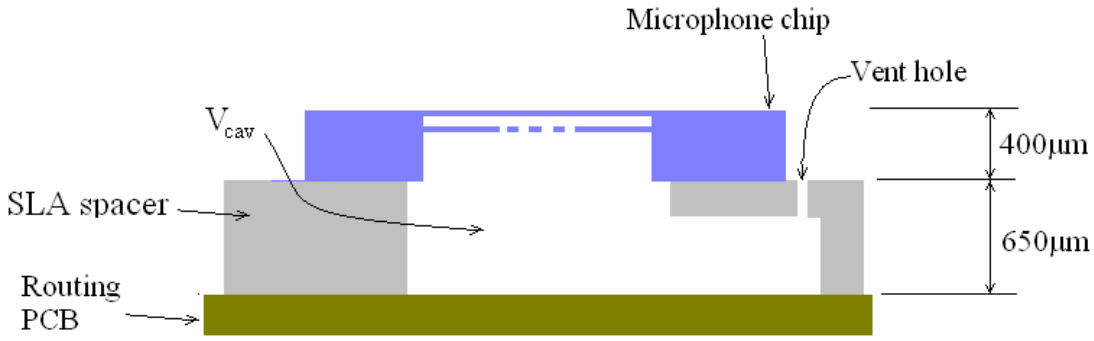

Figure 34. Omnidirectional microphone packaging cross-section

microphone which includes the effects of the microphone header packaging is shown in Figure 35. The impedance of the membrane is modeled by an inductive mass element, m_{eff}, and compliance element, C_{mem}. Other elements included in this model include backplate resistance, R_{back}, packplate compliance, C_{back}, cavity compliance, C_{cav}, and vent hole resistance, R_{vent} [34]. Determination of these parameters begins by estimating the

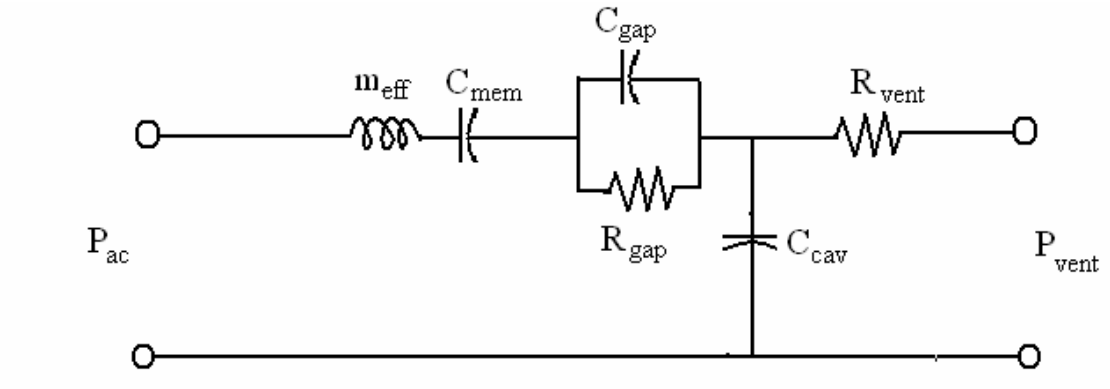

Figure 35. Equivalent circuit model of the omnidirectional optical microphone

resonant frequency of the clamped circular diaphragm. One possibility is to use modal analysis in an appropriate ANSYS model although it is more convenient to use the electrostatic frequency response of the diaphragm. This value is found to be f_o=11kHz from electrostatic characterization results. With knowledge of f_o a value for C_{mem} can then be calculated if the effective mass of the diaphragm is known. A value for m_{eff} is next obtained using Rayleigh-Ritz methods. In this approach, an appropriate trial function is selected which satisfies the boundary conditions of a clamped circular diaphragm for a particular mode (in this case the 1st resonant mode). A cross sectional profile of such a plate with a normalized center deflection, *dg,* and radius, *R,* is shown in Figure 36. An appropriate time-dependent trial function for the first resonant mode of the

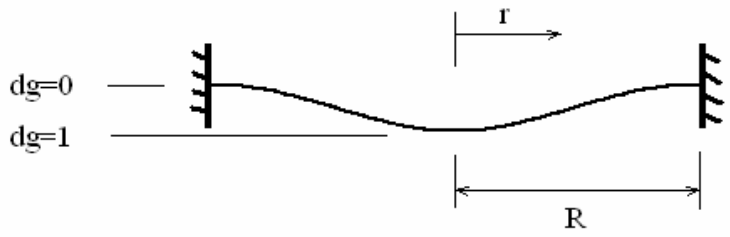

Figure 36. Deflection profile of a clamped circular plate with radius R

diaphragm is therefore

$$dg = \frac{1+\cos\left(\frac{r\pi}{R}\right)}{2}\cos(\omega t) \qquad 22$$

The kinetic energy is obtained integrating the over the entire diaphragm area

$$KE = \int_0^R \frac{1}{2}\frac{m}{\pi R^2} 2\pi r \times \left[\frac{d(dg)}{dt}\right]^2 dr \qquad 23$$

assuming the mass per unit area can be expressed as $m/(\pi R^2)$. An alternate way of expressing the kinetic energy of the diaphragm is to assume that an effective mass, m_{eff}, is concentrated at r=0. This expression becomes

$$KE = \frac{1}{2} m_{eff} (-\omega \cos(\omega t))^2 \qquad 24$$

where ω is the angular frequency and t is time. By setting Equations 23 and 24 equal, an expression for m_{eff} in terms of the total mass, m, is obtained.

$$m_{eff} = \left(\frac{-32 + 6\pi^2}{16\pi^2} \right) m \approx \frac{m}{6} \qquad 25$$

Using m_{eff} in dynamic modeling and ignoring membrane curvature leads to the necessity of another approximation which can be obtained using similar derivations. Because membrane curvature is ignored, the pressure acting on the diaphragm is effectively distributed over only 1/4th of the diaphragm area and can be thought of as an area correction factor. Having values for both f_o and m_{eff}, the diaphragm stiffness and subsequently C_{mem} are easily calculated.

Before deriving expressions for the other parameters of the equivalent circuit, two important simplifications are made which greatly reduce the computational complexity of the model while still preserving a high level of accuracy within the audio bandwidth. First, because the omnidirectional optical microphone backplate, consisting of the three rigid support arms and the suspended diffraction grating, is almost entirely open to the flow of air behind the diaphragm, its primary contribution is in the form of the linearized resistance, R_{gap}, and the backplate compliance is ignored. This simplification eliminates the necessity of a full squeeze film damping analysis using the modal projection method

in ANSYS. Secondly, the diameter of the vent hole, which plays a part in determining the lower cutoff frequency of the microphone, is made sufficiently small so that the system operates as a short circuit to frequencies in the audible range. Although a value for R_{vent} will be calculated later when optimizing the lower cutoff frequency, its impact will be ignored temporarily for the purpose of simplifying the optimization of mechanical compliance for the microphone. These simplifications reduce the equivalent circuit to that shown in Figure 37. Also illustrated in Figure 37 is the corresponding lumped mechanical model. The two remaining parameters to be determined in this system are

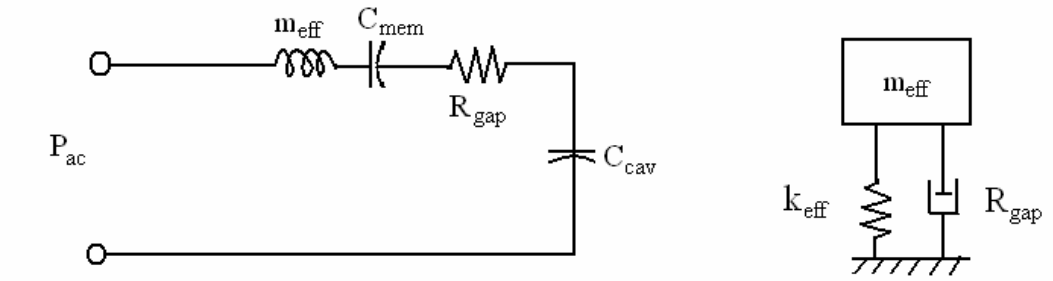

Figure 37. Simplified equivalent circuit diagram ignoring low frequency operation with corresponding lumped mechanical model

therefore R_{gap} and C_{cav}. Although it is possible to perform squeeze film analysis in ANSYS in order to specify R_{gap}, it is more convenient to determine this value via electrostatic characterization results reported in the next chapter. Finally, a value for C_{cav} is selected through a design process which is aimed at maximizing *Sm*. Microphone diaphragms with an enclosed backside cavity are susceptible to a reduction in mechanical sensitivity caused by additional stiffness of the entrapped air as it is compressed. The compliance of such an air cavity with volume V_{cav} is calculated as

$$C_{cav} = \frac{V_{cav}}{Ac^2\rho} \qquad 26$$

where A is the area of the diaphragm, c is the speed of sound in air, and ρ is the density of air [34]. For example, if the 2mm diameter microphone is sealed by mounting the microphone chip directly onto a transparent glass substrate, thus creating a backside cavity volume ($V=1.3x10^{-3}$ mm^3), the total compliance is calculated by the series addition of C_{mem} and C_{cav}.

$$C_{tot} = \frac{A}{k_{eff}} = \frac{1}{\frac{1}{C_{mem}} + \frac{1}{C_{cav}}} \tag{27}$$

The corresponding reduction in mechanical sensitivity leads to an 11dB reduction in the overall sensitivity. Therefore, in order to minimize this loss, an extra back volume cavity is added by designing a hollowed region within the SLA spacer.

The process of optimization requires that the dominant noise source in the system be greater than or equal to the displacement resolution of the optical detection method. In small mechanical structures such as MEMS, the limiting noise source is usually due to thermal mechanical noise. For optical microphones, there are also RIN and shot noise sources to consider as discussed in the conclusion of Chapter 2. For now, however, it will be presumed that these equivalent levels fall below, or can be reduced below the thermal mechanical displacement noise levels of the diaphragm. The displacement noise spectral density of the omnidirectional microphone diaphragm, δ_{th}, caused by a fluctuating spectral density force, F_{th}, is calculated as follows. First, F_{th} is a result of Brownian particle motion and is determined by the equation

$$F_{th} = \sqrt{4k_b T R_{gap}} \tag{28}$$

where k_b is the Boltzmann constant and T is the ambient temperature expressed in Kelvin [6, 34]. The lumped model approximation then allows δ_{th} to be calculated as

$$\delta_{th} = \frac{4F_{th}}{k_{eff}} \tag{29}$$

where k_{eff} is defined in Figure 37 and the factor of four for a circular clamped diaphragm comes about by treating F_{th} as a concentrated load. For optimal noise performance, it is desirable that δ_{th} be greater than or equal to the minimum displacement resolution of the optical detection scheme. Given shot noise limitations of actual optical curve measurements, an estimated minimal displacement value of 40fm/√Hz is possible and this value is used in order to design an SLA back cavity volume which is large enough to allow a predicted thermal mechanical displacement noise level of δ_{th}= 41fm/√Hz using Equations 26-29.

Once an appropriate back volume is selected, a vent hole is designed to avoid sensitivity to ambient pressure fluctuations. Because it attenuates sensitivity however, this vent hole can also degrade noise performance if it is not designed properly. Design of the vent hole begins by referring back to the equivalent circuit of Figure 35 and noting that the combination of C_{cav} and R_{vent} forms a simple high-pass RC circuit. The lower cutoff frequency of this circuit is calculated as $f_{vent}=1/(2\pi R_{vent}C_{cav})$. A value for C_{cav} is determined by applying Equation 26 for the SLA back cavity volume of approximately $V_{cav}\approx 16\text{mm}^3$. R_{vent} is computed under the assumption that the air in the cavity behaves as an incompressible fluid using the equation

$$R_{vent} = \frac{8\eta l_{vent}}{\pi r_{vent}^{\ 4}} \tag{30}$$

where η is the dynamic viscosity of air, and other terms are defined in Figure 38 [35].

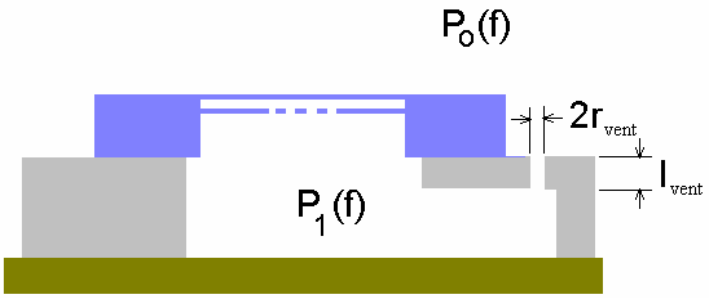

Figure 38. Description of parameters used for vent hole resistance calculation

In this illustration, the vent hole is located on the SLA spacer itself and allows the equalization of pressures $P_1(f)$ and $P_0(f)$ at low frequencies. Ideally, the vent hole can be located on the diaphragm of the microphone so as to exploit the high resolution and precision of silicon micromachining techniques. An etch hole on the order of a few microns, for example, would allow the lower cutoff frequency to be minimized so as not to detract from microphone sensitivity in the audible range. Another benefit of microfabricating these vent holes is that it would allow more precise phase matching among multiple microphones which is especially important in microphone array applications [18, 36]. Regardless, the demonstration of low noise microphones is possible using the somewhat crude method of designing the vent holes in the SLA spacer. The minimum size vent hole which is possible using SLA fabrication is about 70µm in diameter and a micrograph of the vent hole is shown in Figure 39. By substituting other suitable values in Equation 30, R_{vent} is then computed and the estimated cutoff frequency can be plotted against vent hole diameter as shown in Figure 40. From this graph, a value

of 150Hz is taken as the expected cutoff frequency for the omnidirectional microphone on the IO-MAP header package.

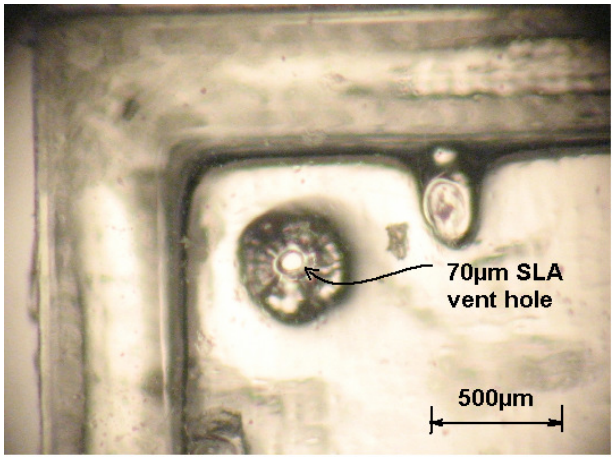

Figure 39. SLA vent hole with approximate 70µm diameter

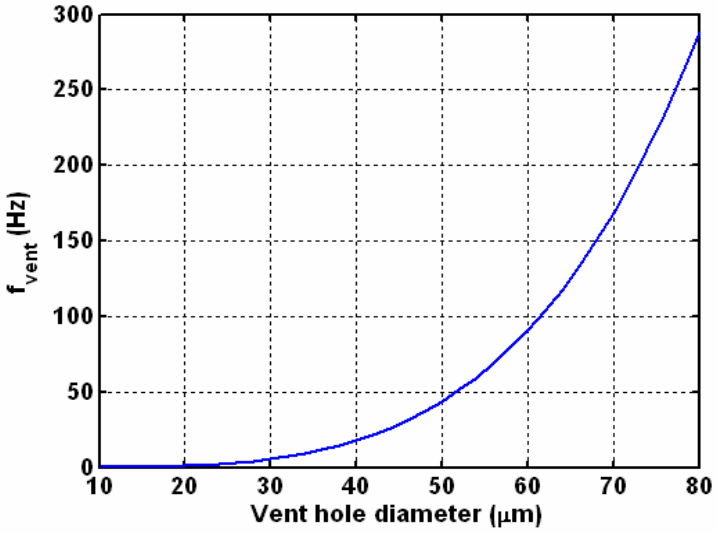

Figure 40. Estimated cutoff frequency as a function of vent hole diameter

With the necessary parameters in place, the equivalent circuit in Figure 35 can be evaluated. In this process, the ratio between the driving pressure ($P_o(f)$-$P_1(f)$) and the vent pressure ($P_o(f)$) is used to describe the low frequency behavior of the diaphragm. This ratio is given by

$$\frac{P_o(f)-P_1(f)}{P_o(f)}=1-\frac{P_1(f)}{P_o(f)}=1-\frac{1}{i\omega\tau+1} \qquad 31$$

where τ is the time constant of the RC filter given by $\tau=R_{vent}xC_{cav}$. For the 2mm omnidirectional diaphragm, the relevant parameters are $\tau=.0013\ 1/s$, $m_{eff}=2.74x10^{-9}$ kg, $R_{gap}=5.7x10^{-5}$ N-s/m, and $k_{eff}=71.4$ N/m. Applying these parameters to the transfer function for a damped second order system under harmonic excitation yields the response shown in Figure 41. Applying F_{th} to this transfer function for the lumped model yields the predicted thermal mechanical displacement noise spectrum shown in Figure 42.

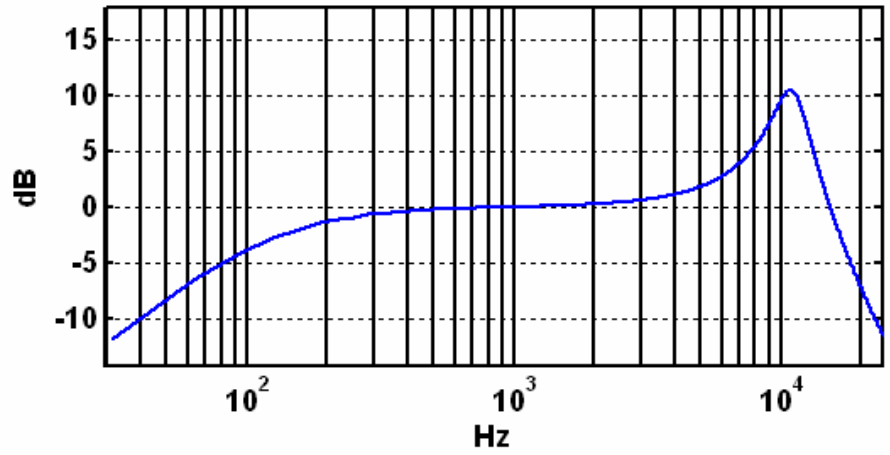

Figure 41. Normalized response of the second order lumped model for the 2mm omnidirectional diaphragm

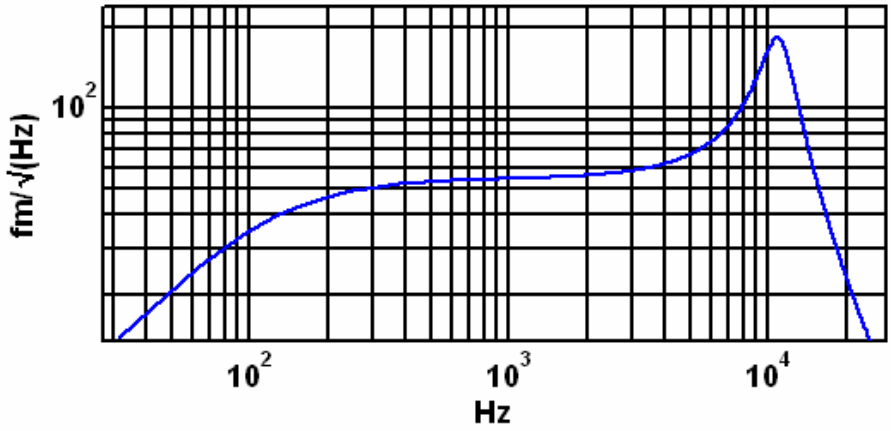

Figure 42. Predicted thermal mechanical noise spectrum of the 2mm omnidirectional microphone

Alternatively, Figure 42 can be expressed in terms of an equivalent constant pressure noise level of 1.24μPa/√Hz. After applying an A-weighted filter to this noise spectrum level, a theoretical noise level of 16.5dBA is obtained assuming the optical microphone is thermal mechanical noise limited.

Modeling of the Biomimetic Directional Microphone

Several models are presented in order to describe the dynamic behavior of the unique biomimetic directional microphone. First, ANSYS10 finite element method (FEM) modeling software is employed to visualize the mode shapes of the diaphragm and to simulate the directionality of the device. A mathematical model, taken from literature, is then provided for estimating the dynamic behavior of the biomimetic directional microphone. This model for angular displacement of the diaphragm, derived from lumped element approximations, is combined with the assumption of small angle deflections for comparison with experimental results.

Finite Element Modeling

A realistic model of the biomimetic directional microphone was constructed using ANSYS10 FEM software package and consists of a 1mm x 2mm silicon diaphragm supported by two pivot arms which provide mechanical coupling between the two sides of the diaphragm. The thin silicon diaphragm is modeled using 8-node SHELL93 elements which provide complete structural analysis capability. A damping ratio obtained from electrostatic characterization tests is applied for a more complete model although stiffening effects of the backside air cavity are ignored.

Modal Analysis

First, a modal analysis is performed to estimate the first two modes of the diaphragm motion. Figure 43 illustrates both the rocking and the flapping modes.

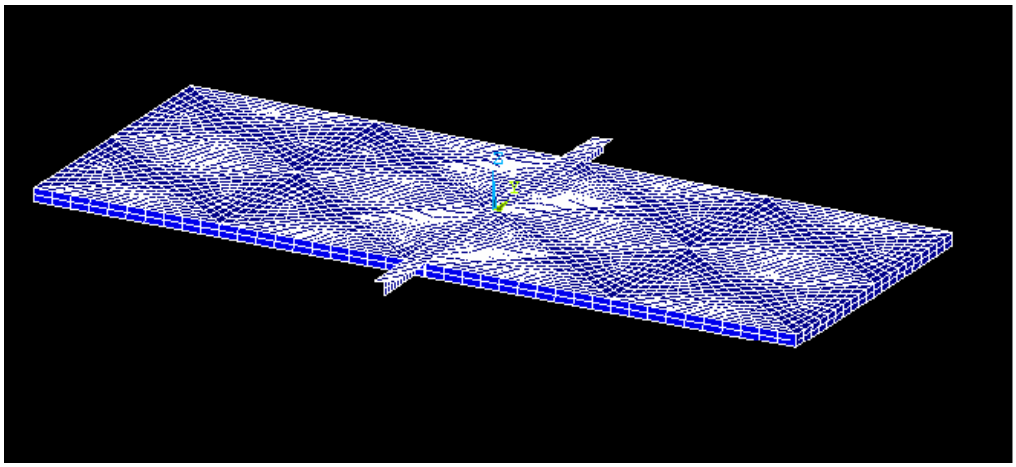

(a) f_1=734 Hz

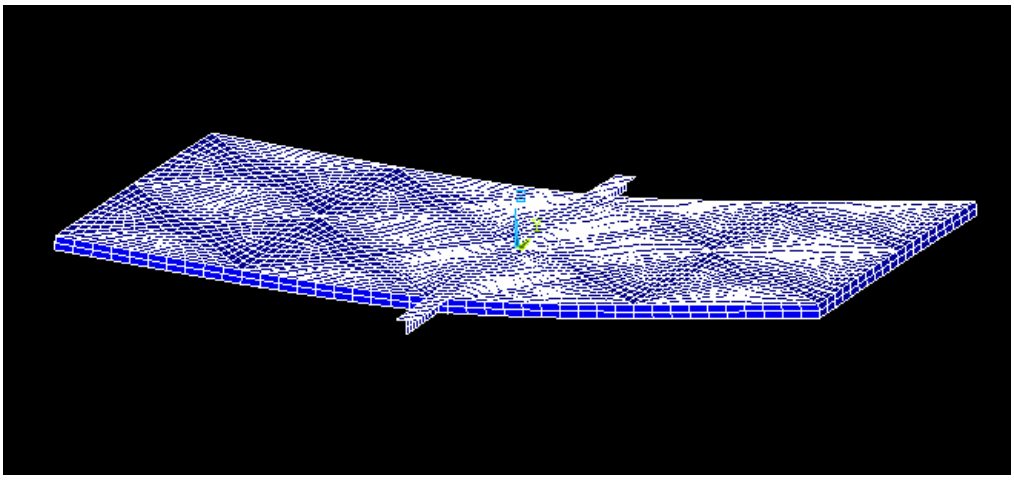

(b) f_2=15,432 Hz

Figure 43. Finite element modal simulation of the first two modes of the biomimetic directional diaphragm

From this analysis, two observations are made. The first observation regards the impact of these resonant modes on the acoustic response. The value of 734Hz for the 1st resonant mode indicates that the biomimetic directional microphone will be sensitive to

frequencies in a highly important bandwidth of the audio range. A related detail is that the 2nd resonant mode is high enough to avoid significant interference with the 1st resonant mode. A second observation pertains to effectiveness of the optical detection method in regards to the locality of the diffraction grating. It is clear from the analysis that the maximum diaphragm displacement occurs at either end of the diaphragm where the grating fingers are located and the optical detection takes place.

Directionality Simulation

The FEM model of the biomimetic directional microphone was also used to simulate the directionality of this microphone structure. This was done using harmonic analysis to solve for the displacement of the diaphragm under the application of two phase-separated forces, f_1, and, f_2, which correspond to the ipsalateral and contralateral forces discussed in literature [14]. A simple derivation was used in order to generate these forces and serves here to better illustrate the simulation. The derivation begins by establishing the coordinate system shown in Figure 44. Assuming an incident plane

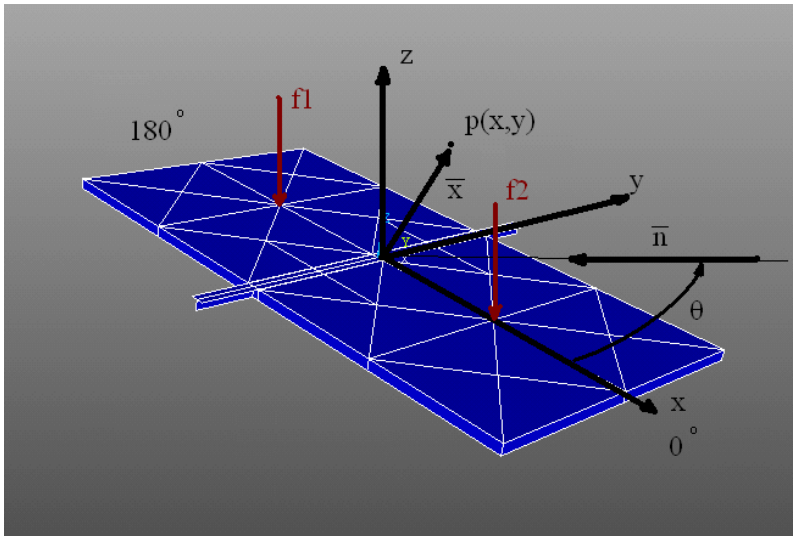

Figure 44. Coordinate system used to describe the directionality simulation of the biomimetic directional microphone

wave, which varies only in the x-y plane, the pressure at an arbitrary location, $\bar{x}$, can be expressed as

$$p(x, y) = Pe^{i\omega(t \pm \frac{\bar{x} \bullet \bar{n}}{c})} \qquad 32$$

where P is the pressure amplitude, ω is the angular frequency, $\bar{n}$ is the direction of propagation, c is the speed of sound, and t is the time used in transient analyses. In the finite element model, it is convenient to consider two pressures acting on either side of the membrane each distributed over an equal area. For the purpose of modeling, it is reasonable to assume that these pressures are distributed evenly about their respective areas and as a result produce two forces, f_1 and f_2, located symmetrically about the y axis (rocking axis) at a distance $\pm L/4$ from the origin where L is the diaphragm length (L=2mm). Consequently, $\bar{x}$ takes the form $\bar{x} = \pm\frac{L}{4}\bar{\mathbf{j}}$. The direction $\bar{n}$ is expressed in terms of Cartesian coordinates as $\bar{n} = -\cos(\theta)\bar{\mathbf{i}} - \sin(\theta)\bar{\mathbf{j}}$ based on the illustrated configuration. The expressions for the two forces then become

$$f_1 = PAe^{i\varpi(t - \frac{L\cos(\theta)}{4c})} \text{ and } f_2 = PAe^{i\varpi(t + \frac{L\cos(\theta)}{4c})}. \qquad 33$$

It is clear from Equation 33 that the two time-varying forces are equal in magnitude but differ by a phase which depends on the incidence angle, θ, of the approaching plane wave. Observing more closely, it can be seen that these two forces share the same phase when θ is equal to an odd multiple of π/2. At these values of θ, f_1 and f_2 are identically equal and should only excite higher order modes in the diaphragm. Maximum disparity

between f_1 and f_2, will occur when $cos(\theta)$ is a maximum (i.e. θ equals any integer multiple of π).

For a given frequency and pressure amplitude, the range of coupled forces f_1 and f_2 is found by allowing θ to vary from 0 to π. These force pairs are then applied to the model and harmonic analysis is performed in order to obtain displacement amplitude as a function of θ. The results from this simulation for a 1.5kHz applied signal at 1Pa are plotted in Figure 45. Clearly, the directional response of the biomimetic microphone is

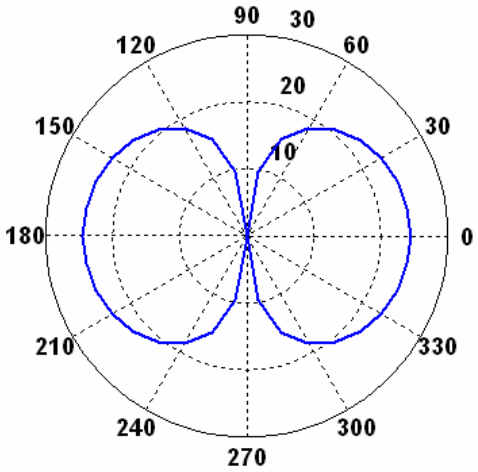

Figure 45. Simulated directionality in ANSYS of the biomimetic directional microphone structure at 1.5kHz (dB: arbitrary ref)

that of a directional gradient microphone. One figure of merit that is often used to quantify the directivity of microphones is known as the directivity index (DI). The DI is found by first computing the "random efficiency" as

$$Q(f) = \frac{2}{\int_0^{\pi} \left(\frac{V_{RMS}(f,\theta)}{V'_{RMS}(f)} \right)^2 \sin(\theta) d\theta} \qquad 34$$

In Equation 34, $V_{RMS}(f,\theta)$ is the RMS microphone output obtained as a function of signal frequency, f, and incidence angle θ. $V'_{RMS}(f)$ on the other hand is the RMS reference signal value obtained by setting $\theta=0$ which corresponds to on-axis response and maximum sensitivity of the directional microphone. The DI is then expressed as

$$DI = 10Log_{10}(Q(f)) \tag{35}$$

As described by Equations 34 and 35**,** the DI is a convenient way of describing the decibel difference between the power levels actually observed by a microphone in a diffuse sound field at random incidence, and the power levels that would be observed if the microphone were uniformly sensitive in all directions. For omnidirectional microphones, V_{RMS} and V'_{RMS} are identically equal for all values of f and θ. Therefore, the integrand in Equation 34 reduces to $\sin(\theta)$ and the DI for a perfectly omnidirectional microphones is 0dB. For an ideal directional gradient microphone, whose response follows a $\cos(\theta)$ relationship, the DI is found to be 4.8dB. From the directivity simulation performed in ANSYS at 1kHz, the DI of the biomimetic directional microphone is calculated as 4.8dB, reinforcing its behavior as a directional gradient microphone.

Mechanical Modeling

A mechanical model for the biomimetic directional microphone has been presented in literature [14]. Assuming a 0° incident sound wave, a transfer function for angular deflection of the diaphragm, Θ, in terms of applied pressure signal amplitude, P, is given by

$$\frac{\Theta}{P} = \frac{\frac{Ai\omega(\frac{L}{2})^2}{cI_{yy}}}{\omega_1^2 - \omega^2 + i2\omega\zeta_1\omega_1} \qquad 36$$

where A is the diaphragm area, I_{yy} is the mass moment of inertia, ω_1 is the resonant frequency of the first mode, and ζ_1 is the damping ratio of the first mode. If Θ is small, the amplitude of the tip displacement in the z direction is approximately equal to $\Theta(L/2)$ according to the small angle approximation. This approximation, along with the measured displacement sensitivity, provides a comparison model for sensitivity measurements. Using this mathematical model, the transfer function relating the first mode of grating motion to the signal pressure is plotted in Figure 46 [16]. Again, as observed from modal analysis, the mechanical sensitivity of this microphone is capable of acquiring acoustic information which is vital in audio applications. While the 6dB per octave roll-off occurring above and below resonance will take away from sensitivity as well as directional performance, these frequencies become less important for speech intelligibility and therefore this microphone is well suited for hearing aid applications.

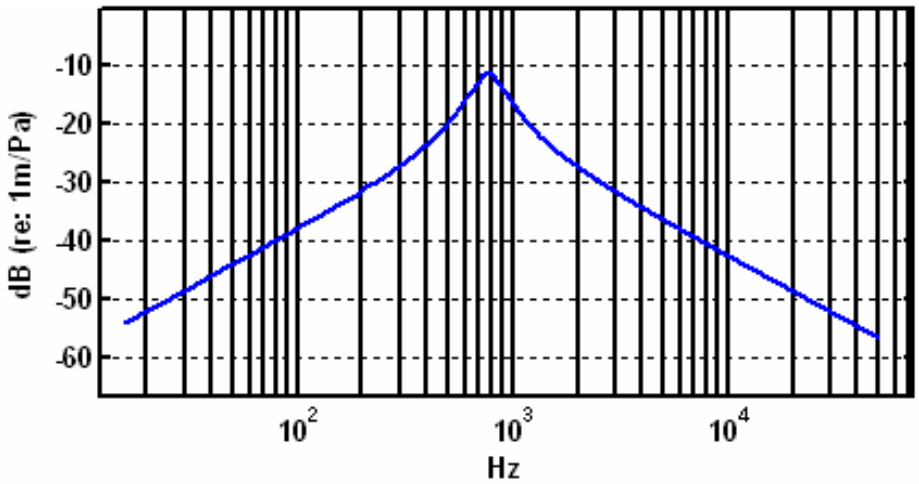

Figure 46. Transfer function for grating deflection assuming small angle deflections for the biomimetic directional microphone structure

CHAPTER 5

CHARACTERIZATION OF FULLY PACKAGED MICRO-OPTICAL MICROPHONES

Fully packaged microphones with integrated micro-optical detection architectures are characterized in this chapter and some comparisons are made between these microphones and other quality condenser microphones. For both omnidirectional and biomimetic directional optical microphones, the optical modulation performance is first reported. These results are then followed by acoustic characterization including frequency response, directionality, and noise measurements. Included in this chapter are the results from the simultaneous "figure 8" measurement of a dual array of biomimetic directional optical microphones. The results in this chapter reflect the excellent performance of not only the optical microphone header itself, but also the IO-MAP preamplifier package which imposes minimal disturbance to the measured sound field. A majority of the characterization presented in this chapter makes use of the Georgia Tech Integrated Acoustic Laboratory anechoic chamber facility which provides an acoustically isolated testing environment. Prior to these acoustic characterization tests, the noise level of the anechoic chamber was measured to be sufficiently low to accurately characterize the presented optical microphones. A model 824 Larson Davis sound level meter was used to measure the 16dBA anechoic chamber noise floor.

Performance of the Omnidirectional Optical Microphone

The performance of the 2mm diameter omnidirectional optical microphone is first characterized using the miniaturized packaging scheme. This microphone descends from a previous MEMS design which was intended for broadband acoustic measurements but was dominated by large thermal mechanical noise levels. Unlike its predecessor, the present omnidirectional optical microphone is equipped with an optimized 200μm diameter optical grating which not only maximizes the performance of the optical detection method, but also minimizes the backplate resistance – thereby minimizing the thermal mechanical noise. These factors enable the present omnidirectional optical microphone to exhibit performance superior to miniaturized condenser microphones and on-par with commercialized measurement microphones. Finally, directionality measurements are provided to assess the influence of the IO-MAP packaging architecture on the measured sound field.

Modulation Performance of Sub-1mm^3 Optical Detection

The optical modulation of the micro-optical system contained within microphone header is a crucial attribute directly impacting the performance of the optical microphone. In order to assess the performance of the optical detection scheme, the 2mm diaphragm is actuated using electrostatic DC bias. The output voltage obtained from a single diffracted order is collected and plotted as a function of the applied DC bias. Figure 47 shows the results obtained from the I_{+1} intensity order. The sensitivity is then calibrated by adjusting the diaphragm position using electrostatic DC bias. At an optimal value of 22V, the resulting displacement sensitivity for this microphone is calculated using

Equation 9 as 10.5mV/nm. This result comes to within 15% of the optical model predictions when the 51% transmission loss through the unmetallized polysilicon diaphragm is taken into account. This error is most likely due to slight misorientation of the optoelectronic components and/or an improper assumed value of the refractive index of the polysilicon diaphragm in the transmission model from Chapter 2.

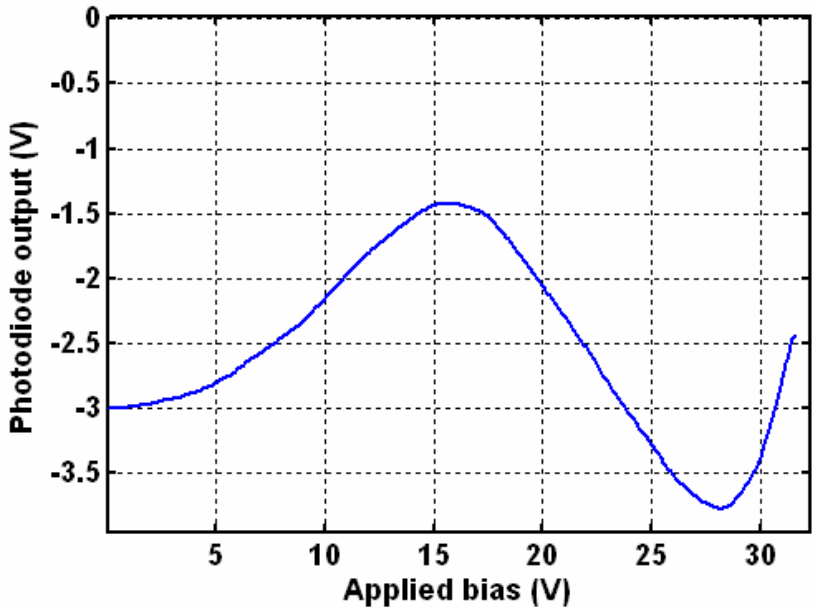

Figure 47. Optical curve for the 2mm omnidirectional microphone measured using the IO-MAP

Displacement resolution is another important figure of merit which takes into account the diaphragm displacement levels at which the microphone is unable to differentiate between acoustic signals and the internal noise of the device. The displacement resolution is defined by the measured noise spectrum of the microphone divided by the displacement sensitivity and can be expressed in units of m/√Hz at a specified frequency. The noise floor of the omnidirectional optical microphone is measured using a Stanford Research Systems (SRS) SR785 dynamic signal analyzer and at 1kHz, a value of -116dBV_{rms}/√Hz is obtained. The displacement resolution for the

omnidirectional microphone with a single 1st order output is therefore roughly 150fm/√Hz at 1kHz. Following the dynamic range calculation which was described in Chapter 2, this microphone demonstrates a dynamic range of 123dB.

Electrostatic and Acoustic Response Characterization

Frequency response measurements are carried out in order to asses the operational range of these devices and to ensure that the IO-MAP testing apparatus is able to minimize acoustic disturbances. An extremely attractive feature of the optical detection method is the capability of self dynamic characterization using electrostatic actuation. Electrostatic frequency response measurements, which were used to obtain dynamic parameter information such as damping coefficients in the modeling section of this thesis, are presented alongside acoustic measurements for procedural demonstration and comparison purposes. The electrostatic and acoustic frequency response results for the 2mm omnidirectional microphone measured using the IO-MAP apparatus are shown in Figure 48 and Figure 49 respectively. In Figure 48, the electrostatic response has a flat response down to DC because the vent hole acts as a short circuit in this case.

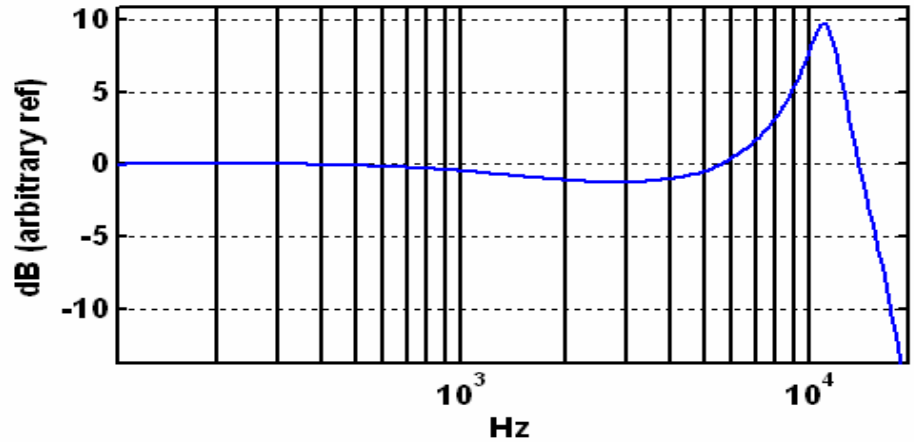

Figure 48. Electrostatic frequency response of the 2mm omnidirectional microphone obtained using swept sine excitation and micro-optical detection

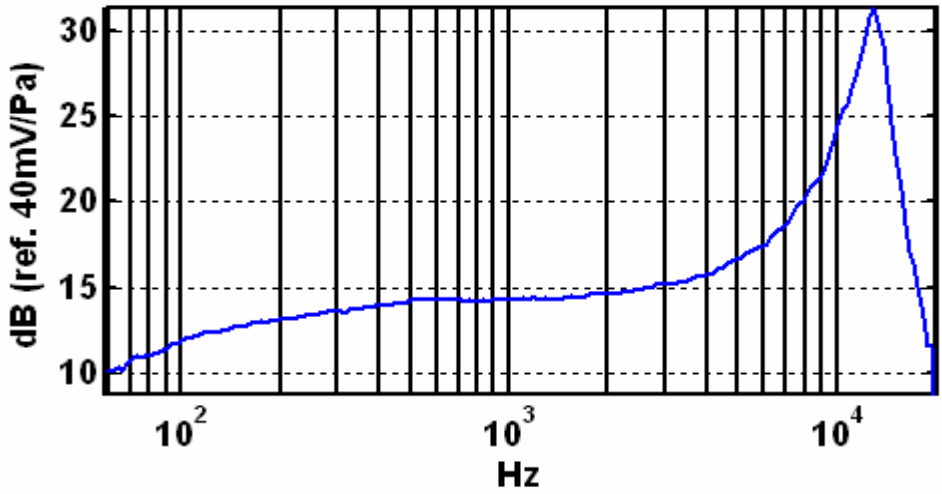

Figure 49. Acoustic frequency response of the 2mm omnidirectional microphone obtained using swept sine excitation and micro-optical detection

The free-field acoustic frequency response is normalized to the Larson Davis 2541 calibration microphone whose sensitivity of 40mV/Pa is taken to be constant across the audio bandwidth. The acoustic response shows a lower cutoff frequency which agrees very well with predicted value of 150Hz obtained from Figure 40 for a 70μm vent hole diameter. With respect to the electrostatic response which was obtained without applying a bias voltage, a 5dB increase is observed in the resonant peak of the acoustic response and is due to electrostatic stiffening during the sensitivity calibration process.

Noise Performance

A final yet tremendously significant characteristic of the optical microphones presented in this thesis is their noise performance. The omnidirectional optical microphone exhibits a noise spectrum with RIN limitations up to the device resonance where the thermal mechanical displacement noise peak is visible. The measured voltage noise spectrum of this device is shown in Figure 50. In order to obtain the pressure noise

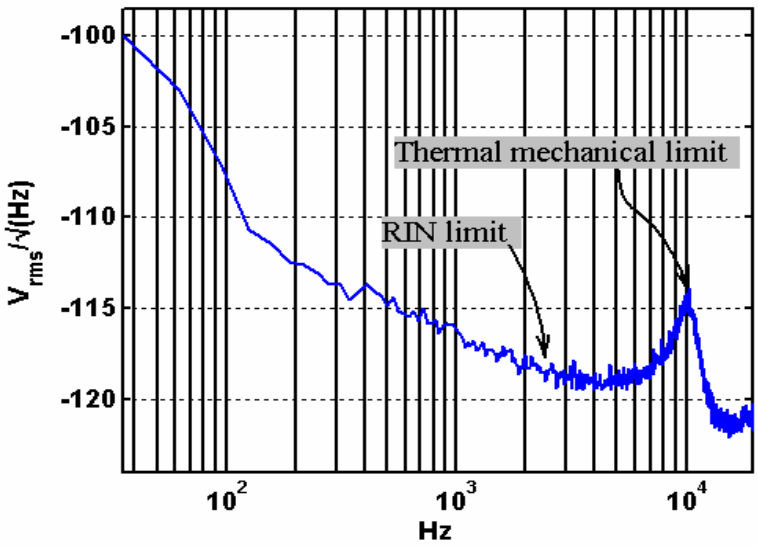

Figure 50. Measured noise spectrum of the omnidirectional optical microphone

spectrum, a calibration process is performed based the known pressure response of a Larson Davis 2541 calibration microphone. The calibration process is performed in a MatLab m-file file which converts the noise data obtained using the SR785 dynamic signal analyzer from units of $dBV_{rms}/\sqrt{Hz}$ to $Pa/\sqrt{Hz}$ using a calibration constant of 40mV/Pa at 250Hz. During this process accurate sensitivity levels are calculated by dividing the voltage output of the optical microphones by the known pressure response of the calibration microphone. Once the pressure noise spectrum is obtained, the m-file then applies an A-weighting filter in order to obtain the dBA noise value. This process was used in order to measure the noise floor of the anechoic chamber and agrees well with the results obtained from the Larson Davis model 824 sound level meter. This measurement was repeated several times and confirms that the anechoic chamber facility is quiet enough to perform accurate noise measurements of the optical microphones given their theoretically predicted values. A comparison of pressure noise levels which confirms this assertion is shown in Figure 51. The dip in pressure noise which occurs at about 12kHz

is a result of resonant frequency mismatch between the sensitivity measurements and noise measurements due to variations in optimal bias voltage. The Larson Davis 2541 microphone has a 15dBA noise floor and its measured spectrum is included to show the minimum level to which noise can accurately be measured [37]. Using a Larson Davis model 824 sound level meter, the noise spectrum obtained with the calibration microphone is found to produce a 16dBA noise level, and therefore the measurement is chamber noise limited.

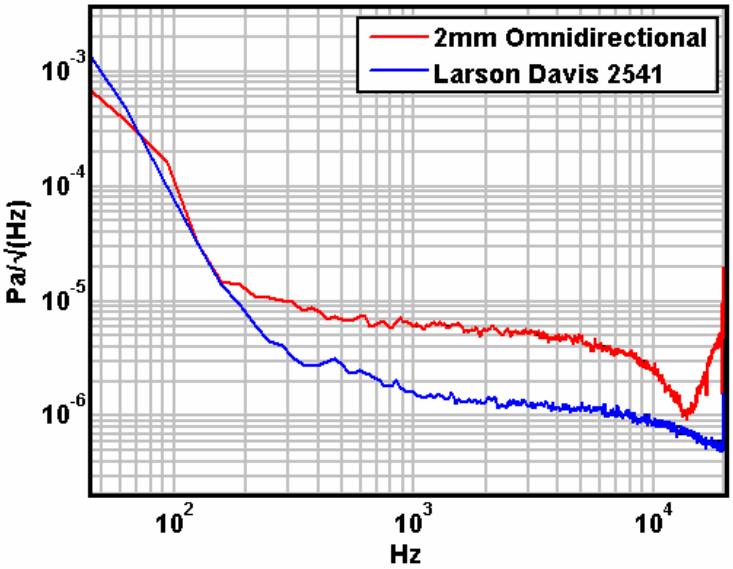

Figure 51. Comparison of measured pressure noise spectrums

The measured noise floor of the fully packaged 2mm omnidirectional microphone is 26dBA. In order to verify agreement between predicted noise levels and experimental results, a comparison is made in terms of equivalent diaphragm displacement noise. This requires knowledge of displacement sensitivity, which was calculated from Figure 47, along with other model parameter values already derived. Excellent agreement between predicted and experimental values is seen in Figure 52. The slight mismatch in resonant frequency between the thermal noise model and the

measured thermal noise peak is likely due to the effect of electrostatic stiffening which is not taken into account by the model. Also shown in this displacement noise comparison is the equivalent shot noise level calculated based on knowledge of the measured optical curve. The shot-noise level is included in the presented noise plots since it represents the absolute limit of the micro-optical detection method when differential order detection is used. In this case, the optimal 22V bias point for the 2mm omnidirectional microphone corresponds to a 2.7V DC offset at the photodiode output. Recalling from Equation 18, the DC offset along with the feedback resistance of the TIA – 200kΩ in this case – determine the shot noise level. For these values of V_{DC} and R_{fb} the voltage shot noise, v_{shot}, is found to be 312nV/√Hz (or 30fm/√Hz) which is constant across the spectrum.

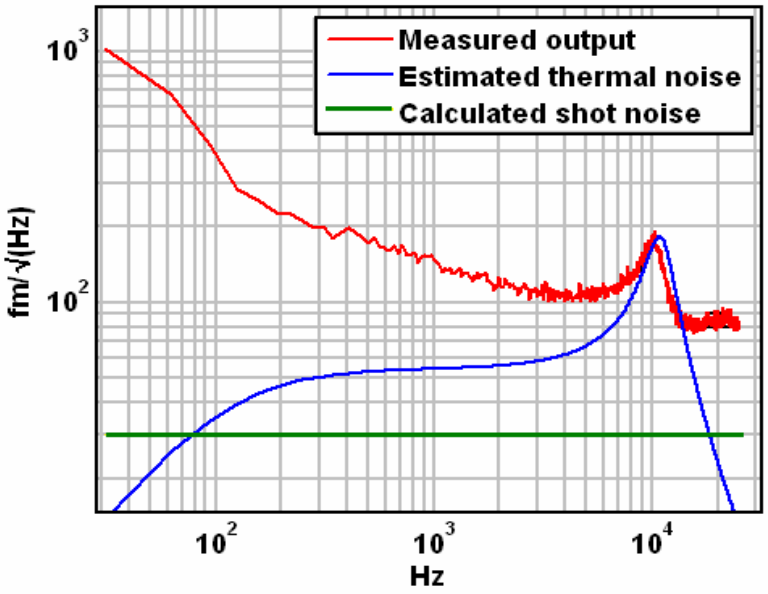

Figure 52. Comparison of measured noise to other relevant noise levels in terms of equivalent diaphragm displacement

Demonstration of RIN Cancellation

The already compelling argument for the potential of optical detection in small scale microphones is made even stronger when considering the possibility of noise

cancellation by means of differential order detection in cases such as the 2mm omnidirectional microphone where single order output detection is dominated by the additive RIN component. In order to demonstrate the principle of differential order detection for RIN cancellation using the micro-optoelectronic components of the IO-MAP, a simple differential multiplier circuit, with all of the associated drawbacks mentioned in the conclusion of Chapter 3 was constructed and tested. Unlike the more powerful cancellation circuitry shown in Figure 33 which operates in the current domain, the noise cancellation in this circuit is performed after the TIA stage. Due to finicky requirements imposed by this circuitry on DC output levels, results are limited to noise measurements at locations on the optical curve where the sensitivity is not optimized.

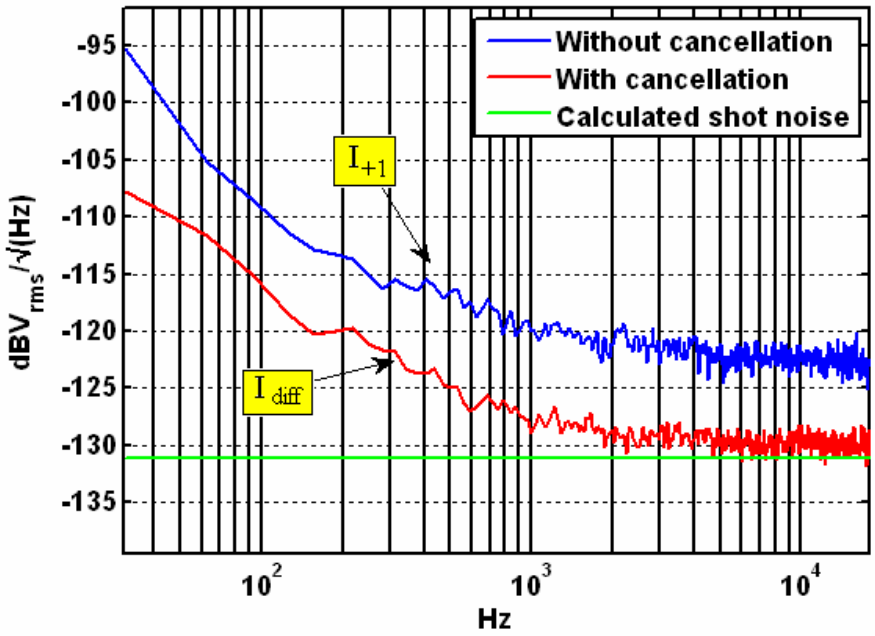

Figure 53. Noise cancellation using differential detection in the voltage domain

Results using this circuitry and demonstrating RIN cancellation down to shot noise are shown in Figure 53. In this figure, the spectrum labeled I_{+1} represents a single 1st order output signal which is dominated by RIN noise. The second curve labeled I_{diff} represents

the combination of I_{+1} and I_0 at the output of the differential detection circuitry. Despite the limitations of this circuitry, a cancellation of 10dB across the relevant spectrum was observed. This noise reduction should therefore enable a 10dBA improvement in the noise performance of the 2mm omnidirectional optical microphone meaning that the 16.5dBA limit of this microphone structure is attainable.

Directionality Results and Assessment of Sound Field Disturbance

In order to further validate the IO-MAP as an effective tool for accurate characterization, directionality measurement results for the 2mm omnidirectional optical microphone are presented and are later compared to the uniform response of the Larson Davis 2541 ½ inch measurement microphone. These test tests are performed in the anechoic chamber where a rotation stage is positioned 1m from a loudspeaker (see Figure 54). The IO-MAP tube is then mounted to the rotation stage and a controller sets the angular orientation of the microphone with respect to the speaker.

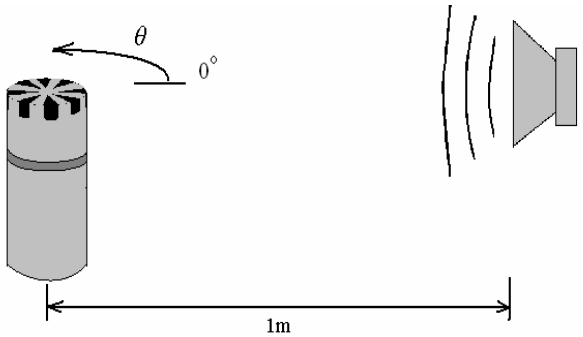

Figure 54. Experimental setup for directionality measurements made in the anechoic chamber

The measured response of the omnidirectional microphone is shown in Figure 55 for 1kHz, 2.5kHz, 5kHz, and 10kHz pure-tone pressure waves. At lower frequencies, the results are perfectly omnidirectional. At higher frequencies, however, artifacts do begin

to appear in the directionality measurements but are believed to be a product of the rotation stage and associated mounting gear rather than the IO-MAP packaging itself.

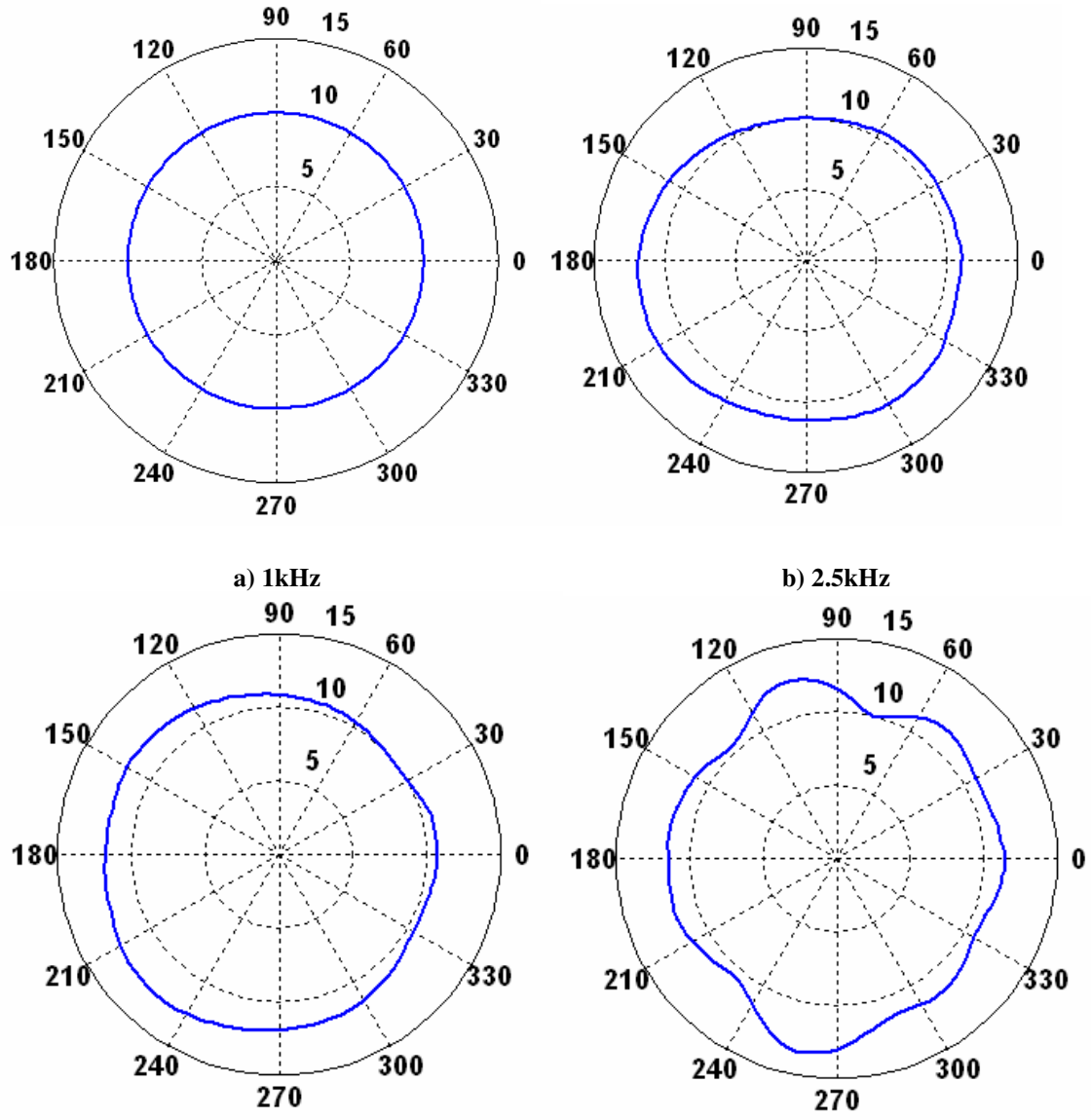

a) 1kHz b) 2.5kHz

c) 5kHz d) 10kHz

Figure 55. Measured directionality of the omnidirectional microphone at a) 1kHz, b) 2.5kHz, c) 5kHz, and d) 10kHz (dB: arbitrary ref).

This hypothesis is tested by repeating the same series of measurements for the Larson Davis model 2541 ½ inch microphone which has excellent omnidirectional response characteristics. These results are presented in Figure 56, and as expected, there are striking similarities between this data set and that of the omnidirectional optical microphone package leading to the conclusion that irregularities in the measured response are a result of the presence of the rotation stage and associated mounting gear.

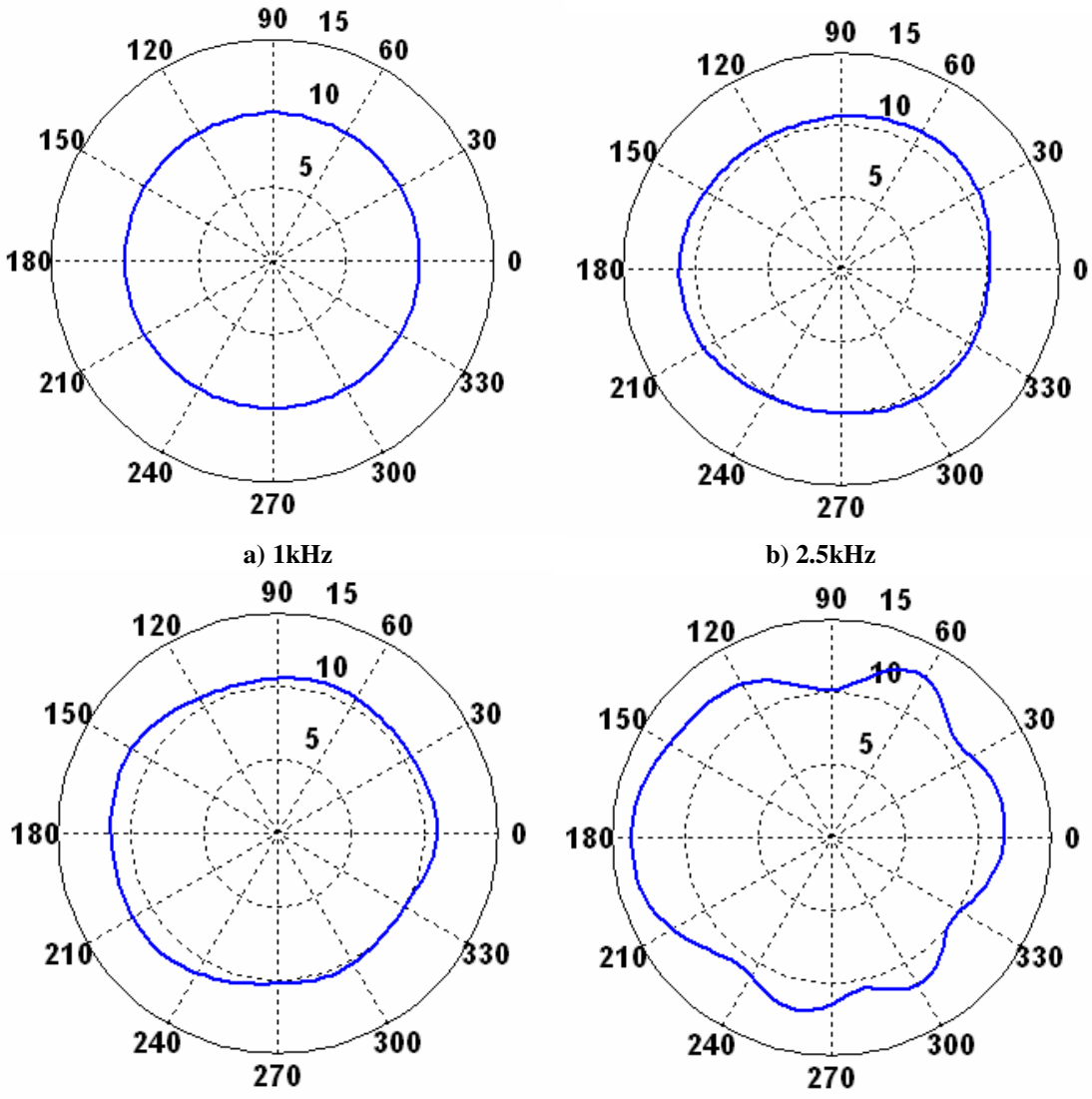

a) 1kHz b) 2.5kHz

c) 5kHz d) 10kHz

Figure 56. Measured directionality of the Larson Davis 2541 ½ inch measurement microphone at a) 1kHz, b) 2.5kHz, c) 5kHz, and d) 10kHz (dB: arbitrary ref).

A second set of directivity measurements is intended to analyze the effects of the preamplifier tube packaging about an axis of rotation which is described by Figure 57

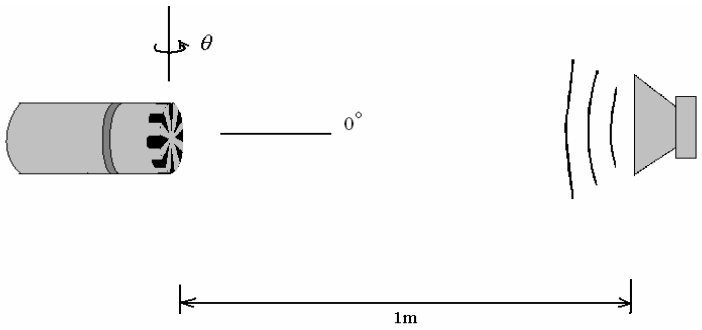

Figure 57. Secondary experimental setup for directionality measurements made in the anechoic chamber

The results obtained for the 2mm omnidirectional microphone are plotted in Figure 58 and can be compared with the results for the Larson Davis 2541 ½ inch measurement microphone plotted in Figure 59. The shapes of these plots are nearly identical and remain more or less omnidirectional with the exception of some random artifacts at higher frequencies.

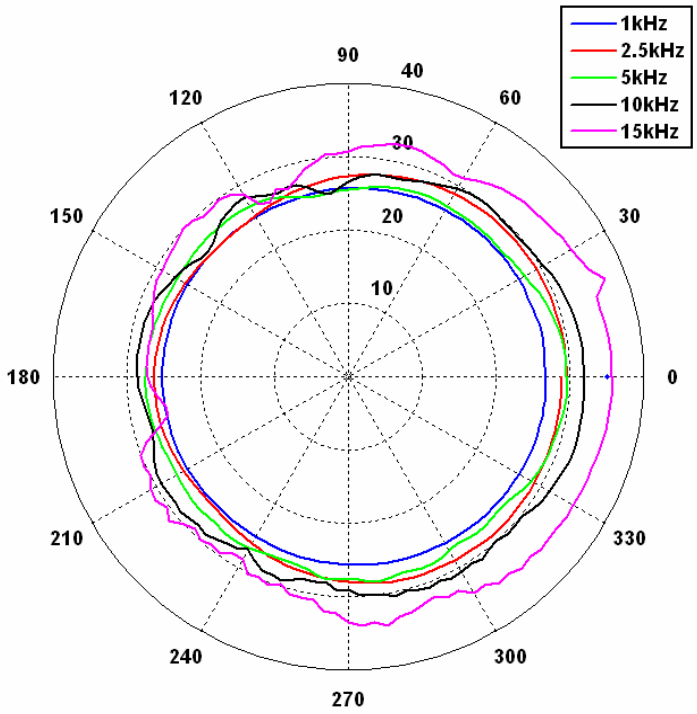

Figure 58. Measured directionality of the omnidirectional optical microphone and preamplifier tube (db: arbitrary ref).

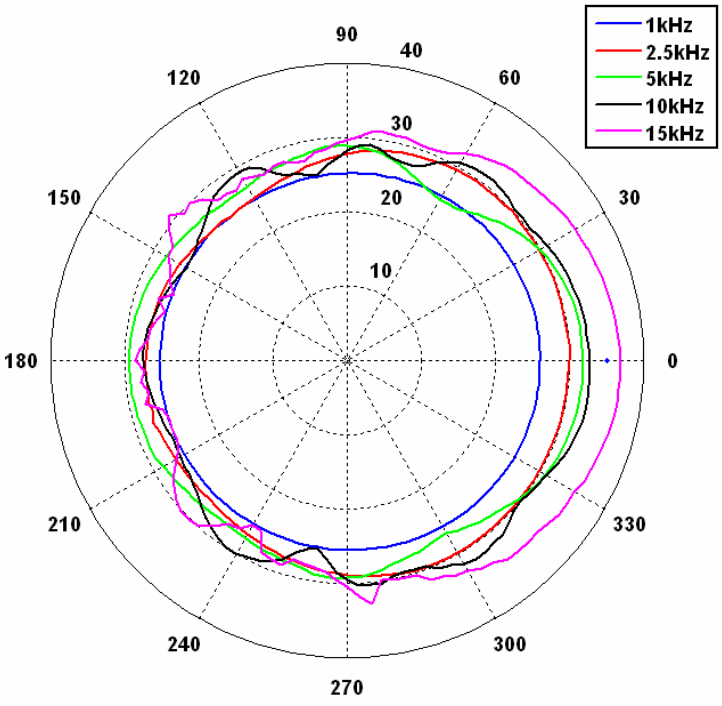

Figure 59. Measured directionality of the Larson Davis 2541 ½ inch measurement microphone and its preamplifier tube (dB: arbitrary ref).

Performance of the Biomimetic Directional Optical Microphone

The characterization of the biomimetic directional optical microphone with equivalent 1mm port spacing is similar to that of the omnidirectional optical microphone and begins with examination of the micro-optical modulation performance. Although this modulation performance is less than in the previous case, the biomimetic directional microphone characteristics are such that the available sensitivity is more than adequate to resolve thermal mechanical noise levels. Characterization again takes place in the Georgia Tech Integrated Acoustics Laboratory anechoic chamber and is conducted using the IO-MAP apparatus.

Modulation Performance of Sub-1mm^3 Optical Detection

The optical curve for the biomimetic directional microphone with a 100µm x 100µm diffraction grating region is graphed in Figure 60. Here, the optimal bias point of 3.9V yields a displacement sensitivity of 2.2mV/nm which is lower than that of the omnidirectional microphone structure. This lesser value is due to the fact that the biomimetic directional microphone is equipped with a grating area which is roughly half the size of the omnidirectional 200µm diameter grating. Consequently, the VCSEL light source has diverged beyond the grating region, resulting in a more pronounced DC intensity offset at the photodiode active area region and less modulation of the diffracted orders beams. Still, the optical detection architecture is able to demonstrate a displacement resolution of 2.5pm/√Hz at 1kHz.

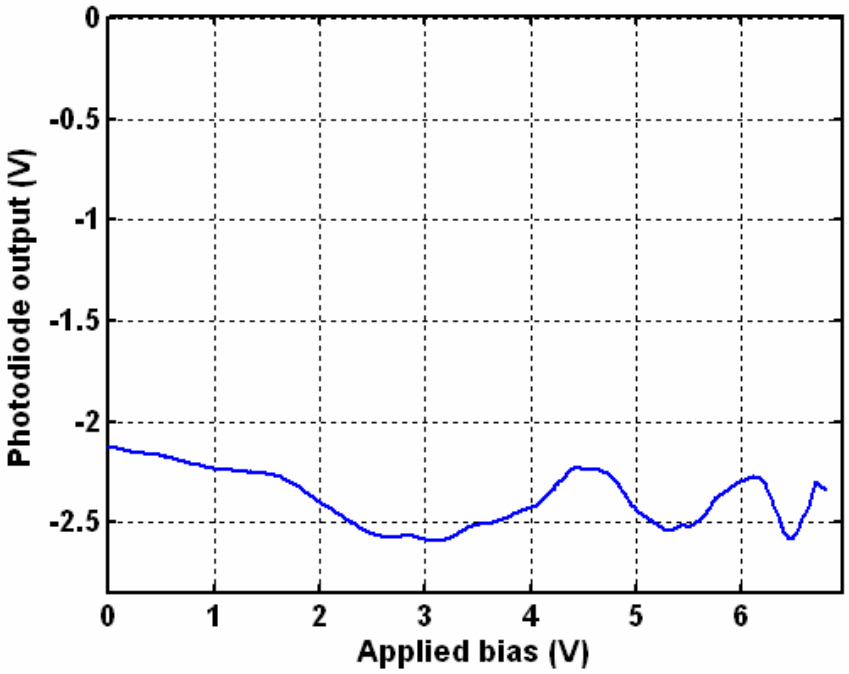

Figure 60. Optical curve for the biomimetic directional optical microphone measured using IO-MAP

Electrostatic and Acoustic Response Characterization

Figure 61 shows the optically measured frequency response of the biomimetic directional microphone when an electrostatic chirp signal is applied to the diaphragm via the reflective gold cantilever seen in Figure 5. Figure 62 gives the acoustic response of the biomimetic directional microphone in its most sensitive orientation. Although it is not included in earlier mathematical modeling, the second mode of vibration which corresponds to flapping motion of the diaphragm can be seen at approximately 16kHz where the ANSYS modal analysis results predict.

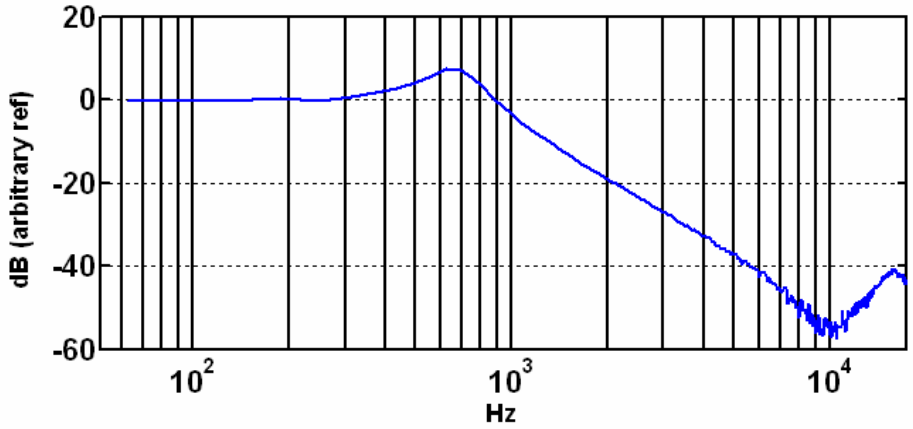

Figure 61. Biomimetic directional microphone frequency response obtained using electrostatic chirp excitation and optical detection

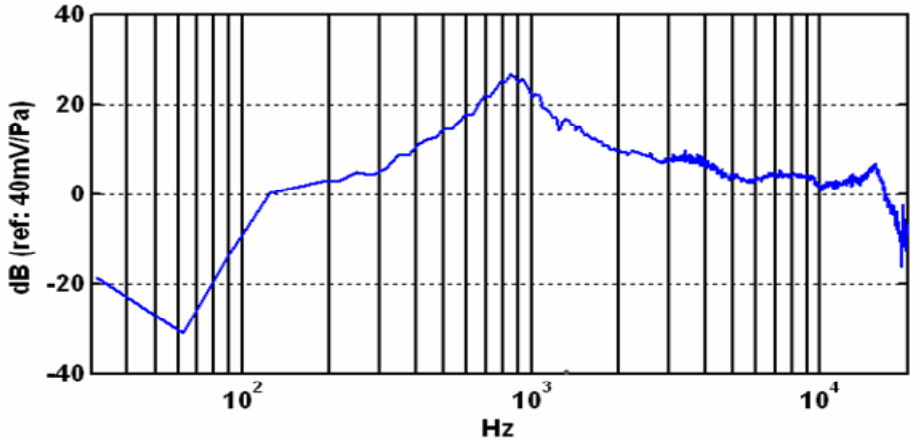

Figure 62. Biomimetic directional microphone frequency response using acoustic chirp excitation and optical detection

Reasonable agreement between these measured curves and the mathematical model is expressed by Figure 63. Note that in this sensitivity plot, the predicted sensitivity only takes into account the 1st resonant mode.

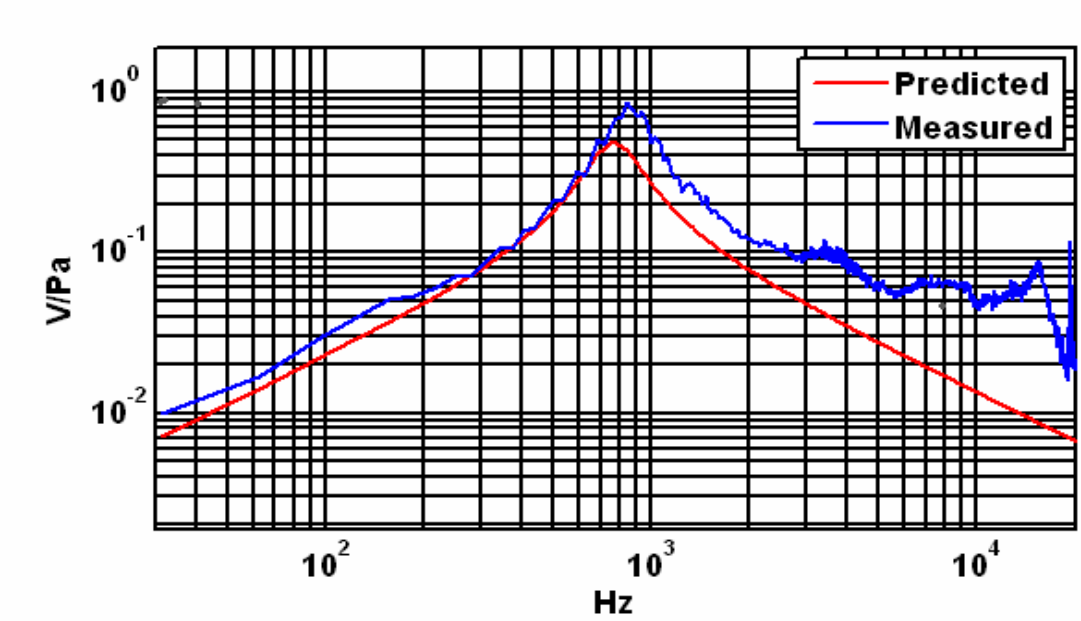

Figure 63. Comparison between measured sensitivity and mathematical predictions for the biomimetic directional optical microphone

Noise Performance

Noise characterization of the biomimetic directional microphone with 1mm equivalent port spacing follows the same procedure described above. From the measured noise spectrum of Figure 64, the A-weighted pressure noise spectrum is computed and shown in Figure 65 resulting in a 34dBA measured noise level. A few comments regarding these figures are worth noting. First, the noise for this microphone is dominated primarily by the thermal mechanical noise attributed to squeeze film damping of the air trapped between the grating region and the gold cantilever. Secondly, the contrast between the shot noise limit and the measured noise floor is much less than in Figure 52 for the case of the omnidirectional optical microphone. This is a consequence of the degradation in the optical modulation performance which results in lower displacement sensitivity. Finally, because the diaphragm is so soft, the displacement

resolution, despite being less than anticipated, is still able to resolve the thermal mechanical noise peak from 300Hz to 3kHz. Therefore, improving upon the measured 34dBA results of the biomimetic directional microphone would require mechanical design changes in this microphone structure.

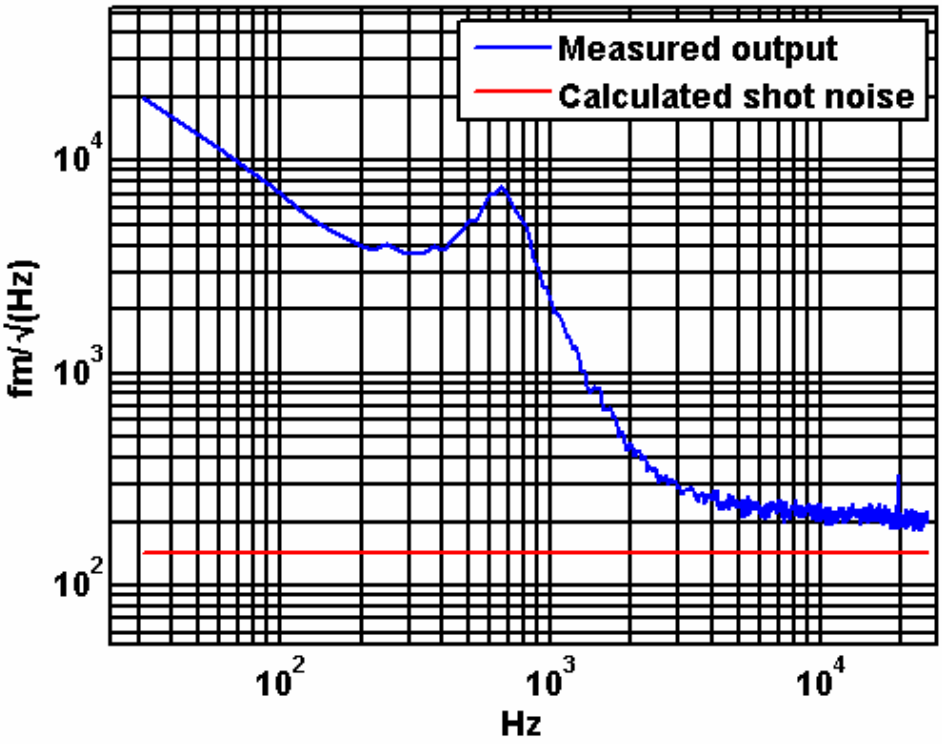

Figure 64. Comparison of measured noise to shot noise limit in terms of equivalent diaphragm displacement

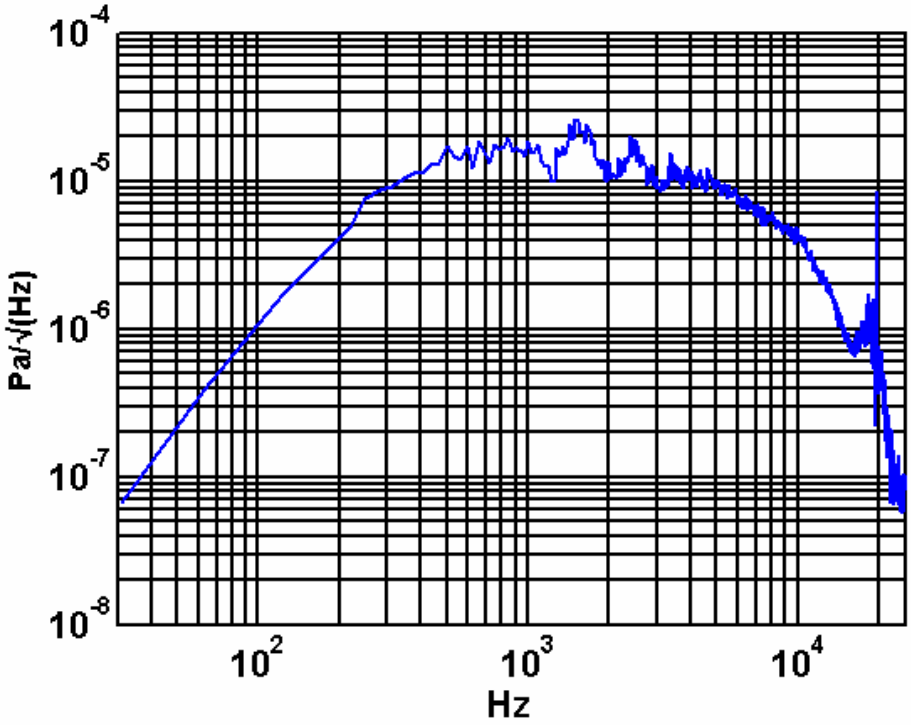

Figure 65. A-weighted pressure noise spectrum of the biomimetic directional microphone measured using the IO-MAP

Directionality Results and Optical Microphone Array Demonstration

Directionality measurements in this section serve two purposes. First, they demonstrate the improved performance of the IO-MAP over previous optical packaging schemes in terms of minimizing sound field disturbance. Secondly, they demonstrate the feasibility of miniaturized optical microphone arrays. Figure 66 provides the results for a directionality measurement made using a previous microphone testing apparatus. This plot reveals that the previous optical microphone test-bed disturbs the acoustic field resulting in measurement errors. Directivity measurements using the IO-MAP are more uniform and agree much better with FEM simulations as subsequent results show.

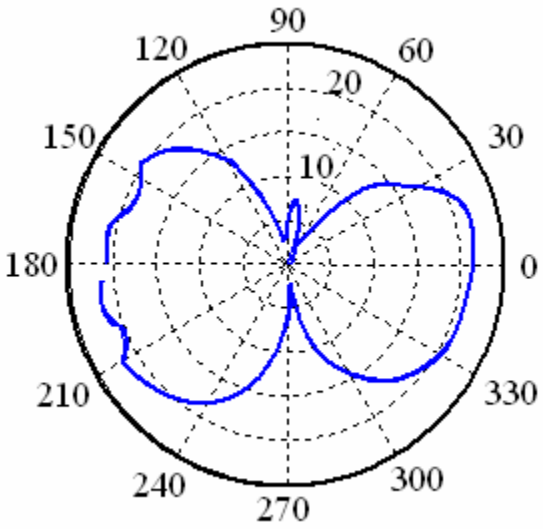

Figure 66. Measured directionality of a biomimetic directional microphone at 2kHz using previous test-bed packaging (dB: arbitrary ref)

An array of two biomimetic directional microphones in the initial orientation of the directionality measurement is illustrated in Figure 67 where the yellow circles represent the positioning of the two micro-optical detection localities. The fabrication of this array is similar to that of single element optical microphone headers with the exception that two micro-optoelectronic detection assemblies are required at precise relative spacing. Using a specialized routing PCB illustrated in Figure 69 of Appendix E, the optoelectronic components are positioned with a lateral accuracy of approximately 30μm. Directionality data for these two microphones is collected simultaneously through the stereo input of a sound card. The resulting gradient patterns of each microphone are seen in Figure 68 where the blue and red "figure 8" patterns belong respectively to microphones 1 and 2 in Figure 67. The measured DIs of these microphones are 4.6 and 3.5 respectively. These results match very closely to the FEM predictions in Chapter 4 and are much more uniform compared to previous test-bed measurements.

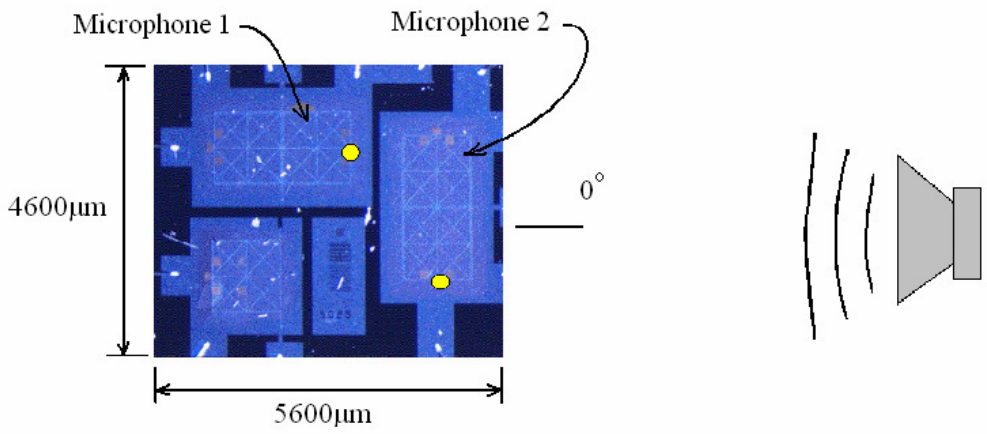

Figure 67. Directionality measurement orientation for dual biomimetic directional microphone array

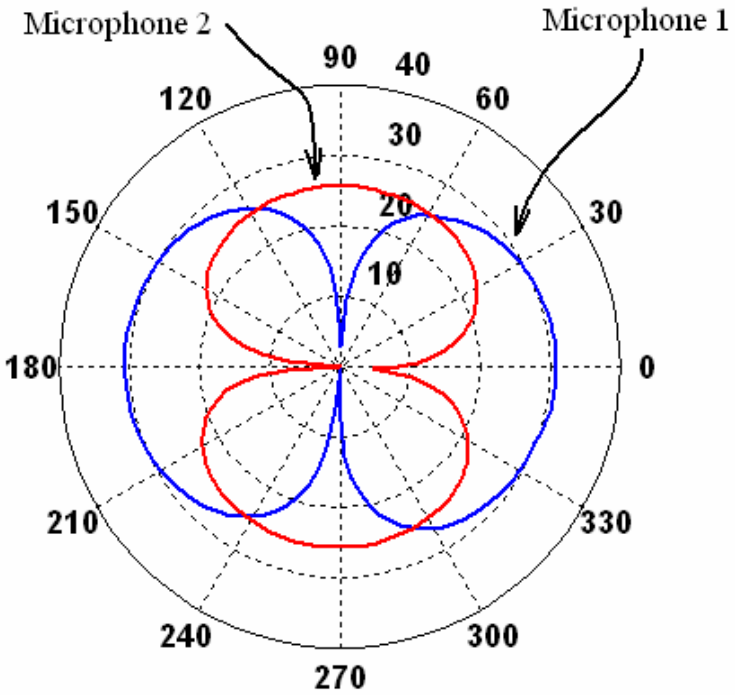

Figure 68. Measured directionality for an array of two biomimetic directional microphones at 1.5kHz (dB: arbitrary ref)

Comparisons

In order to gain a more complete appreciation for these results, a few comparisons are made to existing microphones in terms size and performance. First, the 2mm omnidirectional optical microphone is compared to similar omnidirectional free-field measurement microphones. Typical open-circuit sensitivity values for high quality measurement microphones range from about 10 to 50mV/Pa at 250 Hz. Measurement microphones usually exhibit various dBA noise levels depending on their size. For example, high quality ½-inch microphones can demonstrate noise floors as low as 15dBA while ¼-inch models are usually closer to 29dBA. A more complete summary of measurement microphone standards is provided in Table 4 [38]. The open-circuit sensitivity of the 2mm diameter omnidirectional optical microphone is 224mV/Pa which is considerably higher than these measurement microphones thanks to the excellent displacement sensitivity of the micro-optical detection method. Given this sensitivity, model predictions place the noise level of this device at 16.5dBA assuming shot noise limited detection; however measured results demonstrate 26dBA noise performance without differential order noise cancellation. Although the flat portion of the omnidirectional microphone only extends from 250-3000Hz in these results, improved vent hole fabrication and force feedback modalities have been shown to extend this bandwidth considerably without adding significant noise [39, 40].

Table 4: Typical performance of measurement microphones

Diameter	1inch	1/2inch	1/4inch	1/8inch
Open-circuit sensitivity	50	50	4	1
Noise (dBA)	10	14.5	29.5	-
Frequency response	2.6Hz-18kHz	2.6Hz-20kHz	4Hz-70kHz	6.5Hz-140Hz

Some relevant properties for comparing directional microphones include port spacing, sensitivity, and noise. The biomimetic directional optical microphone has equivalent 1mm port spacing and can be compared to standard hearing aid microphones with 10mm port spacing such as the Knowles TP-4605 directional series. However, the sensitivity of directional microphones is not flat and it is difficult to make meaningful comparisons based on manufacturer's specifications. Regardless, the micro-optical detection method allows the biomimetic directional microphone to exhibit a sensitivity of 400mV/Pa at 1kHz while the TP-4605 demonstrates 13mV/Pa at 1kHz. Finally, the biomimetic directional microphone has a measured noise floor of 34dBA while the TP-4605 series is closer to 42dBA. In both the biomimetic directional microphone and the TP-4605 microphone, directional response patterns provide off-axis noise suppression in excess of 20dB and in some cases as much as 30dB for the biomimetic design [36, 41].

CHAPTER 6

CONCLUSIONS

Micromachined microphones with sub $1mm^3$ diffraction-based optical displacement detection have been packaged and characterized. The aim of these efforts is to demonstrate this miniaturized detection method as an alternative to traditional capacitive detection in small scale applications such as hearing aids where both size and performance are of critical importance. In pursuit of this end, the micro-optical system was optimized through computer simulation using well known Fresnel diffraction theory. Conclusive results from this model were used to design and assemble the micro-optical detection architecture. A platform based on existing measurement microphone designs was constructed in order to assess the performance of the micro-optical detection scheme. Using this testing platform, detailed characterization of two unique optical microphone designs was carried out and results are presented and compared with analogous industry leading condenser microphones.

A computer model for a Michelson type interferometer based on a phase-sensitive grating geometry was constructed. From model simulations, two important observations were obtained. The first observation was that the divergence angle of a VCSEL source is responsible for a significant degradation in the overall performance of the proposed detection method. Divergence angles as small as 8^o based on half angle beam divergence, are responsible for undesirable overlapping of the diffracted order intensities. As a consequence of this overlap, the second observation was that the optimal locations for detection of the modulated order intensities do not exactly coincide with the diffracted

orders locations. Simulations were therefore used to obtain the optimal placement of the optoelectronic components and to specify the appropriate separation between the grating plane and the source plane containing the optoelectronic components. From this model, an estimated 35mV/nm was predicted assuming the optical surfaces (grating and diaphragm) are perfectly reflective. For the microphones tested however, this is not the case. In fact, for the omnidirectional microphone, the presented transmission layer model suggests that up to 51% of the VCSEL light is lost from the system via transmission through the polysilicon diaphragm. Degradation in the optical performance of the biomimetic directional microphone design comes as a result of the grating region being smaller than the spot size of the diverging source as it reaches the grating. In general these non-ideal conditions lead to large DC offsets as well as diminishing modulation levels in the captured photocurrents. Nevertheless, the model estimates sufficient electrical sensitivity, S_e, for high resolution displacement detection given the simple micro-optoelectronic design. It is notable that these predictions do not require the use of any focusing optics or tilting configurations which compound the complexity of the microscale package.

A modular design for implementing the microscale optical detection method was constructed in the form of the IO-MAP which consists of three main assemblies. The microphone header is the first of these assemblies and contains the miniaturized optical detection architecture. The microphone header packaging is minimized using SLA components which serve a variety of purposes. First, these SLA structures serve as precise spacers which set the appropriate separation, z_i, established by the optical model. Second, a back volume was designed within the SLA material, which is aimed at

maximizing the overall mechanical sensitivity, S_m, by reducing the cavity compliance. Finally, this SLA structure is responsible for supplying a vent hole resistance which sets the lower cutoff frequency in the acoustic response. The remaining entities of the IO-MAP are designed to accommodate rapid, non-invasive, acoustic testing of multiple optical microphones and optical microphone arrays.

The results presented in this thesis agree well with model projections and confirm that the micro-optical detection method is an alternative to capacitive detection for miniaturized microphones. Optical modulation and noise measurements demonstrate displacement resolutions of 150fm/√Hz at 1 kHz for the omnidirectional and 2.5pm/√Hz at 1kHz for the biomimetic directional optical microphones. The acoustic frequency response the omnidirectional optical microphone structure demonstrates a relatively flat response up to its resonance at 13kHz. The sensitivity of the biomimetic directional microphone on the other hand is heavily dependant on frequency and its frequency response shows resonant modes occurring at 700Hz and 16kHz and matching FEM predictions. Measured noise levels of 26dBA for the omnidirectional and 34dBA for the biomimetic directional microphones, not to mention the potential gains in noise performance using differential order detection, confirm the excellent performance of the sub-1mm^3 optical detection scheme. Finally, measured directivity patterns provide proof that the IO-MAP packaging imposes minimal disturbance to the measured sound field and boast the achievement of an array of two biomimetic directional optical microphones separated by less than 5mm.

Recommendations

A few suggestions are offered for future improvements and characterization. Some of these recommendations are anticipated by the IO-MAP architecture and others require the investigation and design of new packaging schemes. The first item of contingence is the consistent cancellation of laser intensity noise down to shot noise limitations. It is recommended that this task be accomplished in one of two ways. One option is to incorporate a variable gain component within the IO-MAP preamplifier tube which would allow intensity order equalization required by simple differential multiplier circuits. The preferred solution is to implement the suggested circuitry for differential detection in the current domain. Either solution promises significant gains in noise performance for cases where laser RIN is the dominant noise source. It is possible to improve noise performance by improving the reflectivity of optical surfaces to avoid significant transmission losses. As the optical power losses decrease, potential gains in displacement sensitivity should outweigh the anticipated increase in shot noise levels due to the square root dependence of these levels.

The limitations on power consumption for miniaturized microphone applications can be quite stringent. For these applications, pulsed VCSEL operation should be investigated further. Particularly, the effect of pulsed VCSEL operation on noise performance should be thoroughly assessed. A suggested experiment can be conducted using the IO-MAP and would require the input of a square wave signal with a variable duty cycle in order to drive the VCSEL thereby resulting in a discritized output signal. Accurate reconstruction of the continuous-time output signal from the sampled output then requires a low pass filter with the appropriate gain selected according to basic

sampling theory. The output from the low pass filter can then be analyzed as a function of the input power and corresponding duty cycle [42].

Two final suggestions for future work involve the modification of dynamic properties. The first applies to the omnidirectional optical microphone. By decreasing the size of the vent holes using more precise techniques such as focused ion beam drilling, the vent hole resistance can be increased thereby extending the low frequency response of the microphone. A final suggestion is that electrostatic force feedback operation be demonstrated as a tool for tailoring microphone dynamics. This demonstration will further emphasize the advantages of the optical detection method over other microphone technologies.

APPENDIX A

OPTICAL MODELING CODE

```
%%%%%%%%%%%%%%%%%%%%%%%%%%%%%%%%%%%%%%%%%%%%%%%%%%%%%%%%%%%%%%%%%%%%%%%%
% Optical model of phase sensitive diffraction gratings
% using the Fourier representation for the Fresnel
% approximation of the Fresnel-Kirchhoff diffraction
% formula. Code assumes a diverging VCSEL source and
% computes the intensity at a given field location.
%%%%%%%%%%%%%%%%%%%%%%%%%%%%%%%%%%%%%%%%%%%%%%%%%%%%%%%%%%%%%%%%%%%%%%%%
clear;
P     =2e-3;   %VCSEL Optical power W
lambda=850e-9; %VCSEL wavelength
z     =650e-6; %distance from vcsel to grating
L     =800e-6; %distance from grating to PD array
Wst   =2.27e-6;%2um wst gives approximately 10deg
               %2.27um gives 8deg
k=2*pi/lambda; %10 degree divergence FAHM
fill  =50;     %grating duty cycle
Tg    =4e-6;   %grating period
Phi   =[0,pi]; %relevant cases are phi=0,pi/2, and pi
Nx    =8192;
Ny    =512;

%%%%%%%%%%%%% CREATE SPACE AXIS %%%%%%%%%%%%%%
vx      =linspace(-1.5e-3,1.5e-3,Nx);
deltax  =vx(2)-vx(1); Tx=Nx*deltax;
vy      =linspace(-.5e-3,.5e-3,Ny);
deltay  =vy(2)-vy(1); Ty=Ny*deltay;
   =meshgrid(vx,vy);
%%%%%%%%%%%%%%%%%%%%%%%%%%%%%%%%%%%%%%%%%%%%%%%

%%%%%%% CREATE SPATIAL FREQUENCY AXIS %%%%%%%%
fx_v    =-1/Tx*(Nx/2-1):1/Tx:1/Tx*Nx/2;
fy_v    =-1/Ty*(Ny/2-1):1/Ty:1/Ty*Ny/2;
[fx,fy] =meshgrid(fx_v,fy_v);
%%%%%%%%%%%%%%%%%%%%%%%%%%%%%%%%%%%%%%%%%%%%%%%

u1      =sqrt(2*P/(pi*wst^2))*exp(-(x.^2+y.^2)/wst^2);
temp1   =u1.*exp(i*k/(2*z)*(x.^2+y.^2));
temp2   =Tx/Nx*Ty/Ny*fftshift(fft2(temp1));
clear u1; clear temp1;

%%%%%%% CREATE NEW SPACE AND FREQUENCY AXIS %%%%%%%
```

```
clear fx; clear fy; clear x; clear y;
vx      =fx_v*lambda*z;
vy      =fy_v*lambda*z;
[x,y]   =meshgrid(vx,vy);
deltax  =vx(2)-vx(1); Tx=Nx*deltax;
fx_v    =-1/Tx*(Nx/2-1):1/Tx:1/Tx*Nx/2;
deltay  =vy(2)-vy(1); Ty=Ny*deltay;
fy_v    =-1/Ty*(Ny/2-1):1/Ty:1/Ty*Ny/2;
[fx,fy] =meshgrid(fx_v,fy_v);
%%%%%%%%%%%%%%%%%%%%%%%%%%%%%%%%%%%%%%%%%%%%%%%%%%%%%%%%%%%%

u2      =temp2.*exp(i*k*z)/(i*lambda*z).*exp(i*k/(2*z)
         *(x.^2+y.^2));
clear temp2;
figure(5); plot(vx*1e3,(abs(u2(Ny/2,:))).^2);
xlabel('x (mm)'); ylabel ('u2^2');

%%%%%%%%%%CREATE GRATING FUNCTION %%%%%%%%%%%%%
g_v       =.5*(1+square(2*pi/Tg*vx,fill));
g_v       =circshift(g_v,[0,floor(Tg/deltax/4)+1]);
[g1,dummy]=meshgrid(exp(i*phi(1)*g_v),vy); clear dummy;
[g2,dummy]=meshgrid(exp(i*phi(2)*g_v),vy); clear dummy;
%%%%%%%%%%%%%%%%%%%%%%%%%%%%%%%%%%%%%%%%%%%%%%%%%%%%%%%%%%%%

figure(6); stem(vx*1e3,g_v); xlabel('x mm');

u2_bar1 =u2.*g1;u2_bar2=u2.*g2;clear u2;clear g1;clear g2;
temp1_1 =u2_bar1.*exp(i*k/(2*L)*(x.^2+y.^2));
temp1_2 =u2_bar2.*exp(i*k/(2*L)*(x.^2+y.^2));
temp2_1 =Tx/Nx*Ty/Ny*(fft2(temp1_1));
clear u2_bar1;clear temp1_1;
temp2_2 =Tx/Nx*Ty/Ny*(fft2(temp1_2));
clear u2_bar2;clear temp1_2;

%%%%%%% CREATE NEW SPACE AND FREQUENCY AXIS %%%%%%%
clear fx; clear fy; clear x; clear y;
vx      =fx_v*lambda*L;
vy      =fy_v*lambda*L;
[x,y]   =meshgrid(vx,vy);
deltax  =vx(2)-vx(1); Tx=Nx*deltax;
fx_v    =-1/Tx*(Nx/2-1):1/Tx:1/Tx*Nx/2;
deltay  =vy(2)-vy(1); Ty=Ny*deltay;
fy_v    =-1/Ty*(Ny/2-1):1/Ty:1/Ty*Ny/2;
[fx,fy] =meshgrid(fx_v,fy_v);
%%%%%%%%%%%%%%%%%%%%%%%%%%%%%%%%%%%%%%%%%%%%%%%%%%%%%%%%%%%%
```

```
u3_1=temp2_1.*exp(i*k*L)/(i*lambda*L).*exp(i*k/(2*L)*(x.^2+
     y.^2)); clear temp2_1;
u3_2=temp2_2.*exp(i*k*L)/(i*lambda*L).*exp(i*k/(2*L)*(x.^2+
     y.^2)); clear temp2_2;

figure(9); imagesc(vx*1e3,vy*1e3,abs(u3_1).^2);
xlabel('x (mm)'); ylabel('y (mm)');
title(['u3_1^2  (phi=', num2str(phi(1)),')']);

figure(10); imagesc(vx*1e3,vy*1e3,abs(u3_2).^2);
xlabel('x (mm)'); ylabel('y (mm)');
title(['u3_2^2  (phi=',num2str(phi(2)),')']);

figure(11); plot(vx*1e3,(abs(u3_1(Ny/2,:))).^2,'b');
hold on;
            plot(vx*1e3,(abs(u3_2(Ny/2,:))).^2,'g');
legend(['phi=',num2str(phi(1)),'  phi=',num2str(phi(2))]);
xlabel('x (mm)'); ylabel ('u3^2');

U3_1=abs(u3_1(Ny/2,:)).^2;
U3_2=abs(u3_2(Ny/2,:)).^2;
figure(12); plot(vx*1e3,smooth(abs(U3_2-
U3_1)./max([U3_2;U3_1]),60));
xlabel('x (mm)'); ylabel('% Modulation');
title('modulation');

%%%%%%% Calculate Power falling on ULM PD  %%%%%%%%%%%%%%%
x_cen   =250E-6;
R       =50E-6;
r       =sqrt((x-x_cen).^2+y.^2);  clear x; clear y;
test    =R*ones(size(r));
truth   =r<test;
u3_1    =u3_1.*truth;
u3_2    =u3_2.*truth;
dA      =(3e-3*1e-3)/Ny/Nx;
P3_1    =sum(sum(dA*abs(u3_1).^2));         % W
P3_2    =sum(sum(dA*abs(u3_2).^2));         % W
dsens   =abs(P3_2-P3_1)*.5*2*pi/lambda      % A/m
figure(13); imagesc(vx*1e3,vy*1e3,abs(u3_1).^2);
%%%%%%%%%%%%%%%%%%%%%%%%%%%%%%%%%%%%%%%%%%%%%%%%%%%%%%%%%%%
```

APPENDIX B

COMPLIANCE OPTIMIZATION CODE

```
%%%%%%%%%%%%%%%%%%%%%%%%%%%%%%%%%%%%%%%%%%%%%%%%%%%%%%%%%%%%%%%%%%%%%%%
% This m-file tells how much backvolume is necessary given
% the 40fm/sqrt(Hz) limit. The dominant noise source is
% assumed to be thermal noise and therefore sqrt(4kTR) is
% used to compute displacement noise.  Given a minimum
% displacement resolution, compliance is adjusted (using an
% SLA backvolume) to ensure displacement noise levels
% remain above this level.
%%%%%%%%%%%%%%%%%%%%%%%%%%%%%%%%%%%%%%%%%%%%%%%%%%%%%%%%%%%%%%%%%%%%%%%
clc; clear;
%% 2mm diaphragm %%%%%%%%%%
fo=      11100;      % from electrostatic freq resp
zeta=    .15;        % from electrostatic freq resp
r=       1e-3;       % m
A=       pi*r^2;     % m^2
th=      2.25e-6;    % m
rho=     2330;       % polysilicon density
M=       rho*A*th/6; % kg   from theory circular plate
wo=      2*pi*fo;
cmp=A/k;             % m/Pa

%% 2nd order system
k= M*wo^2;           % N/m or Pa*m
C= M*zeta*2*wo;      % N/m/s

%% compute thermal noise force
Fn= sqrt(4*298*1.3806503e-23*C);    % N/rt(Hz)
dn= Fn*4*1e15/k;                    % fm/rt(Hz), disp noise
Pn= (dn/1e15)/cmp;                  % Pa/rt(Hz), pres noise

%% dBA approximation
dBA= 20*log10(Pn*sqrt(15000)/2e-5)  % Assume th-noise limit

%% Added Backvolume compliance
Vcav=A*400e-6+650e-6*5e-3*5e-3;
Kcav=(1.2*343^2/Vcav);              % Pa/m^3 Units!!!!
cmp_tot=1/(1/cmp+Kcav*A);           % m/Pa
dn_sealed= Pn*cmp_tot*1e15          % IO-MAP detects 40fm
```

APPENDIX C

NOISE MODELING CODE

```
%%%%%%%%%%%%%%%%%%%%%%%%%%%%%%%%%%%%%%%%%%%%%%%%%%%%%%%%%%%%%%%%%%%%%%%
% Noise modeling for 2mm omnidirectional optical microphone
%
% This m-file models the noise performance of the 2mm
% diaphragm structure using a lumped mass approximation.
% The thermal mechanical noise force is applied to this
% model in order to simulate the best possible noise
% performance. Actual measurements made using the IO-MAP
% are compared to these simulations
%%%%%%%%%%%%%%%%%%%%%%%%%%%%%%%%%%%%%%%%%%%%%%%%%%%%%%%%%%%%%%%%%%%%%%%

 clc;
 clear;

%% 2mm diaphragm %%%%%%%%%
r=       1e-3;       % m
Area=    pi*r^2;     % m^2
th=      2.25e-6     % m
M=       2330*Area*th/6; % kg  from theory circular plate
fo=      11100;          % measured electrostatically
wo=      2*pi*fo;
zeta=    .15;            % measured electrostatically
Vhigh=   2.23;           % V optical curve
Vlow=    .81;            % V optical curve
Rfb=     200000;         % Ohm
cmp=     44e-9;          % m/Pa from Ccav optimization
k=       Area/cmp;       % N/m
C=       2*zeta*wo*M;    % N/sqrt(Hz)

%% Parameters for RC high-pass calc
rho=    1.2;             % density of air(kg/m^3)
co=     343;             % speed of sound in air(m/s)
visc=   1.82e-5          % viscosity of air (Pa*s)
d_hole= 60e-6;            % vent hole diameter (m)
d_dia=  2e-3;            % diaphragm diameter (m)
h=      250e-6;          % diaphragm thickness (m)
t_chip= 400e-6;          % chip thickness (m)
Vcav=t_chip*pi*(d_dia/2)^2+(16/(1e3)^3);
     % total cavity volume (m^3)
```

```
%% Optical Curve Results
Vp2p=   Vhigh-Vlow;
Vdc=    Vp2p/2+Vlow;            % approximate
dsens=  2*pi*Vp2p/(850e-9);     % V/m

%% Measured noise
load sandia_2mm_noise.txt;      % measured noise
a= sandia_2mm_noise;
f=a(:,1); db=a(:,2); v=10.^(db/20);
dn_meas=v/dsens;
pn_meas=dn_meas/cmp;
w=2*pi*f;

%% Estimate thermal noise
Fn_th=   sqrt(4*298*1.38e-23*C);  % N/sqrt(Hz)
Ccav=   Vcav/rho/(co^2);          % m/Pa cavity compliance
Rvent=  (8*visc*h)./(pi*(d_hole/2).^4);
     % Pa s/m orifice resistance
tau=    Rvent*Ccav;                % 1/s
x=abs((1-1./(tau*i*w+1))./((1-(w/wo).^2)+i*2*zeta*w/wo));
     % 2nd order 1 DOF damped system with RC high-pass
dn_th=  Fn_th*4*x/k;
     % m/sqrt(Hz), factor of 4 accounts for curvature
cmpx=   cmp.*(x./(x(35)));
pn_th=  dn_th./cmpx;

%% Compute Shot Noise Limit
Vshot= sqrt(2*1.602e-19*Rfb*Vdc);
dn_shot_eq=Vshot/dsens;             % m/sqrt(Hz)
dn_shot=dn_shot_eq*ones(1,length(f));

%% Apply A-weighting funciton for measured noise
signalp=pn_meas.^2;               % Pa^2/Hz noise spectrum
A=((3.5041384.*1e16.*f.^8)./(((20.598997^2+f.^2).^2).*(107.
65265^2+f.^2).*(737.862^2+f.^2).*((12194.217^2+f.^2).^2)));
     % A weighted filter
W=(A.^2).*signalp;                % multiply the signal
     power with the filter^2
sums=sum(W);
sums=sums*(f(2)-f(1));
sums=sqrt(sums);
dBA_meas=20*log10(sums/(2*1e-5))

%% Apply A-weighting function for thermal noise
signalp=pn_th.^2;                % Pa^2/Hz noise power
W=(A.^2).*signalp;               % multiply the signal
```

```
     power with the filter^2
sums=sum(W);
sums=sums*(f(2)-f(1));
sums=sqrt(sums);
dBA_th=20*log10(sums/(2*1e-5))

figure(1);
loglog(f,dn_meas*1e15,'r'); hold on; grid on;
loglog(f,dn_th*1e15,'b');
loglog(f,dn_shot*1e15,'y');
xlabel('Hz'); ylabel('fm/\surd(Hz)');
legend('Measured output','Estimated thermal
noise','Calculated shot noise');

figure(2);
loglog(f,sqrt(W)); grid on;
xlabel('Hz'); ylabel('Pa/\surd(Hz)'); title('A-weighted
thermal noise limit')

figure(3);
loglog(f,dn_th*1e15); grid on;
xlabel('Hz'); ylabel('fm/\surd(Hz)');
```

APPENDIX D

ANSYS CODE FOR BIOMIMETIC MICROPHONE STRUCTURE

```
! Log file to create diffmic with gap next to the central pivot for stress relief
! This file can be used to model the diffmic for various gap sizes
!
finish
/clear,nostart
/title,diffnew
/prep7                          !clear the database
ET,1,SHELL93
ET,2,MATRIX27,,0,4,1

! Define geometry
*SET,xlength,1000
*SET,ylength,500
*SET,skint,1                    ! Skin thickness for diaphragm
*SET,stifft,2                   ! Thickness of stiffeners
*SET,stiffdepth,20              ! Depth of stiffeners
*SET,tlength,200                ! Length of T-section support
*SET,twidth,20                  ! Width of the T on each side
*SET,gap,20                     ! Gap in skin near the central pivot

! Effect of backvolume
*SET,rho0,1.2064e-18
*SET,c,344e6
*SET,A,xlength*(2*ylength)
*SET,h,380                      ! Depth of backvolume: 380 microns
*SET,V,(2*xlength)*(2*ylength)*h

! define material parameters
*SET,youngs,170000
*SET,possion,0.3
*SET,density,2.3e-15
*SET,CTE,0.2941e-6              ! Based on stress=E*alpha*dT  (for 50 MPa stress)
R,1,skint,skint,skint,skint, , ,  ! material properties
R,2,stifft,stifft,stifft,stifft, , ,
R,3                             ! Stiffness matrix
RMODIF,3,24,springstiff
RMODIF,3,30,springstiff
RMODIF,3,69,springstiff

UIMP,1,EX, , ,youngs,
```

```
UIMP,1,NUXY, , ,possion,
UIMP,1,DENS, , ,density,
UIMP,1,ALPX , , ,CTE,

! Create keypoints for unit cell: for skin
k,1,0,0
k,2,twidth,0
k,3,twidth+gap,0
k,4,(twidth+gap)+(xlength-(twidth+gap))/2,0
k,5,xlength,0
k,6,0,-ylength/2
k,7,twidth,-ylength/2
k,8,twidth+gap,-ylength/2
k,9,(twidth+gap)+(xlength-(twidth+gap))/4,-ylength/2
k,10,(twidth+gap)+3*(xlength-(twidth+gap))/4,-ylength/2
k,11,0,-ylength
k,12,twidth,-ylength
k,13,twidth+gap,-ylength
k,14,(twidth+gap)+(xlength-(twidth+gap))/2,-ylength
k,15,xlength,-ylength

! Create keypoints for stiffeners
k,16,0,0,-stiffdepth
k,17,twidth,0,-stiffdepth
k,18,twidth+gap,0,-stiffdepth
k,19,(twidth+gap)+(xlength-(twidth+gap))/2,0,-stiffdepth
k,20,xlength,0,-stiffdepth
k,21,0,-ylength/2,-stiffdepth
k,22,twidth,-ylength/2,-stiffdepth
k,23,twidth+gap,-ylength/2,-stiffdepth
k,24,(twidth+gap)+(xlength-(twidth+gap))/4,-ylength/2,-stiffdepth
k,25,(twidth+gap)+3*(xlength-(twidth+gap))/4,-ylength/2,-stiffdepth
k,26,0,-ylength,-stiffdepth
k,27,twidth,-ylength,-stiffdepth
k,28,twidth+gap,-ylength,-stiffdepth
k,29,(twidth+gap)+(xlength-(twidth+gap))/2,-ylength,-stiffdepth
k,30,xlength,-ylength,-stiffdepth

! Create the T
k,31,0,-(ylength+tlength)
k,32,twidth,-(ylength+tlength)
k,34,0,-(ylength+tlength),-stiffdepth

! Create skin of diaphragm
l,1,2
l,2,3
```

l,3,4
l,4,5
l,5,15
l,15,14
l,14,13
l,12,11
l,11,6
l,6,1
l,6,7
l,7,2
l,7,12
l,7,8
l,8,3
l,8,13
l,8,9
l,9,3
l,9,13
l,9,4
l,9,14
l,4,14
l,10,4
l,10,5
l,10,14
l,10,15
l,1,16
l,16,17
l,17,2
l,17,18
l,18,3
l,18,19
l,19,4
l,19,20
l,20,5
l,20,30
l,30,15
l,30,29
l,29,14
l,29,28
l,28,13
l,27,12
l,27,26
l,26,11
l,26,21
l,21,6
l,21,16 ! Line number 47
l,21,22

```
l,22,7
l,22,23
l,23,8
l,23,24
l,24,9
l,18,23
l,23,28
l,18,24
l,24,28
l,24,19
l,24,29
l,19,29
l,25,19
l,25,20
l,25,29
l,25,30          ! Line number 64
l,25,10

! T-section lines
l,11,31
l,31,34
l,34,26
l,31,32
l,32,12
l,13,12
l,28,27

! Create areas using defined lines
AL,1,10,11,12
AL,8,9,11,13
AL,15,17,18
AL,16,17,19
AL,3,18,20
AL,7,19,21
AL,20,21,22
AL,22,23,25
AL,4,23,24
AL,6,25,26
AL,5,24,26
AL,8,66,69,70
AL,1,27,28,29
AL,2,29,30,31
AL,3,31,32,33
AL,4,33,34,35
AL,5,35,36,37
AL,6,37,38,39
```

```
AL,7,39,40,41
AL,8,42,43,44
AL,9,44,45,46
AL,10,46,47,27
AL,44,66,67,68
AL,11,46,48,49
AL,14,49,50,51
AL,17,51,52,53
AL,15,51,54,31
AL,16,51,55,41
AL,18,53,56,31
AL,19,53,57,41
AL,20,53,58,33
AL,21,53,59,39
AL,22,39,60,33
AL,23,65,61,33
AL,24,65,62,35
AL,25,65,63,39
AL,26,65,64,37
AL,41,71,42,72

! Select lines for line sizing
LSEL,S,LINE,,9,10,1
LSEL,A,LINE,,12,13,1
LSEL,A,LINE,,15,26,1
LSEL,A,LINE,,3,7,1
LSEL,A,LINE,,32,40,2
LSEL,A,LINE,,45,47,2
LSEL,A,LINE,,52
LSEL,A,LINE,,54,64,1
LESIZE,ALL,,,10
LSEL,S,LINE,,27,41,2
LSEL,A,LINE,,42,46,2
LSEL,A,LINE,,49,53,2
LSEL,A,LINE,,65,67,2
LESIZE,ALL,,,2
LSEL,S,LINE,,1,2,1
LSEL,A,LINE,,11,14,3
LSEL,A,LINE,,8
LSEL,A,LINE,,28,30,2
LSEL,A,LINE,,48,50,2
LSEL,A,LINE,,43
LSEL,A,LINE,,69,71,2
LSEL,A,LINE,,72
LESIZE,ALL,,,1
LSEL,S,LINE,,66,70,2
```

```
LESIZE,ALL,,,10
ASEL,S,LOC,Z,0
AATT,1,1
AMESH,ALL
NUMMRG,ALL
NUMCMP,ALL
ASEL,ALL
ASEL,U,LOC,Z,0
AATT,1,2
AMESH,ALL
NUMMRG,ALL
NUMCMP,ALL

! Use symmetry to model the entire diffmic
ALLSEL,ALL
ARSYM,X,ALL,,,,0,0
ARSYM,Y,ALL,,,,0,0
NUMMRG,ALL
NUMCMP,ALL

! Create a MATRIX27 element (stiffness) between the centers of each half
! Get center locations of each half of the diffmic and use these to create a spring element.
NSEL,S,LOC,Z,-stiffdepth
NSEL,R,LOC,X,(twidth+gap)+(xlength-(twidth+gap))/2
NSEL,R,LOC,Y,0
*GET,N1,NODE,,NUM,MAX
ALLSEL,ALL
NSEL,S,LOC,Z,-stiffdepth
NSEL,R,LOC,X,-((twidth+gap)+(xlength-(twidth+gap))/2)
NSEL,R,LOC,Y,0
*GET,N2,NODE,,NUM,MAX
ALLSEL,ALL

! Apply constraints for modal analysis
LSEL,S,LOC,Y,(ylength+tlength)
LSEL,A,LOC,Y,-(ylength+tlength)
DL,ALL,,ALL
allsel,all
FINISH
```

APPENDIX E

ROUTING PCB FOR ACOUSTIC ARRAY

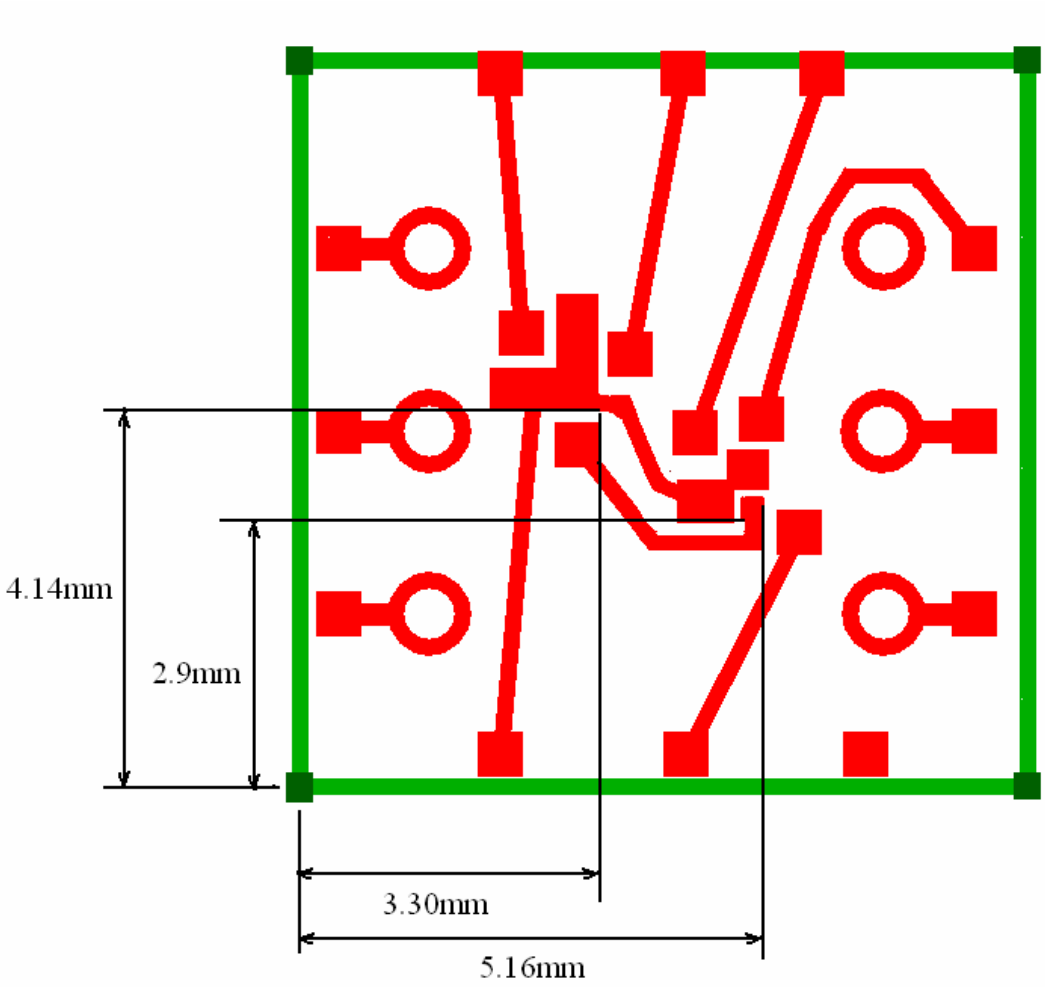

Figure 69. Routing PCB with accurate optoelectronic positioning for dual biomimetic directional microphone array

APPENDIX D

PCB LAYOUT FOR PREAMPLIFIER ELECTRONICS

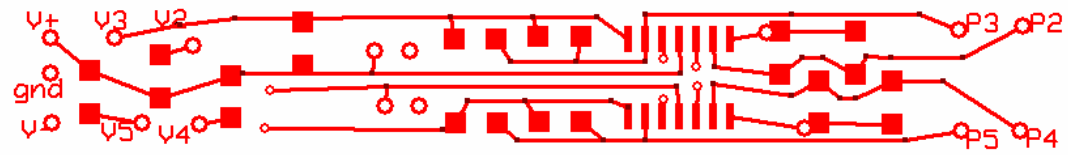

a)

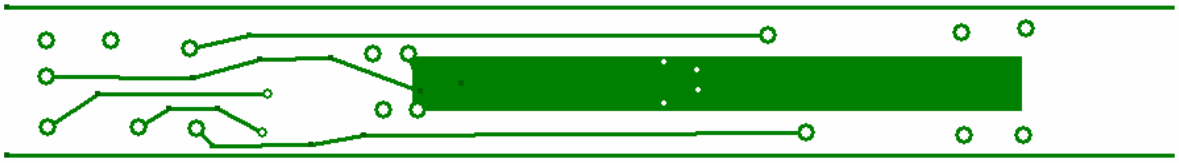

b)

Figure 70. PCB layout for preamplifier electronics a) front layer b) back layer

REFERENCES

[1] John Eargle, *The Microphone Book.* Oxford: Elsevier, 2004.

[2] L. L. Beranek, *Acoustical Measurements.* Woodbury, NY: American Institute of Physics, 1988.

[3] D. T. Martin, J. Liu, K. Kadirvel, R. Fox, M. Sheplak, and T. Nishida. *Development of a MEMS dual backplate capacitive microphone for aeroacoustic measurements*. in *44th AIAA Aerospace Sciences Meeting and Exhibit*. 2006, Reno, Nevada American Institute of Aeronautics and Astronautics.

[4] A. G. H. van der Donk, P. R. Scheeper, W. Olthus, and P. Bergveld, "Modelling of silicon condenser microphones," *Sensors and Actuators*, vol. 40, pp. 203-216, 1994.

[5] S. D. Senturia, *Microsystems Design.* New York, NY: Springer, 2001.

[6] T. B. Gabrielson, "Mechanical-thermal noise in micromachined acoustic and vibration sensors," *IEEE Transactions on Electron Devices*, vol. 40, pp. 903-909, 1993.

[7] R. P. Ried, E. S. Kim, D. M. Hong, and R. S. Muller, "Piezoelectric microphone with on-chip CMOS circuits," *Journal of Microelectromechanical Systems*, vol. 2, pp. 111-120, 1993.

[8] X. Wu, Y. Yang, J. Cai, T. Ren, and L. Liu, "Measurements of ferroelectric MEMS microphones," *Integrated Ferroelectrics*, vol. 69, pp. 417-429, 2005.

[9] N. Bilaniuk, "Optical microphone transduction techniques," *Applied Acoustics*, vol. 50, pp. 35-63, 1997.

[10] P. R. Scheeper, B. Nordstrand, J. O. Gulløv, B. Liu, T. Clausen, L. Midjord, and T. Storgaard-Larsen, "A new measurement microphone based on MEMS technology," *Journal of Microelectromechanical Systems*, vol. 12, pp. 880-891, 2003.

[11] P.V. Loeppert and S.B. Lee, "A commercialized MEMS microphone for high-volume consumer electronics," *The Journal of the Acoutical Society of America*, vol. 116, pp. 2510, 2004.

[12] N. A. Hall, *Micromachined Broadband Acoustic Transducer with Integrated Optical Displacement Detection*, Ph.D. thesis, Georgia Institute of Technology, 2004

[13] N. A. Hall, B. Bicen, M. K. Jeelani, W. Lee, S. Qureshi, F. L. Degertekin, and M. Okandan, "Micromachined microphones with diffraction-based optical displacement detection," *The Journal of the Acoustical Society of America*, vol. 118, pp. 3000-3009, 2005.

[14] R. N. Miles, D. Robert, and R. R. Hoy, "Mechanically coupled ears for directional hearing in the parasitoid fly ormia ochracea," *The Journal of the Acoustical Society of America*, vol. 98, pp. 3059-3070, 1995.

[15] P. R. Dragsten, W. W. Webb, J. A. Paton, and R. R. Capranica, "Auditory membrane vibrations: measurements at sub-angstrom levels by optical heterodyne spectroscopy," *Science*, vol. 185, pp. 55-57, 1974.

[16] L. Tin, *Diaphragm design and analysis for the ormia differential microphone*, BS thesis, Tsinghua University, 1999

[17] H. Dillon and J. Macrae, "Performance requirements for hearing aids," *Journal of Rehabilitation Research and Development*, vol. 23, pp. 1-15, 1986.

[18] S. C. Thompson, Directional patterns obtained from two or three microphones. 2000, Knowles Electronics: Itasca, Illinois.

[19] W. Lee, N. A. Hall, Z. Zhou, and F. L. Degertekin, "Fabrication and characterization of a micromachined acoustic sensor with integrated optical readout," *IEEE Journal of Selected Topics in Quantum Electronics*, vol. 10, pp. 643-651, 2004.

[20] N. A. Hall and F. L. Degertekin, "Integrated optical interferometric detection method for micromachined capacitive acoustic transducers," *Applied Physics Letters*, vol. 80, pp. 3859-3861, 2002.

[21] G. G. Yaralioglu, A. Atalar, S. R. Manalis, and C. F. Quate, "Analysis and design of an interdigital cantilever as a displacement sensor," *Journal of Applied Physics*, vol. 83, pp. 7405-7415, 1998.

[22] N. A. Hall, M. Okandan, R. Littress, D. Serkland, G. Keeler, K. Peterson, B. Bicen, C. Garcia, and F. L. Degertekin, "Micromachined accelerometers with optical read-out and electrostatic actuation for self-tuning, self dynamic characterization, and force-feedback modalities," *Journal of Microelectromechanical Systems*, vol. in-press.

[23] K. Lizuka, *Engineering Optics Second Edition.* Berlin, Germany: Springer, 1987.

[24] N. A. Hall, *Micromachined broadband acoustic transducers with integrated optical displacement detection*, Ph.D. thesis, Georgia Institute of Technology, 2004

[25] Photodiode Model no. ULMPIN-04-TN-U0101U, ULM Photonics, Ulm, Germany.

[26] VCSEL Model no. VCC85A1G-IS, Lasermate Group Inc., Pomona, CA, 91768.

[27] *OSLO: Optics Reference Version 6.1.* Littleton, MA: Lambda Research Corporation, 2001.

[28] J. L. Jewell, J. P. Harbison, A. Scherer, Y. H. Lee, and L. T. Florez, "Vertical-cavity surface-emitting lasers: design, growth, fabrication, characterization," *IEEE Journal of Quantum Electronics*, vol. 27, pp. 1331-1346, 1991.

[29] D. P. Poenar and R. F. Wolffenbuttel, "Optical properties of thin-film silicon-compatible materials," *Applied Optics*, vol. 36, pp. 5122-5128, 1997.

[30] J. I. Cisneros, "Optical characterization of dielectric and semiconductor thin films by use of transmission data," *Applied Optics*, vol. 37, pp. 5262-5270, 1998.

[31] H. Torun, *Design and fabrication of thermo-mechanical thermal detector arrays with optical readout*, M.S. thesis, Koc University, 2005

[32] Wook Lee, *Diffraction-based integrated optical readout for micromachined optomechanical sensors*, Ph.D. thesis, Georgia Institute of Technology, 2006

[33] P. C. Hobbs, "Ultrasensitive laser measurements without tears," *Applied Optics*, vol. 36, pp. 903-920, 1997.

[34] *Microphone Handbook: Vol. 1.* Nærum, Denmark: Brüel & Kjær 1996.

[35] D. Homentcovschi and R. N. Miles, "Viscous damping of perforated planar micromechanical structures," *Sensors and Actuators A*, vol. 119, pp. 544-552, 2005.

[36] S. C. Thompson, "Tutorial on microphone technologies for directional hearing aids," *The Hearing Journal*, vol. 56, pp. 14-21, 2003.

[37] *1/2 Inch Free-Field Microphone*. Larson Davis, [cited October, 2007], <http://www.larsondavis.com/docs/2541-1103_D0501.0016.pdf>.

[38] *Measurement Microphones*.1994, Brüel & Kjær, [cited June 2007], <http://www.bksv.com/2148.asp>.

[39] R. C. Ritter and G. T. Gillies, "Classical limit of mechanical thermal noise reduction by feedback," *Physical Review A*, vol. 31, pp. 995-1000, 1985.

[40] M. Pinard, P. F. Cohadon, T. Briant, and A. Heidmann, "Full mechanical characterization of a cold damped mirror," *Physical Review A*, vol. 63, pp. 13808, 2000.

[41] *TP series microphones*. Knowles, [cited August, 2007], <http://www.knowleselectronics.com/applications/bte.asp>.

[42] A. V. Oppenheim, A. S. Willsky, and S. H. Nawab, *Signals and Systems.* New Delhi: Prentice-Hall, 2005.